Development and Validation of a Turbulence Wall Model for Compressible Flows with Heat Transfer

A THESIS
SUBMITTED TO THE FACULTY OF THE GRADUATE SCHOOL
OF THE UNIVERSITY OF MINNESOTA
BY

Jeffrey R. Komives

IN PARTIAL FULFILLMENT OF THE REQUIREMENTS
FOR THE DEGREE OF
DOCTOR OF PHILOSOPHY

Graham V. Candler, Advisor

August, 2016

Acknowledgements

First and foremost, I would like to express my sincerest appreciation to my advisor, Professor Graham Candler, whose support and trust in me has made my accomplishments possible. I am also greatly indebted to Drs. Ioannis Nompelis, Pramod Subbareddy, and Heath Johnson whose advice, mentorship, and expertise have been invaluable in helping me frame and solve the problems at hand. Additionally, I would like to thank the Boeing Company for their sponsorship of this research.

I have been fortunate to have benefited from the involvement of an incredibly talented cohort of graduate students. I am grateful for the support and involvement from all of my graduate student colleagues, but in particular I'd like to thank Jason Bender, Joseph Brock, Ross Chaudry, Derek Dinzl, Sidharth GS, Anand Kartha, Aaron Neville, Loretta Trevino, and Erik Tylczak. I have also benefited from the involvement of an undergraduate researcher, Charles Hollender, who created the series of grids used in Chapter 6. I am also sincerely appreciative of Mr. Ray Muno for his support with my high-performance computing needs.

My studies at the University of Minnesota would not have been possible without the endorsement and support of several US Air Force agencies. I'd like to acknowledge the Department of Aeronautics and Astronautics at the Air Force Institute of Technology for supporting my request to pursue a degree at this institution. Mr. Whitney, Mr. Clepper, and Capt Rosenoff of AFIT/CI provided me continual and exceptional support. Finally, the officers, NCOs, staff, and cadets of AFROTC Detachments 415 and 410 have been unwavering in their support, for which I am grateful.

Lastly, I'd like to thank the multitude of friends, family, colleagues and mentors that I have engaged with in my personal, professional, and academic life. I am where I am today due in no small part to their influence and support.

Abstract

The computational cost to model high Reynolds number flows of engineering interest scales poorly with problem size and is excessively expensive. This fact motivates the development of turbulence wall models to lessen the computational burden. These models aim to provide accurate wall flux quantification on computational meshes that would otherwise be unable to accurately estimate these quantities. The benefit of using such an approximation is that the height of the wall-adjacent computational elements can be increased by one to two orders of magnitude, allowing for comparable increases in stable explicit timestep. This increase in timestep is critically necessary for the large eddy simulation of high Reynolds number turbulent flows.

To date, most research in the application of wall models has focused on incompressible flows or flows with very weak compressibility. Very few studies examine the applicability of wall models to flows with significant compressibility and heat transfer.

The present work details the derivation of a wall model appropriate for compressible flows with heat transfer. The model framework allows for the inclusion of non-equilibrium terms in the determination of wall shear and heat transfer. The model is applied to a variety of supersonic and hypersonic flows, and is studied in both Reynolds-averaged simulations and large eddy simulations. The impact of several modeling approaches and model terms is examined. The wall-modeled calculations show excellent agreement with wall-resolved calculations and experimental data. For time accurate calculations, the use of the wall model allows for explicit timesteps more than 20 times larger than that of the wall-resolved calculation, significantly reducing both the cost of the calculation and the time required converge the solution.

Contents

List of Tables

List of Figures

Chapter 1

Introduction

1.1 Motivation

The study of hypersonic vehicles at flight representative conditions poses significant challenges. Flight experimentation is cost prohibitive in most cases, and is limited as to the number and type of measurements that can be made on the test vehicle. Ground testing is a less costly alternative to flight testing, affording greater control of test conditions and instrumentation. Ground test facilities can be limited, however, by short run-times, small test sections, and an inability to exactly replicate the flight freestream environment in terms of Mach number, free stream enthalpy, Reynolds number, and freestream disturbance level. An alternative to flight or ground experimentation is the simulation of such flows by solving the governing conservation equations (Navier-Stokes equations) in a discrete representation on high-performance computers (Computational Fluid Dynamics, CFD). CFD allows for parametric exploration of hypersonic vehicles and flows with detailed information available at every point in the solution domain. The challenges of hypersonic CFD are principally twofold; the accuracy of physical, chemical, and thermal models, and the excessive computational cost for simulations of flows at flight representative conditions. This work addresses the latter of these two challenges.

Turbulence models for Reynolds-Averaged Navier-Stokes (RANS) and Wall-Resolved Large Eddy Simulations (WR-LES) have stringent grid resolution requirements near

Direct Numerical Simulation	$N \sim \mathrm{Re}^{37/14}$
Wall-Resolved LES	$N \sim \mathrm{Re}^{13/7}$
Wall-Modeled LES	$N \sim \mathrm{Re}$

Table 1.1: Grid requirements for high Reynolds number turbulent boundary layers, from Choi and Moin. [1]

solid boundaries to produce accurate boundary layers and surface quantities. A typical requirement is that the maximum height of the wall-adjacent cell across the entire boundary be kept under one in wall units ($y^+ \leq 1$). This requirement dictates that a large percentage of the cells used in a given calculation be allocated to the boundary layer, limiting the maximum Reynolds number that can be achieved on a given computational resource. Additionally, the small dimensions of the cells near the wall give rise to restrictive timestep limitations. For unsteady calculations, an overly restrictive timestep results in greater computational efforts to establish the baseline flowfield and converge the relevant statistics. In order to rapidly converge high Reynolds number flows of engineering interest, an alternative solution strategy is required.

Recently, Choi and Moin [1] have revisited Chapman's [7] classic computational requirement scaling estimates using a more current understanding of how skin friction scales at high Reynolds number. Using this revised data, grid requirements for high Reynolds number simulations scale with Reynolds number as shown in Table 1.1. In order to compute high Reynolds number flows of engineering interest, WR-LES is not a feasible solution as the grid requirements are nearly quadratic with Reynolds number. The alternative is the use of a wall-modeled calculation where the conservation equations are simplified in the near-wall region and are not solved in the same finite-volume grid as the rest of the simulation.

A preponderance of the existing literature on wall models for high Reynolds number flows assume that the turbulent boundary layer experiences a zero or mild pressure gradient, and that all inertial terms balance [8, 9, 10, 11]. Under these assumptions, conservation of streamwise momentum reduces to a simple expression of constant shear, which is appealing due to the straightforward solution procedure required for the ordinary differential equation (ODE) and the availability of analytic solutions in the form of the well known law of the wall [12]. Fewer works attempt to model heat transfer

within the wall model framework, but those that do often assume adiabatic walls and flows with mild density gradients.

1.2 Taxonomy of the Turbulent Boundary Layer

Before conducting an analysis of wall-bounded turbulence, it is important to establish a common framework in which we can discuss particular aspects of the flow. Turbulent boundary layers are characterized by a range of turbulent eddy scales that diminish as they approach the wall [13]. The Direct Numerical Simulation (DNS) of Pirozzoli and Bernardini [4] shown in Fig. 1.1 clearly shows the range of turbulent length scales in a compressible turbulent boundary layer.

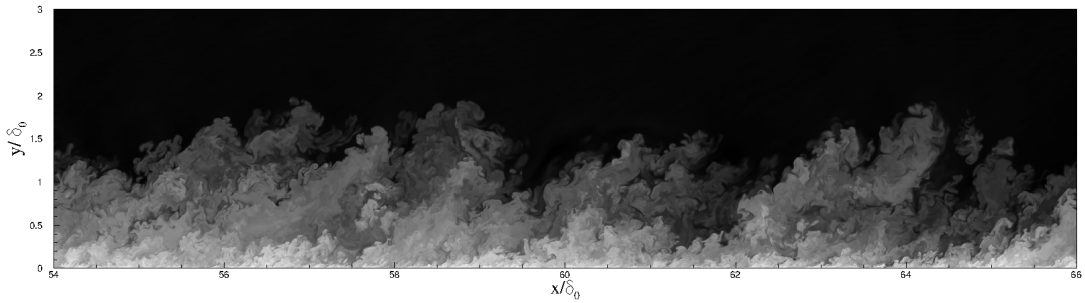

Figure 1.1: Contours of density in a supersonic turbulent boundary layer direct numerical simulation. DNS by Pirozzoli and Bernardini [4]

In practice, the analysis or simulation of all scales of wall-bounded turbulent motion is intractable for engineering purposes. For this reason, spatial or temporal averaging is usually conducted to reduce the scope of the analysis to more energetic motions and the statistics of the turbulence. Numerical simulations of the spatially-filtered governing equations are referred to as Large Eddy Simulations (LES), while temporally averaged simulations are referred to as Reynolds-Averaged Navier Stokes simulations. Reynolds averaging is also applied to experimental datasets to examine attributes of the flow in the mean.

When Reynolds averaging is applied to the Navier Stokes equations, an additional set of terms arise known as the Reynolds stresses, $\overline{u_i' u_j'}$. When starting with the momentum equation:

$$\frac{\partial \rho u_i}{\partial t} + \frac{\partial}{\partial x_j}(\rho u_i u_j + p\delta_{ij}) = \frac{\partial \tau_{ij}}{\partial x_j} \tag{1.1}$$

we can represent an instantaneous flow quantity as the sum of a mean and fluctuating component

$$\phi = \overline{\phi} + \phi' \tag{1.2}$$

After substituting the decomposed flow quantities back into the momentum equation and averaging, we arrive at the expression:

$$\frac{\partial}{\partial x_j}(\overline{\rho u}_i \overline{u}_j + \overline{p}\delta_{ij}) = \frac{\partial}{\partial x_j}\left(\overline{\tau}_{ij} - \overline{\rho u_i' u_j'}\right) \tag{1.3}$$

These stresses function much like the viscous stresses, but arise from the mean effect of turbulent motion. Often, the approximation of Boussinesq [14] is applied to equate the Reynolds stresses to an effective turbulent viscosity, which can be modeled as augmenting molecular viscosity.

It is traditional in the analysis of wall-bounded turbulent flows to normalize boundary layer quantities by the gas thermodynamic state at the wall and shear at the wall. The friction (or shear) velocity is a velocity scale defined by the ratio of wall shear to wall density $u_\tau = \sqrt{\tau_w/\rho}$. The friction velocity is in turn used to non-dimensionalize velocity in the boundary layer as $u^+ = u/u_\tau$ and to non-dimensionalize distance as $y^+ = yu_\tau/\nu$. These normalizations are commonly referred to as "wall units".

Subject to non-dimensionalization into wall units, zero pressure gradient incompressible turbulent boundary layers across a range of Reynolds numbers collapse into the famous *law of the wall* [12]. A representative profile of the collapsed profile is shown in Fig. 1.2. There are three regions of interest in this figure. First is the **viscous sub-layer** which exists from the wall to approximately $y^+ = 10$. In this region, viscous effects dominate and $u^+ \approx y^+$. The second region extends from the viscous sub-layer towards the edge of the boundary layer and is known as the **log-layer**. In this region, the velocity profile obeys the law of the wall, $u^+ = \frac{1}{\kappa}\ln(y^+) + C$, and is shown as a dashed line in Fig. 1.2. Between the log-layer and the edge of the boundary layer lies

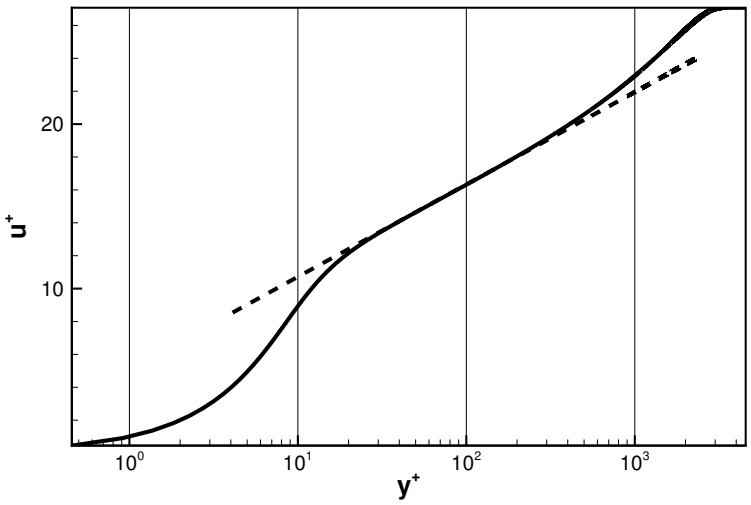

Figure 1.2: Incompressible boundary layer expressed in wall units

the third region, the **wake or defect layer** which is famously described by Coles [15]. The wake region is where the inertial effects of large eddies in the outermost portion of the boundary layer dominate the equilibrium shear process present in the log-layer.

For compressible boundary layers, variations in boundary layer temperature and density are significant. In incompressible flows, the gas total temperature is approximately equal to its static temperature, so no density variation is present in the boundary layer. For supersonic flows, the static temperature of the gas increases as viscous forces act upon it. This temperature variation is most pronounced in isothermal, or cold wall flows, where conduction processes are present to equilibrate the gas temperature with the wall temperature. An example of such a profile is given in Fig. 1.3.

1.3 Wall-Modeled Solutions of the Governing Equations

Wall models function by solving a simplified set of the Navier-Stokes equations in the near-wall region of a CFD simulation. The primary benefit of this simplification is that fewer grid points are needed in the near-wall region, relaxing the often stringent near-wall cell heights. Since the high aspect ratio cells near the wall are typically the ones that restrict the global timestep due to the Courant-Friedrichs-Lewy (CFL) restriction, relaxing this spacing directly results in a larger allowable explicit timestep.

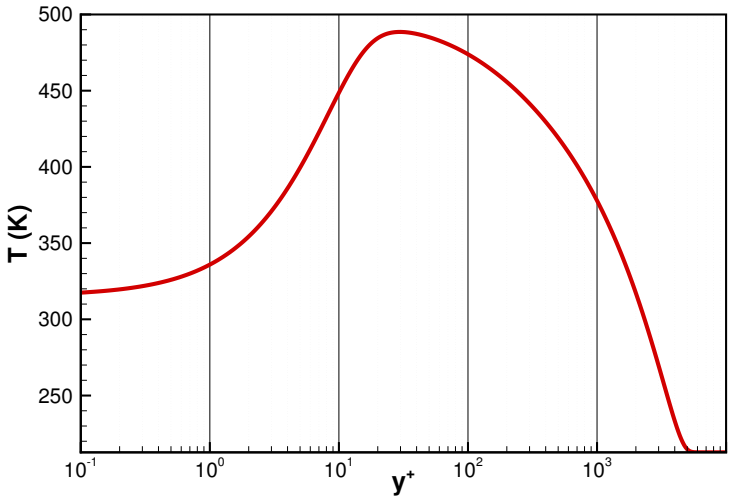

Figure 1.3: Temperature profile of an isothermal compressible boundary layer

$$\Delta t < \frac{\Delta x_{\min}}{|V| + a} \tag{1.4}$$

Piomelli and Balaras [16] broadly categorize two approaches to formulating wall models; the equilibrium stress approach and the zonal approach. Wall models start from an expression of the streamwise momentum equation:

$$\frac{\partial \rho u}{\partial t} + \frac{\partial \rho u u_j}{\partial x_j} = \frac{\partial}{\partial x_j}(\sigma_{1j} - P\delta_{1j}) \tag{1.5}$$

Wall models developed using the equilibrium stress approach assume steady flow, no advection imbalance or pressure gradient within the boundary layer, and gradients in the wall-normal direction are much larger than gradients in the streamwise direction. Under these assumptions, the streamwise momentum equations reduces to an expression of constant wall shear.

$$\frac{\partial}{\partial y}\left[(\mu + \mu_t)\frac{\partial u}{\partial y}\right] = 0 \tag{1.6}$$

These classes of solutions exactly recreate the law of the wall for zero pressure gradient boundary layers.

The other category of wall model approaches defined by Piomelli and Balaras is the zonal approach. Models using the zonal approach use a different set of equations to describe the inner layer of the wall-bounded flow than is used in the rest of the calculation. The Detached Eddy Simulation method of Spalart [17] fits this definition, as a separate turbulence mode is active based on a computational element's proximity to the wall. The oTwo Layer Model (TLM) is a zonal approach where two separate grids are used; one for the general flowfield and another for the near-wall region. In the TLM the general grid extends to the wall, but wall fluxes are not constructed from the data on this grid. Instead, wall shear and heat flux from the wall model grid is imposed at the wall. Traditional practice has been to use the solution in the wall-adjacent cell as the input to the wall model grid, but recent studies by Kawai and Larsson [8] have suggested a change in this practice. The location of data extraction for the wall model is referred to as the "probe location" in this work, and is often given the symbol h^+_{wm}.

1.4 Review of Related Work

Much of the development in wall-modeled turbulent simulations over the last decade has focused on extending wall models to compressible flows and evaluating their performance in a variety of flow regimes. The wall model of Nichols and Nelson [10] serves as a very good primer on how an equilibrium stress model is integrated with a RANS solver with extensions to compressible flows.

Bond and Blottner used a similar approach in the integration of their two-layer "Diffusion Model" [18, 19, 20], which was integrated with a RANS solver and used to examine equilibrium boundary layers with isothermal wall conditions. An important aspect of Bond and Blottner's work is that they decoupled the solution of the wall model equations and instead solved a series of loosely-coupled ODEs.

Increasingly in recent years, LES has been used to study wall-bounded turbulent flows. Using wall-modeled LES, Kawai and Larsson [8] showed that data from the wall-adjacent cell should *not* be used as input data for a wall model, as the data in such cells are necessarily under-resolved. Instead, the authors suggest using data from several cells away from the wall to increase the quality of the data used by the wall model.

A series of authors have examined the performance of Wall-Modeled LES (WM-LES) in highly compressible flows. Dawson, Bodart, and Lele [9] examined a supersonic turbulent boundary layer flowing into a compression ramp. Their simulation using TLM with only equilibrium stress terms failed to consistently reproduce aspects of the turbulent separation and reattachment, which they attributed to missing physics within the wall model. Namely, that pressure gradient and convective terms are the dominant terms in the momentum balance of a boundary layer undergoing a compression STBLI.

Hickel *et al.* [21] investigated two ways of approximating the non-equilibrium terms of the wall model using only data from the resolved scale of the LES. The first method was to approximate the convective term to balance the streamwise pressure gradient, and to damp the term linearly below a threshold. The second method was to approximate the profile based on the value of the convective term at the probe location, and damp the profile proportional to the filtered velocity. To test these formulations, the authors examined WM-LES of a shock impingement of a turbulent boundary layer. No clear conclusion was reached over the efficacy of these approximations.

Vane *et al.* [11] used WM-LES to examine high Reynolds number supersonic duct flow subject to a normal shock train. Their adiabatic calculations used only the equilibrium stress terms of the wall model. The authors noted displaced shock locations relevant to WR-LES for their low Reynolds number condition.

An alternative approach to integrating a TLM with a LES has been proposed by Park and Moin [22, 23]. Whereas a preponderance of the literature solves a series of one-dimensional model problems at each wall face, Park and Moin have resorted to building an auxiliary three-dimensional finite-volume mesh on which the wall model is solved. Data are interpolated from the LES onto the boundary of the wall model mesh, and the three-dimensional RANS equations are solved using the finite volume method, thereby directly incorporating pressure and convective terms within the model. This model was validated against incompressible transitional and fully-turbulent flat plate boundary layers, as well as subsonic airfoils at incipient separation.

With the exception of the RANS models, the aforementioned works assumed adiabatic wall boundary conditions. Compared to an isothermal wall boundary condition, an adiabatic wall represents a fairly benign level of compressibility for a wall model to

handle. Adiabatic boundary layers are not subject to temperature overshoots in the near-wall region and the associated inflection in density gradient.

1.5 Scope of the Current Study

To overcome the wall spacing restriction inherent to high Reynolds number RANS or WR-LES, a wall model has been developed that accurately predicts surface quantities and boundary layer profiles on under-resolved grids. Particular attention is paid to ensure that the derivation of the model is valid for high Reynolds number flows in the hypersonic regime, including regions of Shock Turbulent Boundary Layer Interaction (STBLI). Model derivation, performance and limitations are discussed. The baseline CFD framework that this work is built on is the University of Minnesota hypersonics research code, US3D [24].

- Chapter 2 assesses the applicability of a closed-form equilibrium wall model based on an analytic solution of the Spalart-Allmaras turbulence model.
- Chapter 3 describes the derivation of a turbulence wall model suitable for high Reynolds number flows with heat transfer.
- Chapter 4 provides details on the implementation of the model presented in Chapter 3 in a parallel-unstructured flow solver.
- Chapter 5 assesses the suitability of various eddy-viscosity models for use within the wall model.
- Chapter 6 presents an analysis of inertial source terms in the wall model.
- Chapter 7 assesses the behavior of the model in a time-accurate large eddy simulation.
- Chapter 8 presents a final discussion of the analyses presented in this dissertation.

Chapter 2

Assessment of Spalart-Allmaras Based Equilibrium Model

As a preliminary step in this research, a closed-form equilibrium wall model was developed based on an analytic solution to the Spalart-Allmaras turbulence model, presented by Allmaras *et al.* [2]

2.1 Model Overview

The one-equation turbulence model of Spalart and Allmaras [25] has been robustly used since its introduction in 1992. Allmaras, Johnson and Spalart [2] restated the standard S-A model in 2012 with a few improvements. In this paper they also analytically solved the S-A equation subject to boundary layer assumptions. To arrive at this solution, the following assumptions were used:

- The fluid is incompressible
- The boundary layer is subject to a zero pressure gradient
- The boundary layer edge velocity is constant
- The advection terms in the momentum equation are negligible
- Streamwise gradients are much smaller than wall-normal gradients.

Constant	Value
$\overline{B}$	5.0333908790505579
a_1	8.148221580024245
b_1	7.4600876082527945
a_2	6.9287093849022945
b_2	7.468145790401841
c_1	2.5496773539754747
c_2	1.3301651588535228
c_3	3.599459109332379
c_4	3.6397531868684494

Table 2.1: Constants used in Eq. 2.2 from Allmaras *et al.* [2]

Subject to these assumptions and transformed into wall units, Allmaras *et al.* reduced the S-A equation to

$$\frac{\mathrm{d}u^+}{\mathrm{d}y^+} = \frac{c_{v1}^3 + (\kappa y^+)^3}{c_{v1}^3 + (\kappa y^+)^3(1 + \kappa y^+)} \tag{2.1}$$

which has the exact solution of

$$\begin{aligned} u^+\big(y^+\big) = \overline{B} + c_1 \log\Big(\big(y^+ + a_1\big)^2 + b_1^2\Big) - c_2 \log\Big(\big(y^+ + a_2\big)^2 + b_2^2\Big) \\ - c_3 \arctan\big(y^+ + a_1, b_1\big) - c_4 \arctan\big(y^+ + a_2, b_2\big) \end{aligned} \tag{2.2}$$

For standard model coefficients of $\kappa = 0.41$ and $c_v = 7.1$, the coefficients of the exact solution are presented in Table 2.1.

The preceding equation is implicit in shear velocity (u_τ) and therefore it is implicit in wall shear (τ_w) using the following definitions:

$$y^+ = y\frac{u_\tau}{\nu} \tag{2.3}$$

$$u^+ = \frac{u}{u_\tau} \tag{2.4}$$

$$u_\tau = \sqrt{\frac{\tau_w}{\rho}} \tag{2.5}$$

Plate	Re_L	5×10^6 [1/m]
	Mach No	0.2
	T	300 [K]
Bump	Re_L	3×10^6 [1/m]
	Mach No	0.2
	T	300 [K]

Table 2.2: Flow conditions for subsonic test cases

This solution has the same functional form of Spalding's formula [12], which has classically been used as a fit to the turbulent boundary layer of a flat plate. Spalding's formula is presented as:

$$y^+ = u^+ + e^{-\kappa B}\left[e^{\kappa u^+} - 1 - \kappa u^+ - (\kappa u^+)^2/2 - (\kappa u^+)^3/6\right] \tag{2.6}$$

Eq. 2.2 can be treated as a governing relation in a wall model. Given the flow variables as some point above a wall face, a value of wall shear can be uniquely determined that satisfies the equation.

2.2 Test Cases

To evaluate the performance of this model, two verification cases were chosen from the NASA Langley Turbulence Modeling Resource [26]. The cases were two-dimensional and subsonic due to the assumptions inherent in this wall model formulation. The cases chosen were the 2-D zero pressure gradient flat plate, and the 2-D bump-in-channel. The bump-in-channel case was selected as a mild streamwise pressure gradient would be present in the flow, allowing one to examine the errors produced by flowfields that deviate from the model assumptions. The pressure field associated with the 2-D bump-in-channel test case is shown in Fig. 2.1. The flow conditions for both cases are given in Table 2.2.

To establish a reference solution, the NASA-provided grids were used in US3D with simulation parameters given in Table 2.3. Calculations were run to steady state. For the flat plate case, the reference grid with 273 points in the streamwise direction was used. This grid had an initial off-wall spacing of $y^+ = 0.2$. For the bump-in-channel

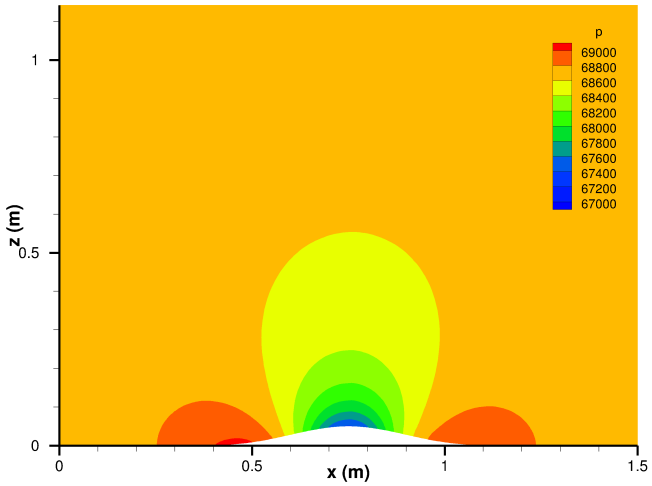

Figure 2.1: Pressure field associated with the 2-D bump-in-channel test case (Pa)

Parameter	Value
Time Integration	DPLR [27]
Inviscid Fluxes	2nd-Order Modified Steger-Warming [28]
Viscous Fluxes	2nd-Order Central
Thermochemistry	Perfect Gas - Air

Table 2.3: Simulation settings for subsonic test cases

case, the grid with 321 points in the streamwise direction was used, which had an initial off-wall spacing of $y^+ = 0.15$.

To create coarsened grids on which to evaluate the wall-model, grids were re-extruded in the wall-normal direction while preserving grid spacing in the streamwise direction. To accomplish this extrusion, the initial off-wall spacing was specified to yield the desired y^+, and a constant 8% growth rate was used. Examples of the grid spacings used for the flat plate are shown in Fig. 2.2. To evaluate the wall shear for a given face, data were sampled from the fourth cell off the wall.

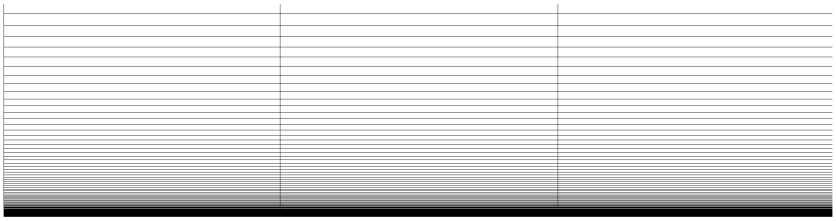

(a) $y^+ = 0.2$ (reference)

(b) $y^+ = 10$

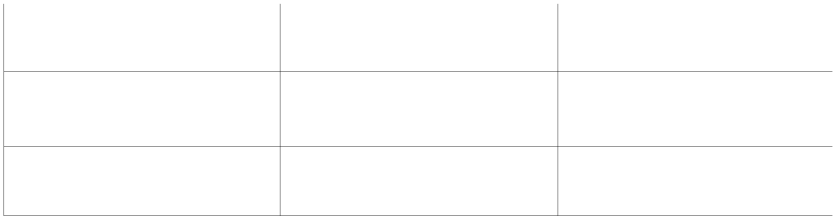

(c) $y^+ = 45$

Figure 2.2: Comparison of flat plate grid spacing

2.3 Analysis

This section presents an analysis of the wall-modeled solutions on the flat plate and bump-in-channel. Solutions are evaluated on the accuracy of skin friction profiles along the plate, and various boundary layer quantities.

2.3.1 2-D Flat Plate

Fig. 2.3 shows predictions of skin friction coefficient as a function of streamwise location on several grids. Skin friction coefficient is defined as defined as:

$$C_f = \frac{\tau_w}{\frac{1}{2}\rho U_e^2} \tag{2.7}$$

Shown in each figure is skin friction coefficient on the reference grid and on the coarsened grid without the application of a wall model, both using lines. The skin friction coefficient on the coarsened grid with the wall model applied is shown using symbols. For both coarsened grids, the application of the wall model results in an accurate determination of skin friction coefficient. For the $y^+ = 45$ case, the skin friction values predicted over the first half-meter of the plate exhibit some error due to the fact that the developing boundary layer is inadequately resolved on the coarsened mesh. It is not until the boundary layer grows to encompass the wall model probe location that the wall model is able to function appropriately.

Profiles of velocity within the boundary layer are given in Fig. 2.4. Velocity in wall units is plotted against the logarithm of wall-normal distance in wall units. Fig. 2.5 shows profiles of the ratio of turbulent S-A variable to freestream dynamic viscosity ($\rho\tilde{\nu}/\mu$) at the same station. Vertical dashed lines in these plots represent the location of the centroid of the wall-adjacent cell on the coarsened mesh. It is clear from these figures that the entirety of the viscous sublayer is sub-cell information on these meshes, and a wall model is required to capture the viscous sublayer.

For both meshes, the application of the wall model results in the accurate prediction of the velocity boundary layer. Note that the velocity in the wall-adjacent cell is not predicted accurately. This supports the modeling decision to provide inputs to the wall model from several cells away from the wall.

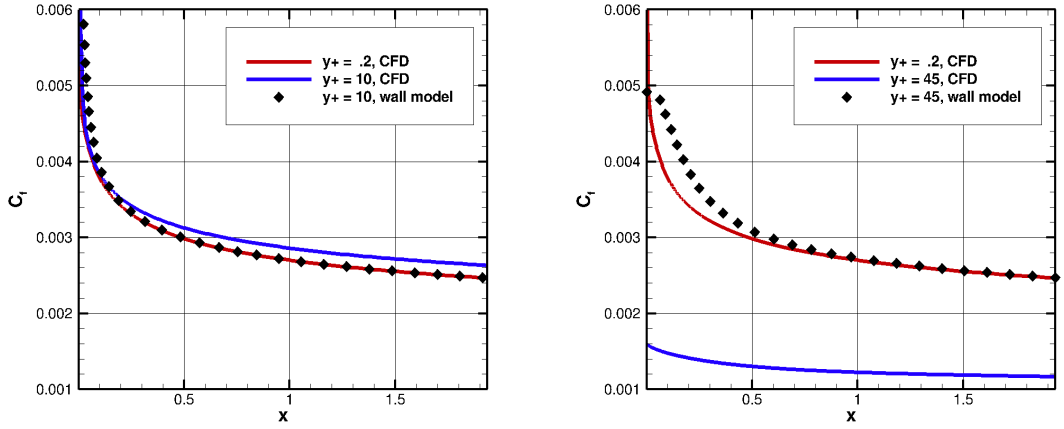

(a) $y^+ = 10$ (b) $y^+ = 45$

Figure 2.3: Flat plate skin friction coefficient for wall-modeled grids. Distance in meters

For the coarsest mesh, while the shape of the S-A profile is correct, the peak is somewhat overpredicted. It is believed that this is the result of two factors:

1. The coarser mesh less accurately resolves the gradients needed in the solution of the S-A equation.

2. The lack of cells in the viscous sub layer do not allow the destruction terms of the S-A equation to appropriately balance production, resulting in a net overprediction.

2.3.2 2-D Bump-in-Channel

Fig. 2.6 presents the skin friction coefficient as a function of streamwise distance for the 2-D bump-in-channel test case on two coarsened grids. As in the flat plate results, lines are presented for the reference solution and solution on the coarsened grid without the application of the wall model. Symbols represent the wall-modeled solution on the coarsened grid.

Application of the wall model results in an overall accurate prediction of skin friction on both of the coarsened grids. A few errors are noteworthy:

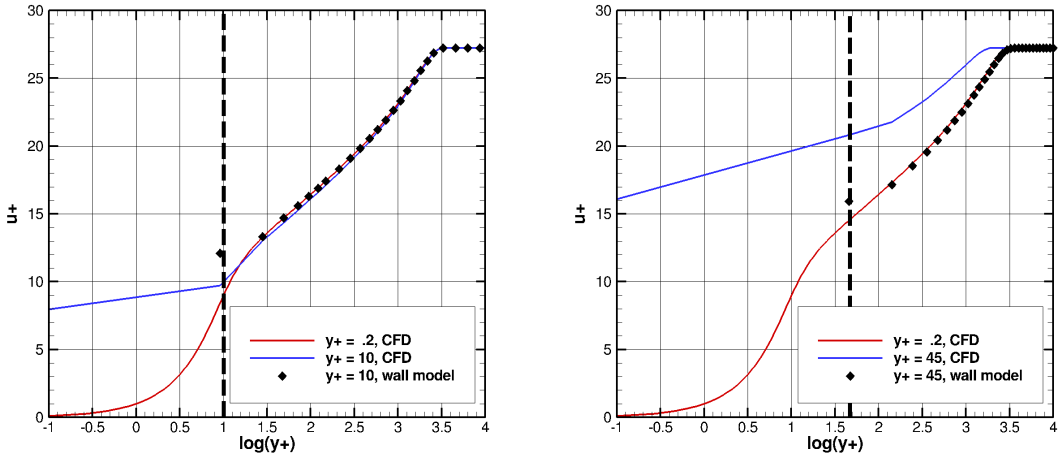

(a) $y^+ = 10$ (b) $y^+ = 45$

Figure 2.4: Flat plate velocity boundary layer profiles at $x = 1.0$ meters

1. As was seen on the flat plate, the coarsest grid produces erroneous skin friction estimates on the leading edge of the wall surface, where the boundary layer is not yet interacting with the probe cell.

2. The wall modeled skin friction peak is slightly overpredicted and downstream of the actual peak.

3. The skin friction predicted by the wall model on the windward side of the bump is significantly lower than determined by the resolved calculation.

The errors in skin friction coefficient here are attributable to the lack of pressure gradient effects in the formulation of Eq. 2.2. The boundary layer on the windward side of the bump experiences a favorable pressure gradient, as shown in Fig. 2.1. The favorable gradient accelerates the flow, requiring higher shear to balance the momentum equation.

Figs. 2.7 and 2.8 show boundary layer profiles of velocity and S-A variable ratio $(\rho\tilde{\nu}/\mu)$ on the two coarsened grids extracted at two locations. The profiles extracted at $x = .75$ meter location are shown in red with lines for the reference solutions and non-modeled solutions. Symbols again represent the wall-modeled solutions. This location corresponds to the apex of the bump. Profiles extracted at the $x = 1.2$ meter location

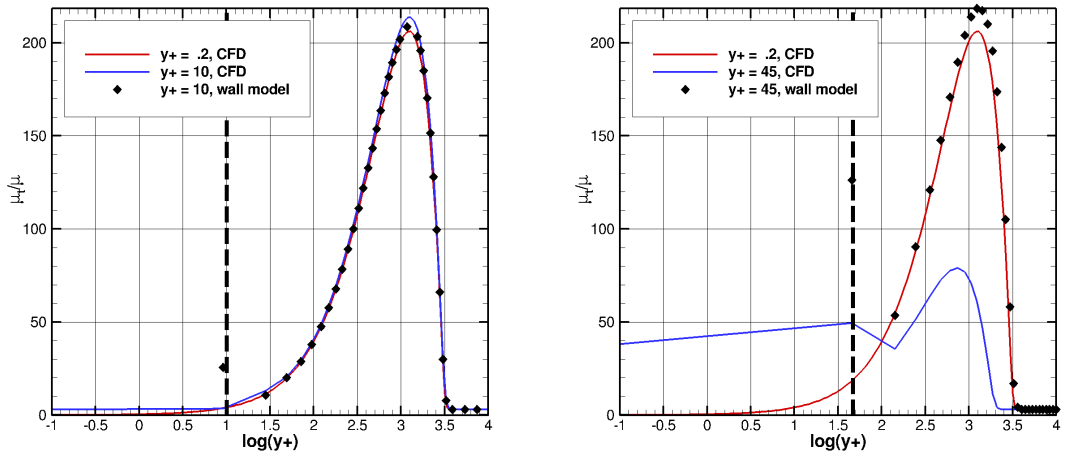

(a) $y^+ = 10$ (b) $y^+ = 45$

Figure 2.5: Flat plate eddy viscosity boundary layer profiles at $x = 1.0$ meters

are shown in black. The boundary layer at this station has experienced several different pressure gradients associated with conforming to the surface curvature of the bump.

Wall-modeled results for the velocity profile show very good agreement with the reference solution. The wall-modeled solution for turbulence variable exhibit the correct peak location, but incorrect peak amplitude. For the coarsest grid, the turbulence variable is overpredicted at for the entirety of the $x = .75$ meter profile. On both grids, the turbulence variable is underpredicted at the $x = 1.2$ meter station.

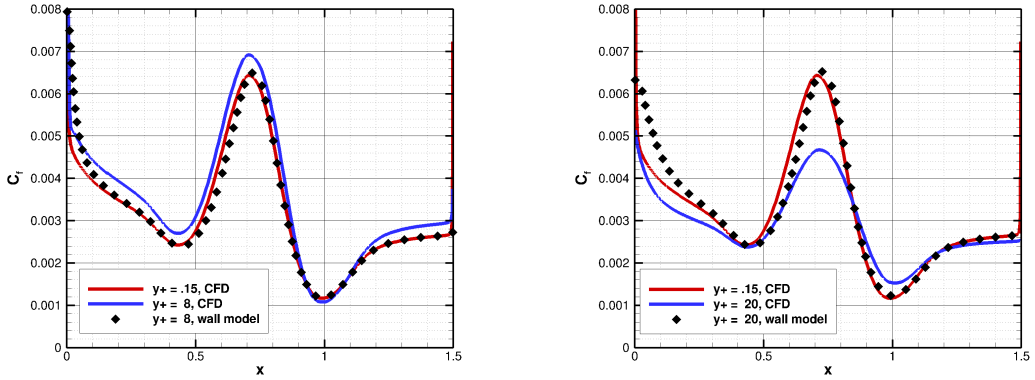

(a) $y^+ = 8$ (b) $y^+ = 20$

Figure 2.6: Bump-in-channel skin friction coefficient for wall-modeled grids

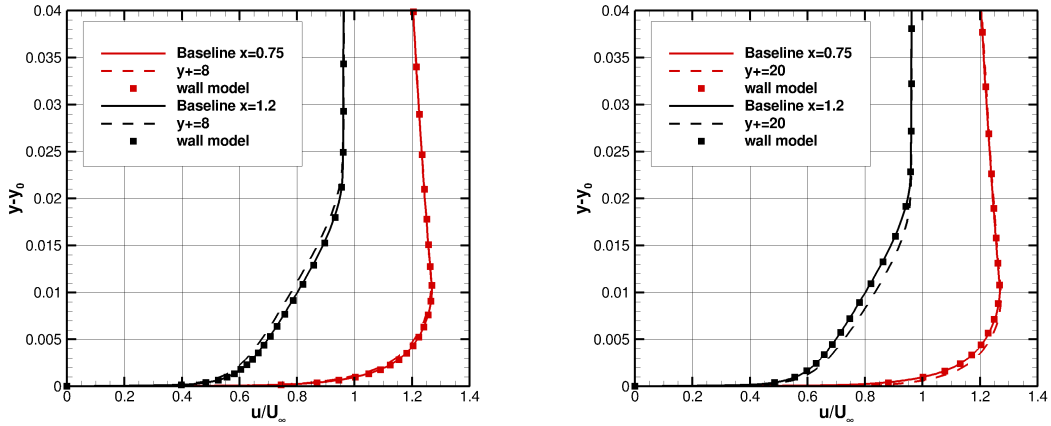

(a) $y^+ = 8$ (b) $y^+ = 20$

Figure 2.7: Bump-in-channel velocity boundary layer profiles at $x = 0.75$ and $x = 1.2$ meters

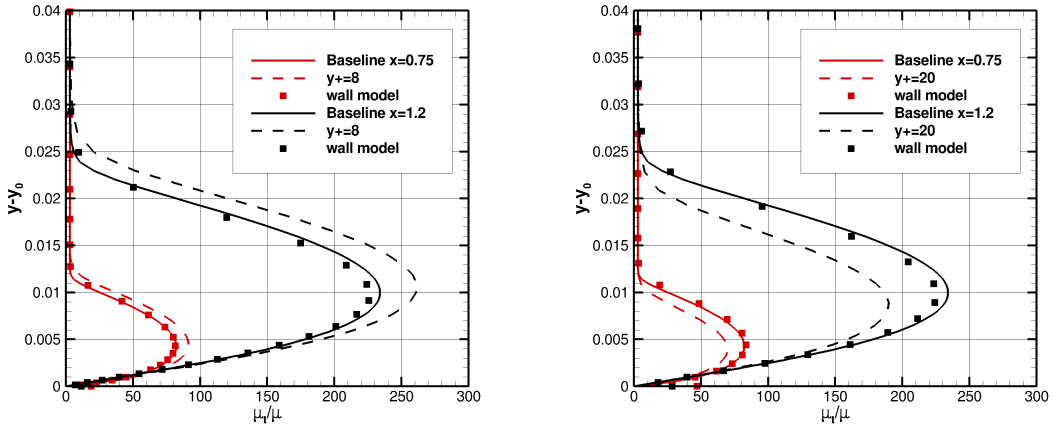

(a) $y^+ = 8$ (b) $y^+ = 20$

Figure 2.8: Bump-in-channel eddy viscosity boundary layer profiles at $x = 1.0$ and $x = 1.2$ meters

2.4 Conclusions

A wall model based on an analytic solution to the S-A equation was integrated into US3D and tested against two test conditions used for turbulence model verification. For a zero pressure gradient incompressible boundary layer, the use of the wall model resulted in accurate predictions of skin friction and velocity profiles for the two coarsened grids examined. For the 2-D bump-in-channel, the use of the wall model resulted in accurate boundary layer velocity profiles on the coarsened grids, but somewhat inaccurate skin friction distributions. For both test cases there were deviations in the profiles of the turbulence variable.

Despite these initial successes, the model examined in this chapter has limited utility for further examinations of hypersonic boundary layers and shock turbulent boundary layer interactions. The following limitations of the model make it unsuitable:

- Incompressible formulation does not allow for density variation due to temperature gradients.
- Neglecting advection and pressure gradient terms in the wall model omits important physics present in shock turbulent boundary layer interactions.
- An additional closure would be required to determine the wall heat transfer and temperature profiles within the modeled region.

To overcome the issues identified above, a new set of model equations are derived. The model is defined in detail in Chapter 3, and incorporates compressibility, heat transfer, pressure gradients, and inertial effects.

Chapter 3

Model Formulation

The primary error caused by under-resolved wall cells is an incorrect viscous flux calculation due to inaccurate gradients evaluated at the wall. The purpose of a wall model is to leverage knowledge of the physics of turbulent boundary layers to correct the calculation of wall shear and heat transfer to a physically meaningful value. As discussed in Sec. 1.4, an equilibrium wall model may not be accurate for STBLI flows with heat transfer due to the omission of pressure-gradient, convection and compressibility effects. We have developed a wall model framework that retains the necessary physics to resolve STBLI flows. The model is summarized as follows.

A reduced set of the Reynolds Averaged Navier-Stokes equations are solved in the modeled region. This is necessary to account for compressibility, heat transfer and inertial effects. Input data for the model is sampled several cells away from the wall. This places the interface location with the parent calculation, or probe point, in the log-layer and avoids unresolved data in the wall-adjacent cells. A schematic of the embedded wall grid within the LES grid is shown in Fig. 3.1. The model equations are solved via a 1-D iterative method on a virtual grid embedded within the LES. In this framework, fluxes of energy and momentum in directions other than the wall-normal are accounted for by a series of source terms. One source term accounts for the effect of pressure gradients within the boundary layer while a second term accounts for convective imbalances. Together, these terms are referred to as the inertial terms. We believe that the inertial terms, often ignored in wall modeling, are necessary in non-equilibrium

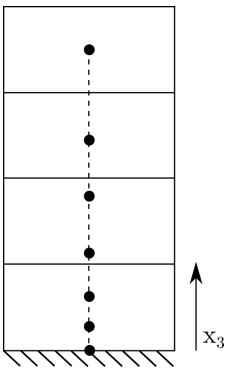

Figure 3.1: Schematic of wall grid shown within LES grid

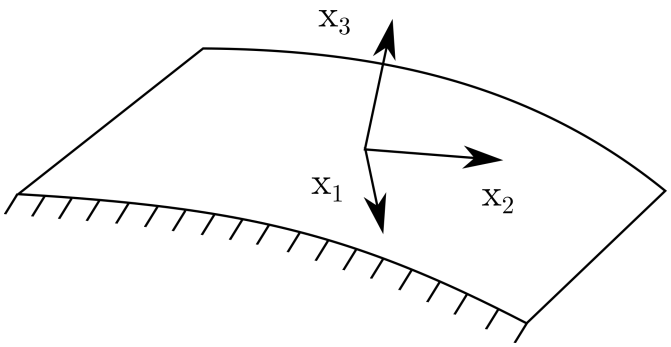

Figure 3.2: Schematic of wall model coordinate system

STBLI flows. The wall model solution at the boundary is then used by the LES to inform the construction of viscous fluxes at the wall.

3.1 Governing Equations

The model is defined in a wall-based coordinate system where x_1 and x_2 are two arbitrary, orthogonal wall-tangent directions and x_3 is the wall-normal. It is important to note that the x_1 and x_2 directions need not be chosen to align with the local streamlines. This generality costs little in terms of model complexity, but greatly enhances model robustness in application. A schematic of the coordinate system is given in Fig. 3.2.

The Navier-Stokes equations in divergence form are:

$$\frac{\partial U}{\partial t} + \frac{\partial F_1}{\partial x_1} + \frac{\partial F_2}{\partial x_2} + \frac{\partial F_3}{\partial x_3} = 0 \tag{3.1}$$

where U and F_j are the vectors of conserved variables and fluxes respectively.

$$U = \begin{pmatrix} \rho \\ \rho u_1 \\ \rho u_2 \\ \rho u_3 \\ E \end{pmatrix}, \quad F_j = \begin{pmatrix} \rho u_j \\ \rho u_1 u_j + p\delta_{1j} - \sigma_{1j} \\ \rho u_2 u_j + p\delta_{2j} - \sigma_{2j} \\ \rho u_3 u_j + p\delta_{3j} - \sigma_{3j} \\ (E+p)u_j - \sigma_{kj}u_k - q_j \end{pmatrix} \tag{3.2}$$

The viscous stress tensor, σ_{ij}, and heat conduction vector, q_j, are defined as

$$\sigma_{ij} = \hat{\mu}\left(\frac{\partial u_i}{\partial x_j} + \frac{\partial u_j}{\partial x_i}\right) - \frac{2}{3}\hat{\mu}\frac{\partial u_k}{\partial x_k}\delta_{ij} \tag{3.3}$$

$$q_j = \hat{\kappa}\frac{\partial T}{\partial x_j} \tag{3.4}$$

where the effective viscosity and thermal conductivity are approximated via the Boussinesq approximation as the sum of a molecular and turbulent component

$$\hat{\mu} = \mu + \mu_t, \qquad \hat{\kappa} = \kappa + \kappa_t \tag{3.5}$$

Pressure is assumed to be constant in the wall-normal direction, which allows for the conservation of wall-normal momentum and conservation of mass equations to be decoupled from the equation set. For a perfect gas, the equation of state allows us to recover the density field solely from the temperature field for an isobaric gas.

$$\rho = \frac{P_e}{RT} \tag{3.6}$$

As suggested by the solution strategy of Bond and Blottner [20], the density field and flow primitives can be updated in an outer loop while each of the remaining governing equations are solved in a decoupled fashion in an inner loop. Assuming no time-derivative of density, the conservation equations given in Eq. A.2 are recast as:

$$\frac{\partial Q}{\partial t} + \frac{1}{\rho}\left[\frac{\partial G_1}{\partial x_1} + \frac{\partial G_2}{\partial x_2} + \frac{\partial G_3}{\partial x_3}\right] = 0 \tag{3.7}$$

where Q is the solution vector with density decoupled, and G_j is the flux vector of the reduced set of equations.

$$Q = \begin{pmatrix} u_1 \\ u_2 \\ e \end{pmatrix}, \quad G_j = \begin{pmatrix} \rho u_1 u_j + p\delta_{1j} - \sigma_{1j} \\ \rho u_2 u_j + p\delta_{2j} - \sigma_{2j} \\ (E+p)u_j - \sigma_{kj}u_k - q_j \end{pmatrix} \tag{3.8}$$

The equation for conservation of wall normal momentum is not necessary since under the boundary-layer assumptions it reduces to the invariance of pressure in the wall normal direction.

$$\frac{\partial P}{\partial x_3} = 0 \tag{3.9}$$

Constant pressure in the boundary layer then allows us to decouple conservation of mass and prescribe density from an equation of state. The equations are expressed in terms of the primitives to decouple the density field, which has severe changes in gradient, from the ODEs being solved. The resulting velocities and specific energy fields are monotonic and better conditioned for implicit solution. The complete derivation of Eq. 3.8 is presented in Appendix A.1.

These equations are discretized on an embedded node-based mesh in the near wall region. The outermost node coincides with the probe location in the solver, and the innermost node is on the wall face.

3.2 Eddy Viscosity Modeling

This section examines the formulation of two different eddy viscosity models for the proposed wall model. The first model examined is a simple mixing length model with near-wall damping. This type of model is the one most typically found in compressible wall models [8, 9, 11, 29, 30], and describes the eddy viscosity profile typical of the

near-wall region of a boundary layer not subject to any pressure gradient. This method is completely local, requiring only local wall-shear, density, and distance from the wall.

$$D = \left[1 - e^{-(x_3^\star/A^+)}\right]^2 \tag{3.10}$$

$$\mu_t = \rho\kappa x_3 \sqrt{\frac{\tau_w}{\rho}} D \tag{3.11}$$

where $A^+ = 17$ and the von Karman constant is chosen as $\kappa = 0.41$. The wall coordinate used in the damping function, D, is modified to account for cold wall conditions.

$$x_3^\star = x_3 \frac{\sqrt{\rho\tau_w}}{\mu} \tag{3.12}$$

The second model chosen for this study is the compressible form of the Spalart-Allmaras turbulence model proposed by Catris and Aupoix [31] (SA-Catris). This is a one-equation model where the transport, production, and destruction of a turbulence variable is modeled and calibrated against a series of canonical flows. It has the advantage of modeling the physical processes of turbulence within a boundary layer whereas the aforementioned mixing-length model simply prescribes the profile that exists in the near-wall region of the boundar layer. This eddy viscosity model is very similar to the formulation of the S-A model used by Bond and Blottner [20] in their study. Using the assumptions inherited so far in this work and only considering gradients in the wall-normal direction, the SA-Catris model is expressed as:

$$\frac{\partial \tilde{\nu}}{\partial t} = \frac{1}{\rho}(S_P - S_D + D) \tag{3.13}$$

where

$$S_P = c_{b1}\tilde{S}\rho\tilde{\nu} \tag{3.14}$$

$$S_D = c_{w1} f_w \rho \left(\frac{\tilde{\nu}}{d}\right)^2 \tag{3.15}$$

$$D = \frac{1}{\sigma}\left[\frac{\partial}{\partial x_3}\left(\mu\frac{\partial \tilde{\nu}}{\partial x_3}\right) + \frac{\partial}{\partial x_3}\left(\sqrt{\rho}\tilde{\nu}\frac{\partial \sqrt{\rho}\tilde{\nu}}{\partial x_3}\right) + c_{b2}\frac{\partial \sqrt{\rho}\tilde{\nu}}{\partial x_3}\frac{\partial \sqrt{\rho}\tilde{\nu}}{\partial x_3}\right] \tag{3.16}$$

The full derivation of Eq. 3.13 is presented in Appendix A.2. Equation 3.13 is added to the set solved in Eq. 3.7. The model coefficients in Eqs. A.35 - 3.16 are taken from the standard S-A model. The turbulent Prandtl number for all models is chosen to be a constant 0.9.

3.3 Solution Form

Given the strong coupling in the wall-normal direction, the flux derivatives in the wall-tangent directions can be evaluated explicitly and moved to the right-hand side.

$$\left.\frac{\partial Q}{\partial t}\right|^{n+1} + \frac{1}{\rho}\left.\frac{\partial G_3}{\partial x_3}\right|^{n+1} = -\frac{1}{\rho}\left.\sum_{j=1}^{2}\frac{\partial G_j}{\partial x_j}\right|^{n} \tag{3.17}$$

The terms on the left-hand side of Eq (3.17) (including the SA-Catris equation) are cast into delta-form yielding a set of tri-diagonal scalar systems that are solved iteratively until convergence.

A number of other assumptions simplify the numerical procedure. Namely, viscous fluxes in the x_1 and x_2 direction are negligible, the streamwise and spanwise pressure gradients are assumed to be constant throughout the height of the modeled region, and are therefore determined by the LES sample location, and that the inner layer responds instantly to fluctuations in the outer layer, decoupling the timestep taken in the wall-solve from the global timestep. With the above assumptions the final form of the equations become:

u-velocity

$$\frac{1}{\Delta t}\delta u^{k+1} - \frac{1}{\rho^k}\frac{\partial}{\partial x_3}\left[\hat{\mu}^k\frac{\partial \delta u^{k+1}}{\partial x_3}\right] = \left[\frac{1}{\rho}\frac{\partial}{\partial x_3}\left(\hat{\mu}\frac{\partial u}{\partial x_3}\right)\right]^k - \frac{1}{\rho^k}\left[\sum_{j=1}^{3}\frac{\partial}{\partial x_j}(\rho u_1 u_j + p\delta_{1j})\right]^n \tag{3.18}$$

v-velocity

$$\frac{1}{\Delta t}\delta v^{k+1} - \frac{1}{\rho^k}\frac{\partial}{\partial x_3}\left[\hat{\mu}^k\frac{\partial \delta v^{k+1}}{\partial x_3}\right] = \left[\frac{1}{\rho}\frac{\partial}{\partial x_3}\left(\hat{\mu}\frac{\partial v}{\partial x_3}\right)\right]^k - \frac{1}{\rho^k}\left[\sum_{j=1}^{3}\frac{\partial}{\partial x_j}(\rho u_2 u_j + p\delta_{2j})\right]^n \tag{3.19}$$

specific energy

$$\frac{1}{\Delta t}\delta e^{k+1} - \frac{1}{\rho^k}\frac{\partial}{\partial x_3}\left[\frac{\hat{\kappa}^k}{c_v}\frac{\partial \delta e^{k+1}}{\partial x_3}\right] = \left[\frac{1}{\rho}\frac{\partial}{\partial x_3}\left(u\hat{\mu}\frac{\partial u}{\partial x_3} + v\hat{\mu}\frac{\partial v}{\partial x_3} + \hat{\kappa}\frac{\partial T}{\partial x_3}\right)\right]^k - \frac{1}{\rho^k}\left[\sum_{j=1}^{3}\frac{\partial}{\partial x_j}\{(E+p)u_j\}\right]^n \tag{3.20}$$

SA variable

$$\mathcal{A}\delta\tilde{\nu}^{k+1} - \frac{c_{b2}}{\sigma\rho^k}\mathcal{B}\frac{\partial}{\partial x_3}\delta\tilde{\nu}^{k+1} - \frac{1}{\sigma\rho^k}\frac{\partial}{\partial x_3}\left(\mathcal{C}\delta\tilde{\nu}^{k+1}\right) - \frac{1}{\sigma\rho^k}\frac{\partial}{\partial x_3}\left(\mathcal{D}\frac{\partial \delta\tilde{\nu}^{k+1}}{\partial x_3}\right) = \mathcal{E}\Big|^k \tag{3.21}$$

where the coefficients of the S-A equation are:

$$\mathcal{A} = \left[\frac{1}{\Delta t} - \left(c_{b1}\tilde{S} - \frac{c_{w1}f_w}{d^2}\tilde{\nu}\right) - \frac{2c_{b2}}{\sigma\rho}\left(\tilde{\nu}\frac{\partial\sqrt{\rho}}{\partial x_3}\frac{\partial\sqrt{\rho}}{\partial x_3} + \sqrt{\rho}\frac{\partial\sqrt{\rho}}{\partial x_3}\frac{\partial\tilde{\nu}}{\partial x_3}\right)\right]^k \tag{3.22}$$

$$\mathcal{B} = 2\left(\rho\frac{\partial\tilde{\nu}}{\partial x_3} + \sqrt{\rho}\tilde{\nu}\frac{\partial\sqrt{\rho}}{\partial x_3}\right)^k \tag{3.23}$$

$$\mathcal{C} = \left(2\sqrt{\rho}\tilde{\nu}\frac{\partial\sqrt{\rho}}{\partial x_3} + \rho\frac{\partial\tilde{\nu}}{\partial x_3}\right)^k \tag{3.24}$$

$$\mathcal{D} = (\mu + \rho\tilde{\nu})^k \tag{3.25}$$

$$\mathcal{E} = \frac{1}{\rho^k}\left\{S_P - S_D + \frac{1}{\sigma}\left[\frac{\partial}{\partial x_3}\left(\mu\frac{\partial\tilde{\nu}}{\partial x_3}\right) + \frac{\partial}{\partial x_3}\left(\sqrt{\rho}\tilde{\nu}^2\frac{\partial\sqrt{\rho}}{\partial x_3} + \rho\tilde{\nu}\frac{\partial\tilde{\nu}}{\partial x_3}\right) + c_{b2}\left(\sqrt{\rho}\frac{\partial\tilde{\nu}}{\partial x_3} + \tilde{\nu}\frac{\partial\sqrt{\rho}}{\partial x_3}\right)^2\right]\right\}^k \tag{3.26}$$

Where needed, $\tilde{S}$ is limited from reaching negative values using the method suggested by Allmaras *et al.* [2] Equations 3.18 - 3.21 are discretized using second-order central differencing. The index n indicates data from the previous solver timestep, which is held constant while solving the wall-model. The k index represents data from the previous iteration. As was done in the work by Bond and Blottner [20], the equations are solved iteratively using an inner-loop/outer-loop construct. On the inner loop, only the variable being solved for is updated in each equation. An outer loop exists to sync the flow variable amongst the equations, and to update the density field.

3.4 Boundary Conditions

The boundary conditions for Eqs. 3.18 - 3.21 are determined by the wall-state and the LES solution at the probe location. The values on the boundary are held fixed for the wall-model calculation. Turbulent eddy viscosity is specified to be zero at the wall, however its determination at the outer boundary differs depending on which viscosity model is used. If the mixing length model is used, the value is determined by the model and updated at each iteration. If the SA-Catris model is used, the value of the S-A variable on the boundary is chosen to produce the eddy-viscosity from the LES or RANS at that point, and held fixed throughout the wall model calculation.

3.5 Treatment of Inertial Source Term

Evaluation and approximation of the inertial source terms to Eqs. 3.18 - 3.21 are flow dependent and an active area of research. To evaluate these terms exactly, flux evaluations are required using data from within the wall model. This presents a host of complications and stability issues, including the determination of appropriate spanwise and streamwise boundary conditions within the model. Additionally, the choice of temporal integration scheme within the wall model is now coupled to the convective transport of information between wall modeled faces, and cannot necessarily be decoupled from the global timestep.

An approximation is made in this work to allow for some effect of inertial imbalances while keeping each wall-modeled face independent from each other face. The inertial

source term is decomposed into a pressure and convective component. For the inertial source term in the i-direction:

$$\frac{1}{\rho^k}\left[\sum_{j=1}^{3}\frac{\partial}{\partial x_j}(\rho u_i u_j + p\delta_{ij})\right]^n = \frac{1}{\rho^k}\left[\frac{\partial p}{\partial x_i} + \sum_{j=1}^{3}\frac{\partial}{\partial x_j}(\rho u_i u_j)\right]^n \tag{3.27}$$

Continuing with our assumption that pressure does not vary in the wall-normal direction, it follows that pressure gradient in the streamwise and spanwise directions are not dependent on the distance from the wall. As such, the value of the pressure gradient evaluated at the interface location between the wall model and LES/RANS calculation can be enforced all the way to the wall.

The value of the convective component of Eq. 3.27 is identically zero at the wall due to the no-slip boundary condition. An approximation of this term must vary smoothly from the value determined by the LES/RANS solution at the probe location to zero at the wall. The key difficulty in approximating a physically meaningful profile for this term in a cold-wall flow is the strong variation in density in the near wall region. As occurs for temperature profiles, there can be an overshoot in this quantity relative to the value determined at the probe location before returning to zero at the wall. For temperature, we have a governing equation available to us to accurately determine this profile for a wide range of conditions. The same is not true for this term. The approximation used in this work is to treat this term as constant in the outer portion of the boundary layer, and apply van Driest damping very close to the wall. Eq. 3.10 is applied with a damping constant A^+ of 10.

Chapter 4

Parallel-Unstructured Model Implementation

This chapter discusses several implementation issues for integrating the wall model described in Chapter 3 into a RANS or LES solver. While this integration is discussed from the viewpoint of integrating the model into US3D, extension to other flow solvers should not be significantly different.

4.1 Definition of Coordinate Frames

As discussed in Sec. 3.1, a wall-based coordinate system is used in the derivation of the wall model where two axes are tangent to the wall with the third axis being normal to the wall. A schematic of this coordinate system is presented in Fig. 4.1.

To establish this basis, one can leverage the orthonormal face basis already present in most flow solvers. The vectors can be arbitrarily reordered so long as right-handedness is preserved.

Once established, this basis also serves as a rotation matrix from the global frame to the wall frame. To determine the reverse transformation from wall frame back to global frame, simply take the matrix inverse of the wall basis.

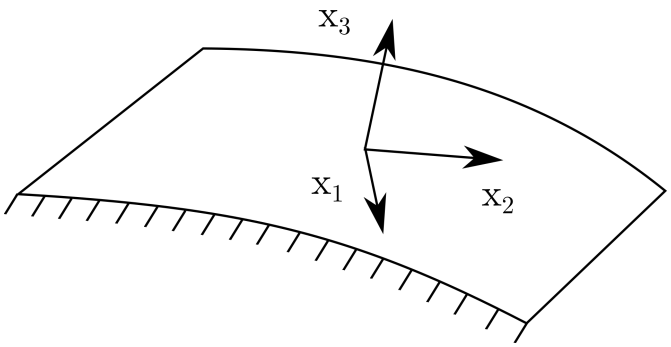

Figure 4.1: Schematic of wall model coordinate system

4.2 Discretization of Wall Model Mesh

A one-dimensional grid needs to be established between the wall face centroid and the cell centroid of the cell being used as an input to the wall model. First, a mapping must be made between each wall face and their respective probe locations. For solvers using Data Parallel Line Relaxation (DPLR), this information is already present in the line connectivity. For solvers without line data structures, a search will need to be performed for the fluid element the desired distance from the wall. Care should be taken to partition the grid in such a way that processor boundaries are not crossed in this search.

Once the endpoints of the wall model grid have been established, the node locations on one-dimensional grids are determined by a hyperbolic-tangent distribution. This distribution has the advantage of clustering nodes to the wall while having smooth grid metrics. The distribution of the nodes in the wall model grid is determined as follows:

$$y_i = \eta \left[1 - \frac{\tanh\left(\alpha \frac{i}{N}\right)}{\tanh(\alpha)} \right] \tag{4.1}$$

where η is the distance between the wall and the probe location and α is a tuning parameter taken as 3.0 in this work.

4.3 Wall Model Initialization

The equations solved on the wall grid are boundary value problems. They are uniquely defined by the solution variables and the gradients of solution variables on the boundary. As such, a numerical method used in solving these equations should arrive at a unique answer regardless of the initial condition, so long as the initial condition is well-posed.

To ensure a well-posed initial condition, the variables in the wall model are initialized to vary smoothly from the value at the probe location to the value prescribed at the wall.

$$\phi_i = \phi_N \left(\sqrt{\frac{y_i}{\eta}} \right) + \phi_w \left(1 - \sqrt{\frac{y_i}{\eta}} \right) \tag{4.2}$$

where ϕ represents any flow quantity, η is the distance between the wall and the probe, and the subscripts N and w correspond to the probe location and wall respectively.

Once a simulation is running, the wall model solution from the previous timestep is used as the initial condition for the next timestep's solution. The wall model solver can sometimes have difficulty converging to a solution if a strong source term is included along with an artificial initialization. For this reason, it is recommended to allow for sufficient iterations that an equilibrium boundary layer can be obtained without the source term, after which the source term is activated.

4.4 Application of Boundary Conditions to Wall Model and Global Solutions

Wall-modeled CFD calculations inherently are solving two problems concurrently. The finite-volume CFD calculation requires information from the wall model to inform correct fluxes on its wall boundary. The wall model requires information from the probe location to establish boundary values for its line calculation. The process of linking these calculations is described as follows:

4.4.1 Establish Wall Model Boundary Values

CFD values of velocity, temperature, density, and pressure are trivially enforced on the wall model. Since the centroid of the probe cell coincides with the boundary of the 1-D wall line, these values are simply transcribed from the CFD to the wall model. For velocity, a coordinate transformation is applied to express the CFD velocity in the wall coordinate frame

$$\vec{\mathbf{u}}_w = \overline{\overline{\mathbf{S}}}_w \vec{\mathbf{u}} \tag{4.3}$$

4.4.2 Determine and Store Wall Shear and Heat Flux

Once the wall model has converged sufficiently, the wall shear and wall heat transfer can be determined from the model data and applied as a boundary condition to the CFD. For steady-state simulations, iterating the wall model for approximately five iterations at a wall CFL of approximately 500 is sufficient to maintain stability of both the CFD and wall model calculations.

Wall shear is computed in each of the wall-tangent directions and stored at each wall face.

$$\tau_i = \mu_w \frac{\partial u_i}{\partial x_3} \tag{4.4}$$

$$\tau_1 \approx \mu_w \frac{u_1}{\Delta} \tag{4.5}$$

$$\tau_2 \approx \mu_2 \frac{u_2}{\Delta} \tag{4.6}$$

where Δ is the distance between the wall and the first off-wall node in the wall model mesh, μ_w is the fluid viscosity evaluated at the wall temperature, and u_i is the i-direction velocity at the first off-wall node in the wall model mesh. This wall shear is defined in the local wall coordinate system and must be transformed back to the CFD frame.

$$\vec{\tau} = \left[\overline{\overline{\mathbf{S}}}_w\right]^{-1} \vec{\tau}_w \tag{4.7}$$

Similarly, wall heat flux is evaluated as:

$$q_w = \kappa_w \frac{\partial T}{\partial x_3} \tag{4.8}$$

$$q_w \approx \kappa_w \frac{T - T_w}{\Delta} \tag{4.9}$$

where k_w is the thermal conductivity of the fluid at the wall temperature and T is the temperature of the first off-wall node in the wall model mesh. This quantity is independent of coordinate system, so no transformation needs to be applied.

4.4.3 Apply Wall-Modeled Fluxes to CFD

When the CFD calculation determines viscous fluxes across all faces, the values calculated on wall-modeled faces will be incorrect. Instead, the wall shear and heat flux from the wall model should be enforced at this point on the CFD. For finite-volume based derivations, this will simply entail multiplying the wall-modeled fluxes by the relevant face area.

$$\mathbf{F}'_{\mathbf{v}}\mathbf{S} = \begin{bmatrix} 0 \\ \vec{\tau}_{\mathrm{wm}} \\ q_w \end{bmatrix} s \tag{4.10}$$

It should be noted that for LES of very under-resolved grids, the shear enforced by the wall model can reverse the flow at the wall if the domain is not initialized with turbulent structure throughout. For this reason, it is recommended that either the domain be initialized with turbulent structures, or that the model not be active until turbulent structures impinge on the wall throughout the domain.

The reason for this behavior is simple. The wall model uses some form of the mixing length hypothesis to prescribe an effective turbulent viscosity in the inner layer of the boundary layer. If sufficient resolved-scale turbulent structures are not present near the wall, the subgrid scale stresses are not sufficient to balance the augmented stress enforced by the wall model, possibly resulting in spurious flow reversal.

Chapter 5

Analysis of Eddy Viscosity Formulations

While a preponderance of the wall-models in the literature use a mixing-length approach to determine the eddy viscosity to use within the wall model, there remain two open questions. How well can a mixing-length based wall model replicate a cold-wall boundary layer? What is the impact of the choice of probe height with regards to the accuracy of the wall-model eddy viscosity formulation?

To address these questions, an analysis is performed to evaluate the accuracy of the wall model, and the performance of the various eddy viscosity models. For this analysis the forebody data from the Calspan-University of Buffalo Research Center (CUBRC) LENS-II Hollow-Cylinder Flare (HCF) experiments from the shock wave/turbulent boundary layer study presented at AIAA Aviation 2014 [3] are used.

5.1 Test Geometry and Flow Conditions

The HCF forebody is a hollow cylinder with an outer diameter of 0.496 meters and a length of 2.474 meters. A schematic of the test article is given in Fig. 5.1. The test conditions selected for this analysis are presented in Table 5.1.

This condition is chosen due to the high Mach number, cold-wall isothermal conditions, and large extent of flow over the test article where inertial effects and pressure

(a) Picture of as-built test article with researcher for scale

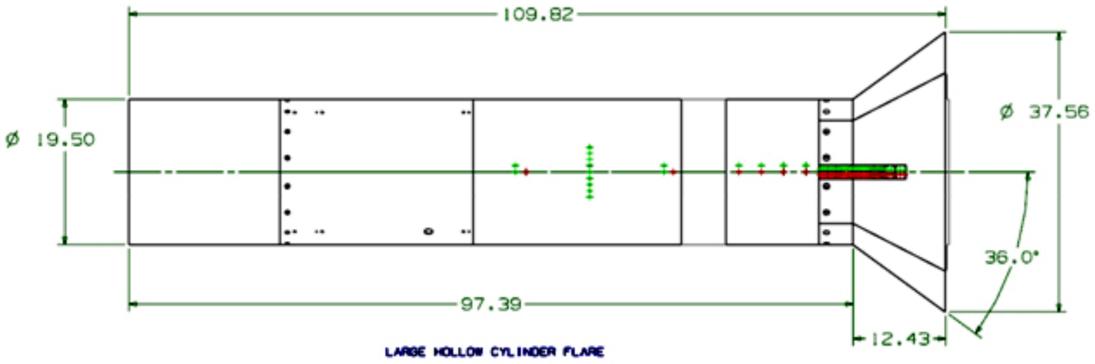

(b) Schematic of test article, dimensions in inches

Figure 5.1: Hollow Cylinder-Flare test article used for AIAA shock wave/turbulent boundary layer study presented at AIAA Aviation 2014, from [3]

Mach	Re_L	T_w/T_0
4.97	85.4×10^6	0.25

Table 5.1: Test condition for CUBRC LENS-II HCF experiment, run 16 [3]

	HCF run 16		
x [m]	0.5	1.1	1.5
τ_w [Pa]	309.18	276.15	263.58
q_w [W/cm^2]	21.11	18.83	17.96

Table 5.2: US3D wall shear and heat flux on a resolved grid for the HCF run 16 test condition

gradients are negligible. This allows for the wall-model to be run with only the equilibrium terms, focusing the examination on the effect of eddy viscosity formulations.

Simulations are conducted in US3D using modified Steger-Warming flux vector splitting [28] with second-order MUSCL on density, velocities, turbulence variable and pressure, gradients evaluated by weighted least-squares, molecular viscosity determined by Sutherland's formula, and turbulent viscosity from the SA-Catris Model [31]. Time integration is accomplished with the DPLR [27] method to drive the flow to steady-state. The 2-D axisymmetric grids are resolved to the wall with a $y^+ \ll 1$. Data extraction locations .5, 1.1, and 1.5 meters from the leading edge are chosen to minimize the influence from both the leading edge of the geometry and downstream STBLI, but allow for the streamwise evolution of the boundary layer.

Probe data are extracted from the converged US3D solutions at various heights in the boundary layer and used as boundary values for evaluation of the wall model. The heat flux and wall shear determined by the US3D simulations are given in table 5.2.

This test geometry is axisymmetric with no surface curvature in the streamwise direction in the area of interest. To capitalize on this fact and simplify the model formulation, the wall-tangent flux derivatives in Eq. 3.17 are neglected in the current implementation of the wall model. This results in a purely 1-D model involving only diffusive terms, as is common practice in wall modeling. This assumption may result in error for regions of flow where pressure gradients and inertial terms are non-negligible.

5.2 Baseline Solution

Figure 5.2 shows the reference boundary layer profile computed by US3D at the 1.1 meter station in wall units. Notable features include a peak in the S-A variable at a distance of 2800 wall units above the surface, and a peak temperature overshoot at 28 wall units. There is a very strong temperature gradient in the inner portion of the boundary layer to recover the cold-wall temperature from the peak temperature location. Associated with the temperature variation are strong density gradients throughout the boundary layer which peaks below 30 wall units. The same features are present at the other stations at different different values of y^+.

5.3 Model Performance

To evaluate the various formulations of the proposed wall model, data are sampled from the baseline boundary layer at specific heights in the boundary layer. Those data are used as boundary conditions for the wall model's ODE solve. The models are run independently of the solution that generated the baseline profiles. For both proposed eddy viscosity formulations, a single iteration of the inner loop is sufficient to stabilize the outer loop to convergence. In all cases the models converge to machine zero in negligible computational time.

The following model factors are examined:

- The impact of choice of eddy viscosity model
- The impact of probe height for the wall-model

To evaluate the above factors, boundary layer profiles computed by the wall model are compared to those from the reference solution. Additionally, predictions of wall shear and heat flux from the wall model is compared to the baseline solution.

5.3.1 van Driest Transformed Velocity and Temperature Profiles

van Driest-transformed velocity and temperature profiles computed by both eddy viscosity models with data extracted at various probe locations at the $x = 1.1$ meter station

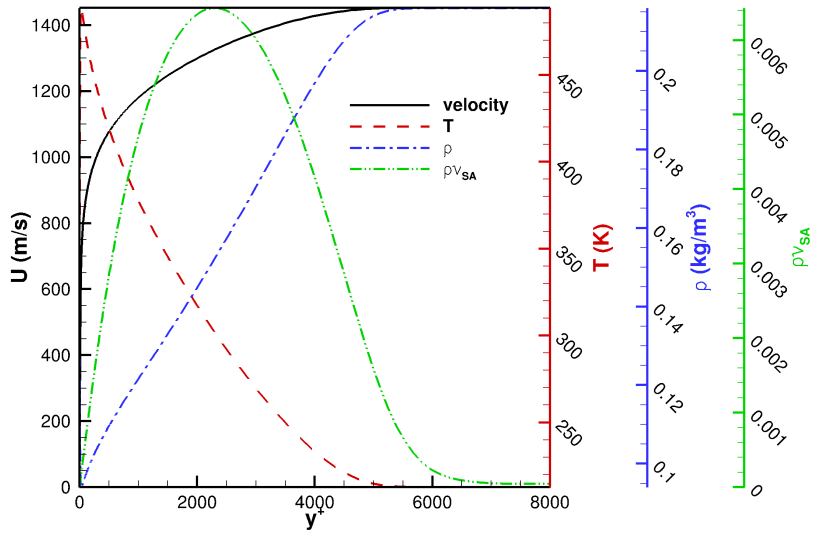

(a) wall-unit

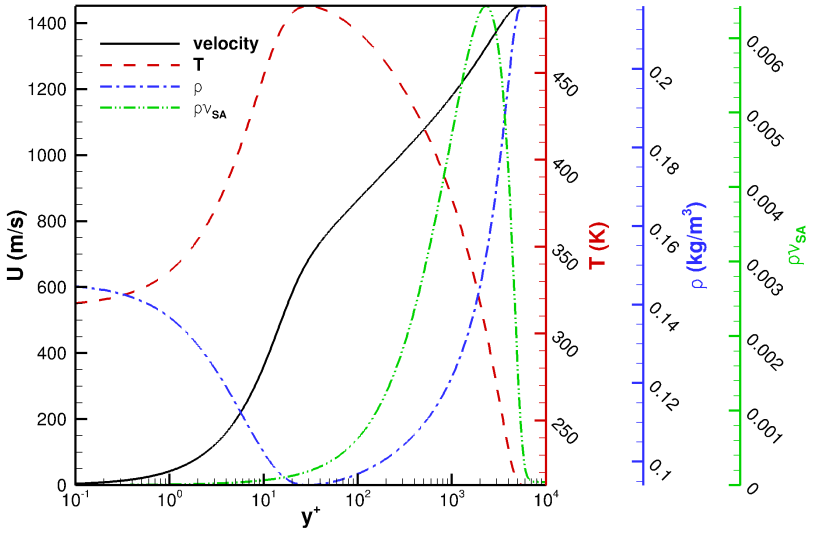

(b) log wall-unit

Figure 5.2: Computed wall-resolved boundary layer profiles for the Hollow Cylinder-Flare at x=1.1m

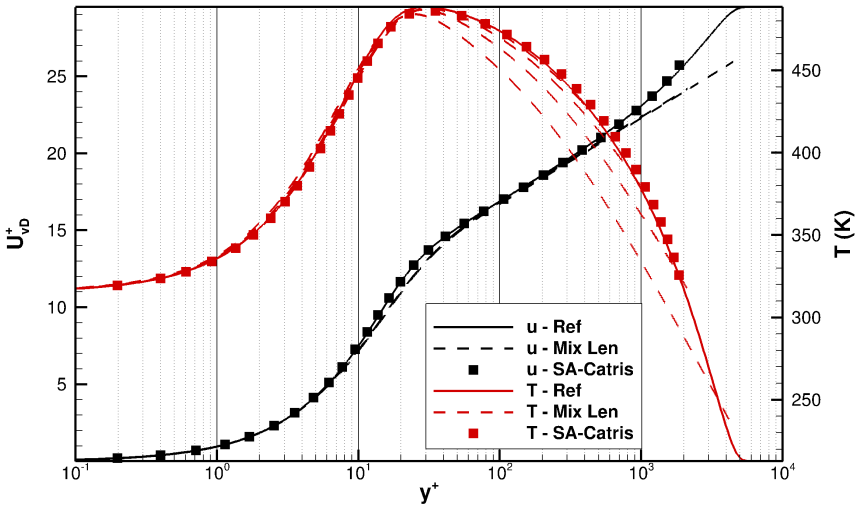

Figure 5.3: Velocity and temperature profiles for HCF at $x = 1.1$m

of the HCF are shown in Fig. 5.3. The van Driest transformation is accomplished on the wall modeled solution by performing the following integration:

$$u^+_{\mathrm{vD}} = \int_0^{u^+} \sqrt{\frac{\rho}{\rho_w}}\, \mathrm{d}u^+ \tag{5.1}$$

For probe locations placed more than 1000 wall units from the wall the mixing length model boundary layer profiles deviate significantly from the reference boundary layer. Use of the SA-Catris model to determine turbulent eddy viscosity significantly improves the wall model's approximation of the boundary layer profile.

5.3.2 Wall Shear and Heat Flux Predictions

Figures 5.4 through 5.6 show the wall shear and heat flux predicted by the two eddy-viscosity models for varying probe locations. These values are normalized by the quantity produced by the reference solution. The mixing length model significantly overpredicts both wall shear and het transfer for probe location at or beyond 1000 wall units at all stations. The SA-Catris model shows asymptotic convergence at all stations as the probe is brought closer to the wall. Compared to the predictions made by the mixing

length-based model, the SA-Catris model more accurately determines wall shear and heat transfer at every station and at each probe location.

The wall shear and heat flux calculations produced by the mixing length model are accurate so long as the probe is placed near the inner region of the boundary layer where viscous dissipation dominates the solution. Probes placed further into the log region of the boundary layer towards the wake region led to rapidly diverging predictions of both wall shear and heat flux. For cases where the probe is placed further into the log-layer, not only is density variation a factor, but so is non-linear variation of the production of turbulent kinetic energy, and by extension turbulent eddy viscosity. While most CFD practitioners refrain from using mixing length models outside of the inner-layer of a boundary layer, the employment of Kawai and Larsson [8] -like probe placement methods result in interface points being placed further into a boundary layer than has traditionally been accepted practice. This occurrence should be accounted for when choosing a turbulence modeling strategy.

5.4 Integrated Solution

Given that both eddy viscosity formulations produce accurate calculations of wall shear and heat flux for probe locations in the inner part of the boundary layer, the in situ performance of the model needs to be addressed. For the results in this section, a coarsened grid is generated with the wall-adjacent cell centroid located 90 wall units from the wall, and with the probe place approximately 650 wall units from the wall. The wall model is run with only equilibrium terms active.

The error bars in Fig. 5.7 are ten-percent of the wall-resolved calculation, and are present for reference only. Both eddy viscosity formulations produce solutions within this error band for axial locations of 0.5 meters and greater. Before this axial location, where the boundary layer is its thinnest, the solutions using different eddy viscosity formulations deviate from the wall-resolved solution. The wall model using the mixing length eddy viscosity formulation significantly overpredicts wall shear and heat flux in the region from 0 to 0.5 meters. The wall model using the S-A eddy viscosity formulation retains predictive capability up to the 0.2 meter axial location.

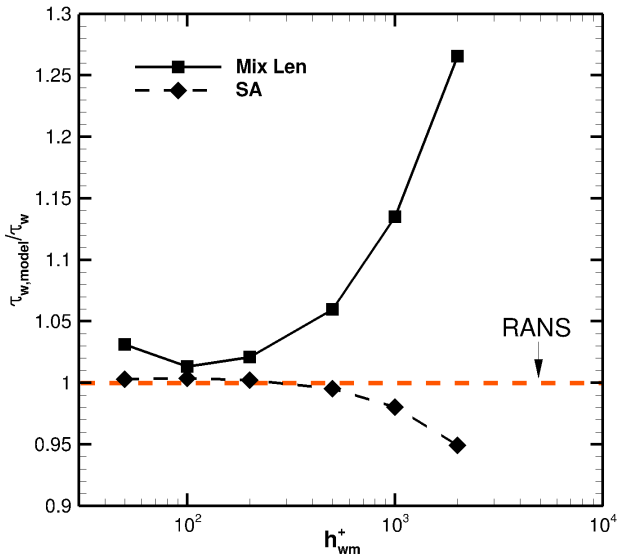

(a) wall shear

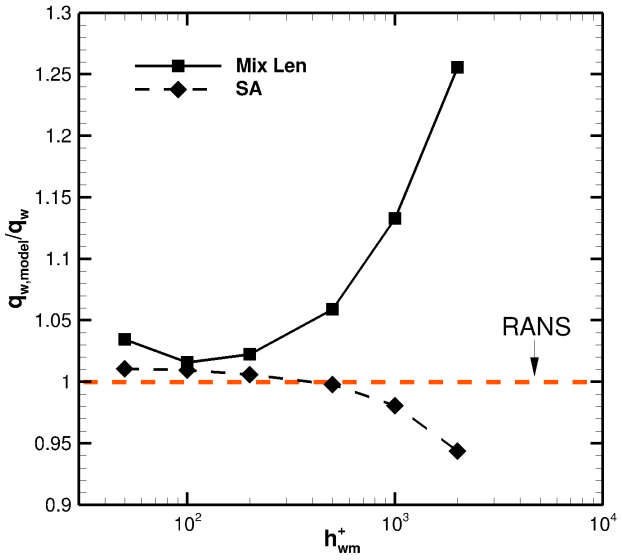

(b) heat transfer

Figure 5.4: Wall fluxes determined by two eddy-viscosity models on HCF at x=0.5m with varying probe heights

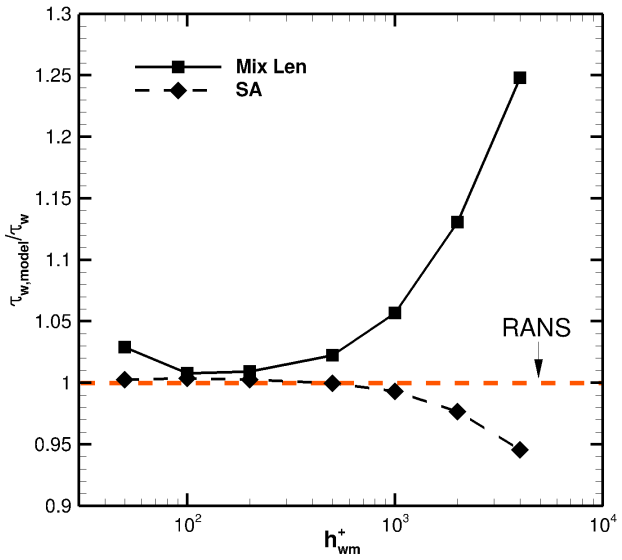

(a) wall shear

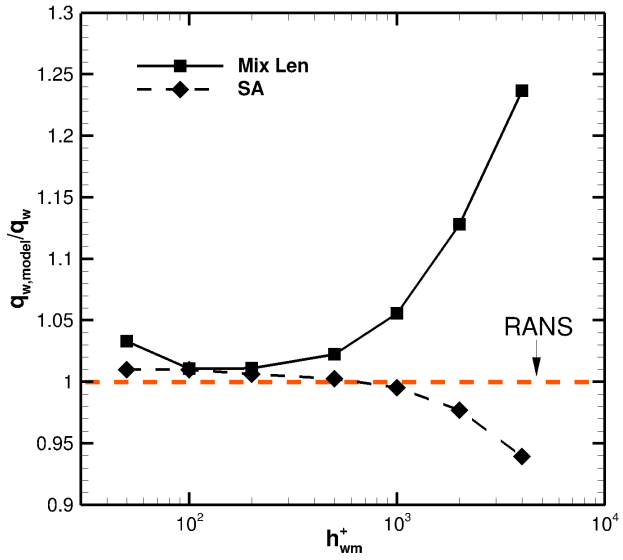

(b) heat transfer

Figure 5.5: Wall fluxes determined by two eddy-viscosity models on HCF at x=1.1m with varying probe heights

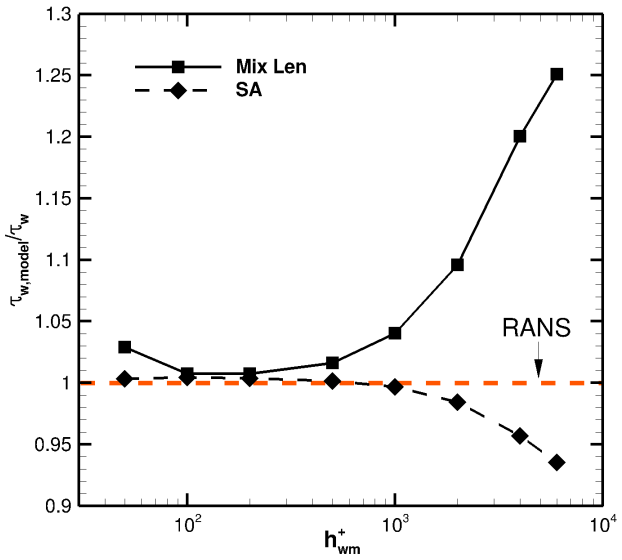

(a) wall shear

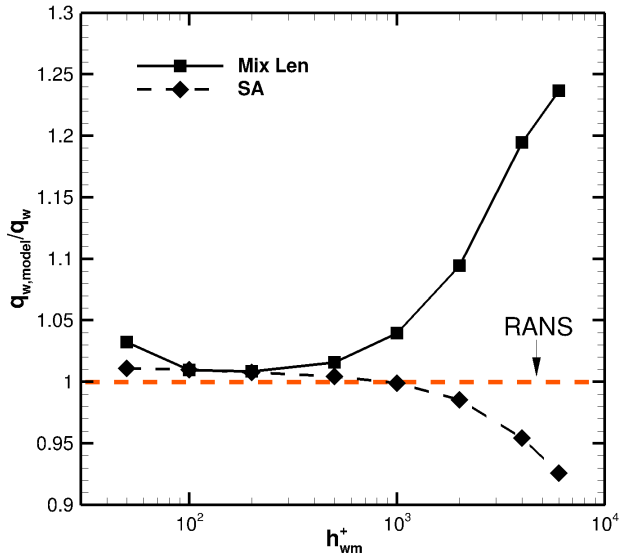

(b) heat transfer

Figure 5.6: Wall fluxes determined by two eddy-viscosity models on HCF at x=1.5m with varying probe heights

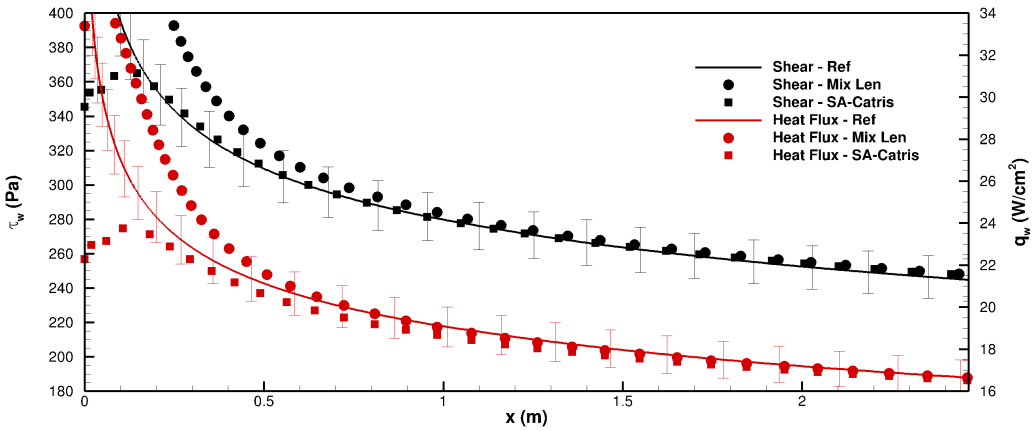

Figure 5.7: Wall-modeled wall shear and heat transfer calculations of HCF geometry compared to resolved calculation

As the boundary layer begins to develop on the hollow cylinder flare the near-wall resolution of the coarse mesh is insufficient to capture the boundary layer in any detail. With a probe location several cells off the wall, it is not until the boundary layer growth reaches the probe cell that the model has any information other than the post-shock freestream data to operate on. In this calculation, this occurs around 0.2 meters downstream of the lip of the cylinder. At this location, the probe is effectively in the defect region of the equilibrium turbulent boundary layer. As discussed in Sec. 5.3.1, the mixing length based model has no ability to predict the defect region, whereas the SA based model retains predictive capability for for probe locations in this region. It is not until the boundary layer grows sufficiently to place the probe cell in the log layer that the two wall model solutions predict the same result.

5.5 Review of Findings

In this chapter, we evaluated the performance of the wall model against a cold-wall test case. The geometry of the problem allowed for a simplification of the wall model to only equilibrium terms, allowing us to examine several factors independent of the

more complicated model terms addressed later in this work. The following are the key take-aways from this chapter:

- The model proposed in Chapter 3 can produce accurate boundary layer profiles and wall quantities by sampling wall-resolved data from an equilibrium cold wall boundary layer.
- Both eddy viscosity formulations proposed in Sec. 3.2 are accurate so long as the probe location is restricted to the log region of the equilibrium boundary layer. As the probe approaches the defect region, the performance of the mixing-length based model deteriorates rapidly while the S-A based model retains predictive capability.
- When integrated with CFD and used on a coarsened mesh, the wall model is able to accurately simulate flow over the hollow cylinder.

Chapter 6

Analysis of Wall Model Source Terms

Many wall-bounded flows of engineering interest violate the assumptions incorporated with equilibrium wall models. Namely, flows with shock waves impinging on boundary layers subject the boundary layer to pressure gradients and inertial imbalances. Similarly, supersonic boundary layers undergoing expansion or compression processes also experience non-equilibrium effects. Separated flows and stagnation point flows also have extensive regions where the boundary layer cannot be described as being in equilibrium.

This chapter examines the balance of forces on a non-equilibrium hypersonic boundary layer. The effects of various choices of wall modeling terms in a RANS sense are discussed.

6.1 Test Geometry and Flow Conditions

The geometry studied in this section is the CUBRC Large Cone Flare (LCF) [3], shown in Fig. 6.1. The cone portion of the LCF is a 7-degree half-angle cone extending 2.35 meters in the axial direction. The cone is then flared 40-degrees and extends 0.15 meters in the axial direction. Test conditions for the chosen experimental run are shown in Table 6.1.

This condition is chosen due to the high Mach number, cold-wall isothermal conditions. The full test article is modeled, which includes the turbulent boundary layer

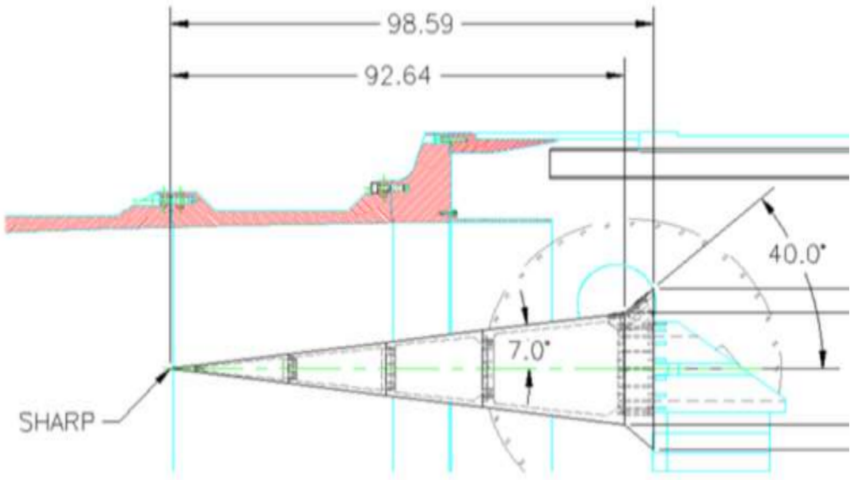

Figure 6.1: Schematic of CUBRC Large Cone Flare, from [3]. Dimensions in inches

Mach	Re_L	T_w/T_0
7.14	52.7×10^6	0.52

Table 6.1: Test condition for CUBRC LENS-XX LCF experiment, run 14 [3]

interacting with the 40-degree flare. This allows us to examine the effect of various model terms in a non-equilibrium boundary layer.

Simulations are conducted in US3D using modified Steger-Warming flux vector splitting [28] with second-order MUSCL on density, velocities, turbulence variable and pressure, gradients evaluated by weighted least-squares, molecular viscosity determined by Sutherland's formula, and turbulent viscosity from the SA-Catris Model [31]. Time integration is accomplished with the DPLR [27] method to drive the flow to steady-state.

The 2-D axisymmetric grids used in this study are detailed in Table 6.2. Isotropic cell density is applied outside of boundary layers with approximate shock alignment. The only difference between the grids used in this study is the near-wall clustering applied to the grids. The wall spacing achieved on several of the grids used in this study is shown in Fig. 6.2. Within the boundary layer, a cell growth rate of eight percent was applied in the wall-normal direction. Detail views showing a comparison of the near-wall clustering used are presented in Fig. 6.3.

Grid	y^+-cone	y^+-flare
Resolved	0.05	0.6
Medium	1.0	12.0
Coarse	4.0	50.0
Very Coarse	8.3	100.0

Table 6.2: Wall-spacing for LCF grids

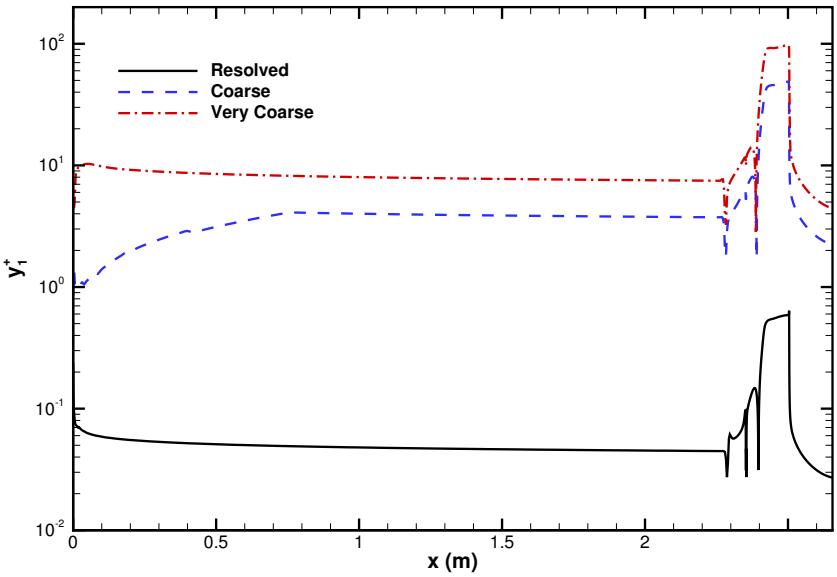

Figure 6.2: Near-wall grid resolution for LCF grids

6.2 Analysis of Wall-Resolved Solution

The LCF flowfield has two distinct regions of interest. The first region is the flowfield produced by the 7-degree cone. The second region is the area where the turbulent boundary layer from the cone impinges on the 40-degree flare. Fig. 6.4 shows the magnitude of the density gradients in the vicinity of the flare. The oblique shock generated by the cone is shown entering the figure from the left, and not interacting with either the flare or the shock generated by the flare. The incoming compressible boundary layer separates in this RANS calculation, with a separation shock apparent which impinges on the flare.

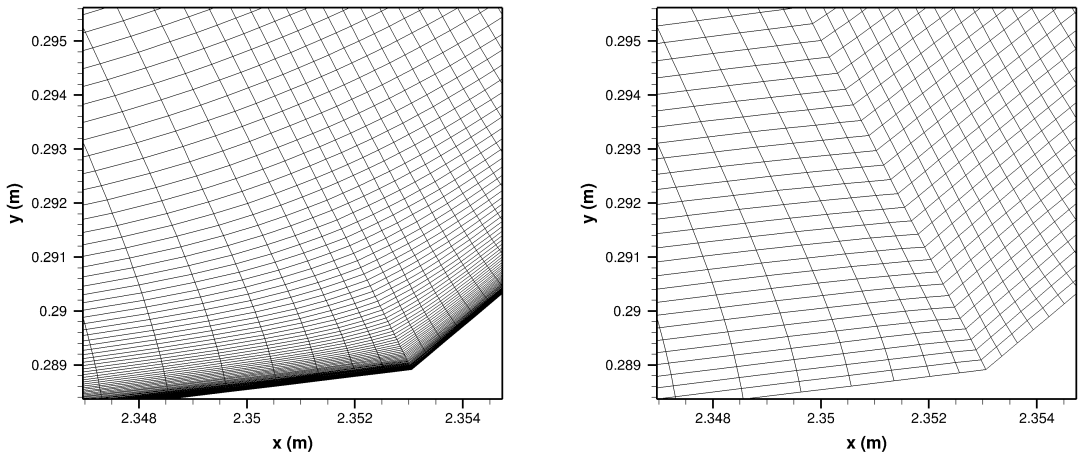

(a) Resolved

(b) Very Coarse

Figure 6.3: Detail view the wall-resolved, and Very Coarse LCF meshes

The wall-resolved result is compared to experimental measurements of heat flux in Fig. 6.5. The transition process on the cone is far more rapid in the RANS than the experiment, but heating levels on the cone compare very favorably between the simulation and the experiment. Agreement is poor in the heating levels on the flare portion of the geometry. The heating profile shown in Fig. 6.5(b) is typical of other S-A RANS calculations in the CUBRC study [3]. Wall-resolved calculations are run both with a trip, and fully turbulent. The wall heat flux is only significantly affected in the vicinity of the trip, and the solution on the flare is insensitive to the use of the trip.

To further assess the necessity of tripping the flow for this investigation, we examine boundary layer profiles of velocity and turbulent viscosity ratio μ_t/μ at two different axial locations in Fig. 6.6. The first axial location is approximately half-way along the cone, 75 centimeters downstream from the onset of transition. The second location is on the flare approximately 5 centimeters before the shoulder and after the STBLI. The velocity profiles shown in Figs. 6.6(a) and 6.6(b) are indistinguishable whether or not the trip is used. The primary difference in the simulations is evident in the profiles of turbulent viscosity ratio. The difference is greatest at the 1.1 meter station shown in Fig. 6.6(c) where the two predictions of peak turbulent intensity differ by approximately 10%. This discrepancy is not unexpected due to the proximity of the trip just upstream

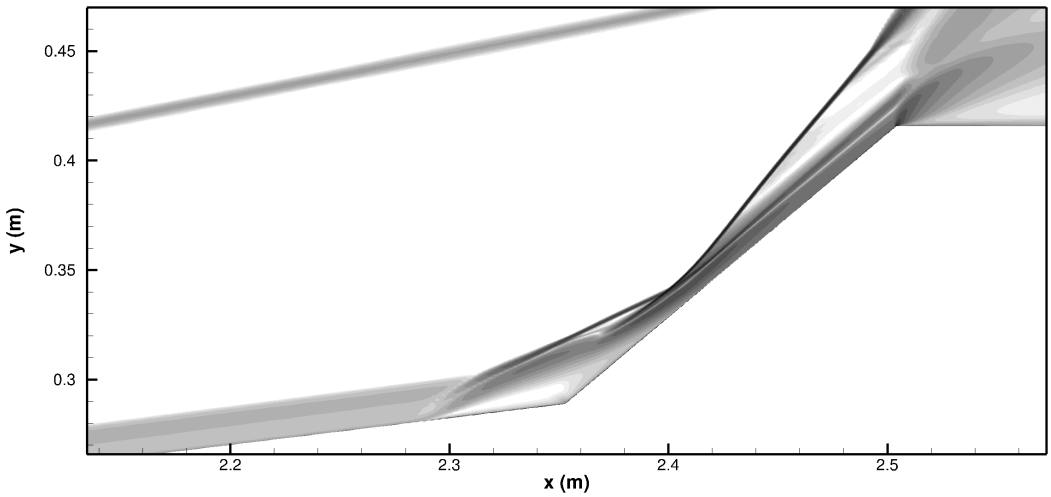

Figure 6.4: Logscale of density gradient magnitude in the flare region of the LCF

of this location. The results closer to the STBLI are of arguably more importance, due to the potential augmentation of turbulence intensity due to freestream turbulence passing through the shock. The results shown in Fig. 6.6(d) indicate that the intensities agree very well between the tripped and un-tripped simulations, with less that a 2% augmentation evidenced.

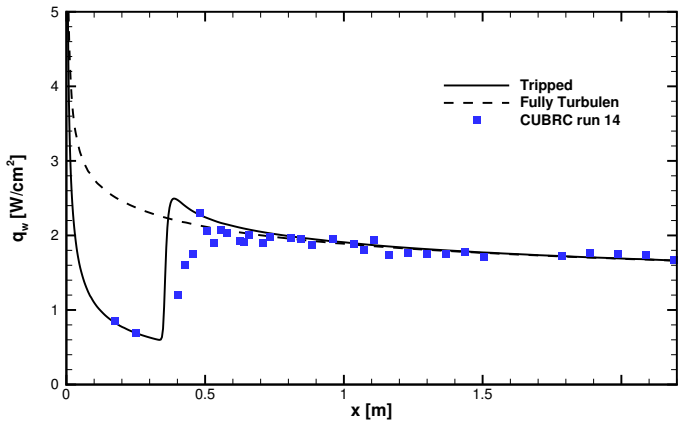

(a) Cone

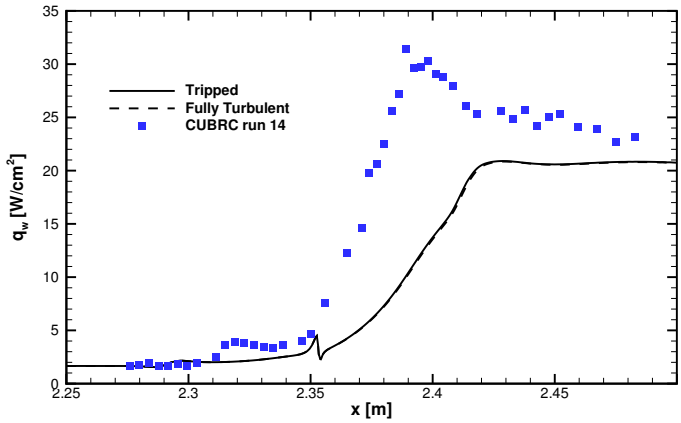

(b) Flare

Figure 6.5: Comparison of resolved SA-Catris result and experimental heating measurements for LCF with and without tripping the flow

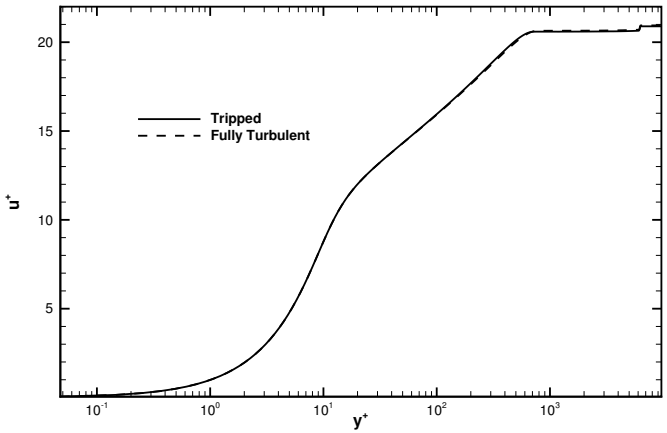

(a) x=1.10 m, velocity

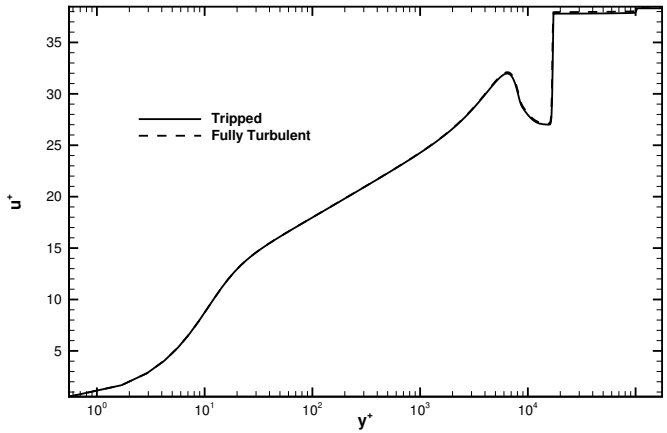

(b) x=2.45 m, velocity

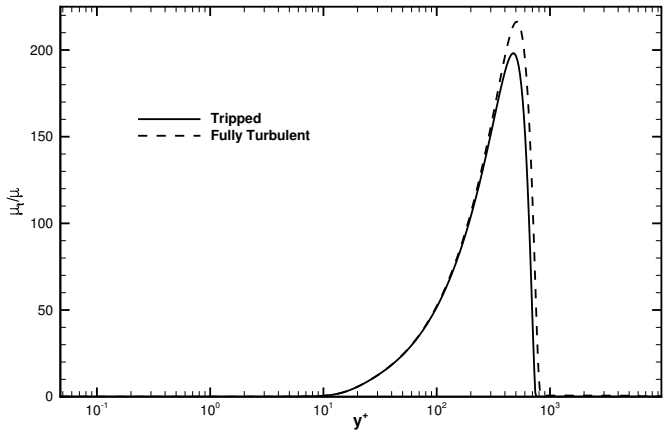

(c) x=1.10 m, turbulent viscosity ratio

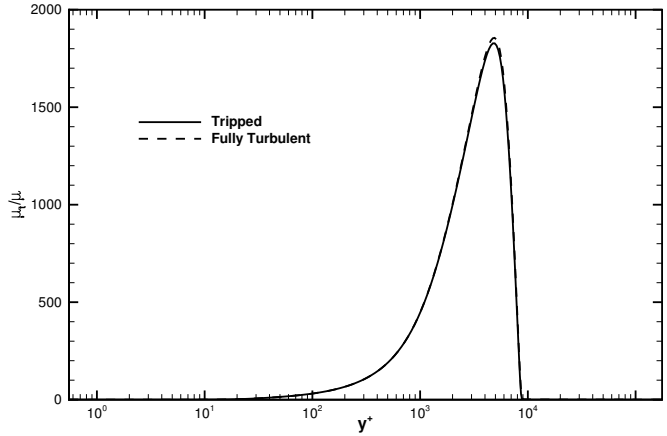

(d) x=2.45 m, turbulent viscosity ratio

Figure 6.6: Comparison of velocity and turbulent viscosity profiles between the tripped and un-tripped flow

For the purposes of this chapter, the performance of the wall model will be compared to the solutions produced by the S-A model on the wall-resolved grid, not the experimental heating levels. The primary interest in this investigation is showing the consistency of the wall-modeled simulations with their wall-resolved counterparts. Additionally, while investigations have been accomplished on wall-modeled grids using a trip, the calculations using the mixing length model for eddy viscosity proved somewhat susceptible to instabilities. For this reason, the simulations presented herein are fully turbulent.

6.3 Effect of Various Terms in Wall-Modeled Solution

Figs. 6.7 - 6.12 compare the effects of the various wall model terms on the prediction of skin friction coefficient and wall heat flux for each of the three modeled grids. Simulations are conducted using both mixing length and the SA-Catris formulations for determining wall model turbulent eddy viscosity. In each of the figures a solid line denotes the solution on the wall-resolved grid without the use of a wall model. The dashed line denotes the solution on the coarsened grid without the application of a wall model. This line bounds the error of the solutions. The wall-modeled solutions are presented as symbols; filled symbols denote solutions using SA-Catris, hollow symbols denote solutions using mixing length. Symbol shapes are used to convey which terms are included in the wall model. Square symbols are solutions using only the equilibrium terms of the wall model, as is used in Chapters 5 and 7. Triangles indicate a simulation that uses the pressure gradient at the probe location as a source term in the wall model. Circles denote solutions using an approximation of the inertial source term detailed in Sec. 3.5.

6.3.1 Eddy Viscosity Formulation

The most significant differences are observed when examining the effect of eddy viscosity formulation. All model permutations accurately predict skin friction and heat flux on the cone portion of the geometry, with predictions from mixing length based models slightly elevated from the resolved calculations. On the coarsest grid, all models deviate from the resolved calculation at the tip of the cone, as shown in Figs. 6.11(a) and

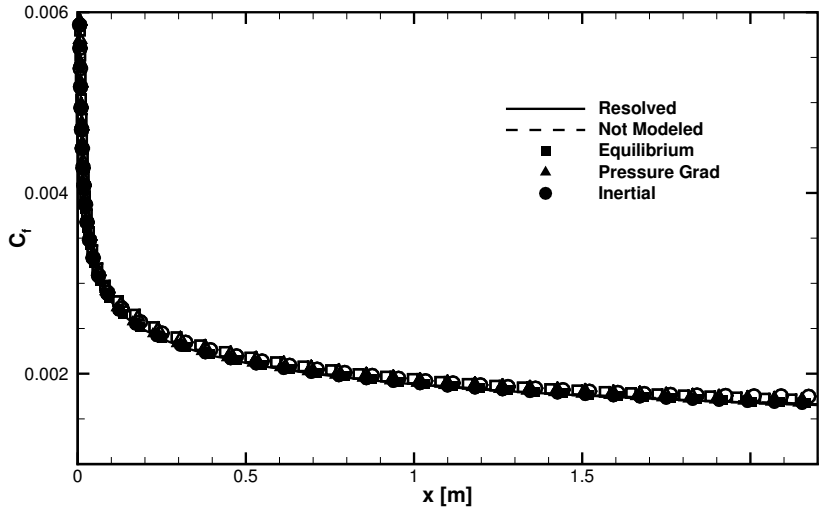

(a) Cone

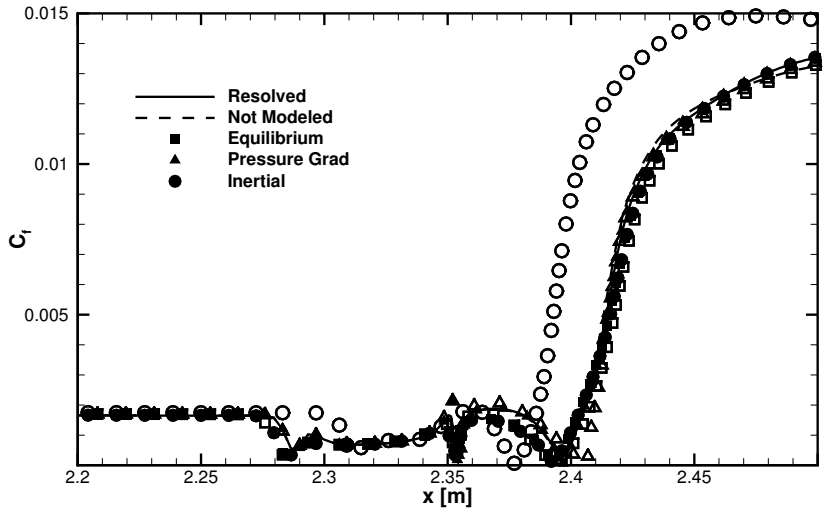

(b) Flare

Figure 6.7: Skin friction coefficient the 1-12 grid. Hollow symbols use mixing length for eddy viscosity, filled symbols use SA-Catris

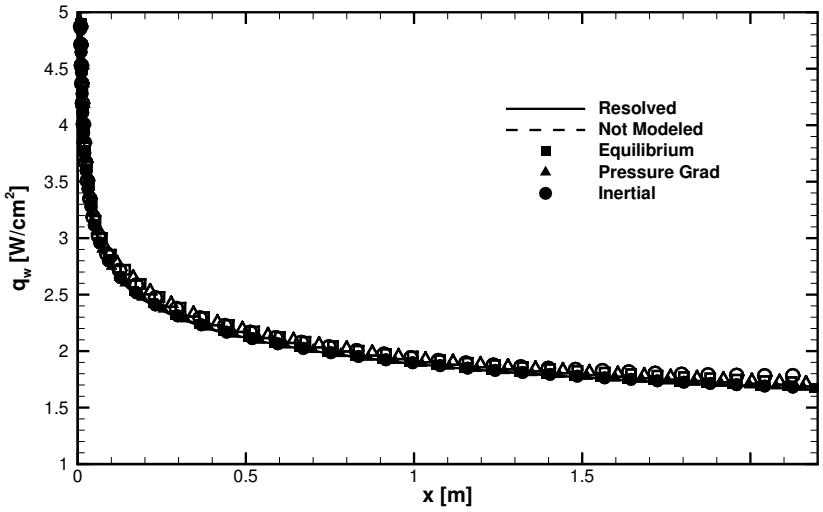

(a) Cone

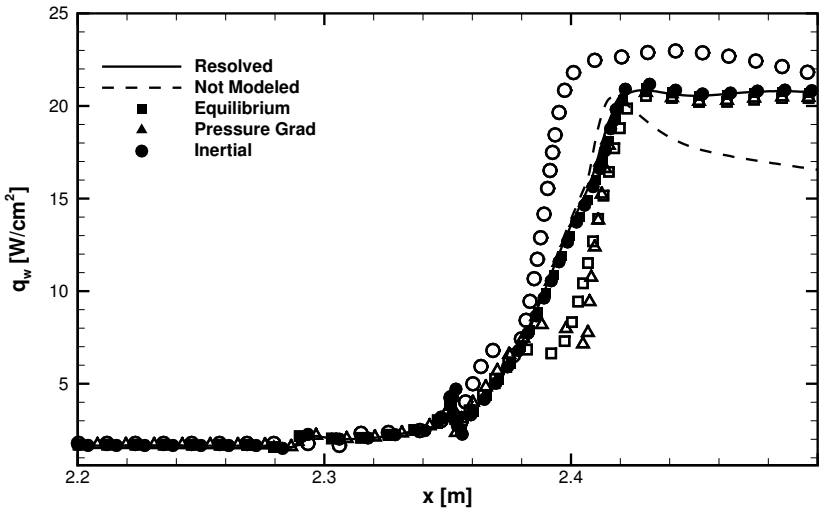

(b) Flare

Figure 6.8: Wall heat flux for the 1-12 grid. Hollow symbols use mixing length for eddy viscosity, filled symbols use SA-Catris

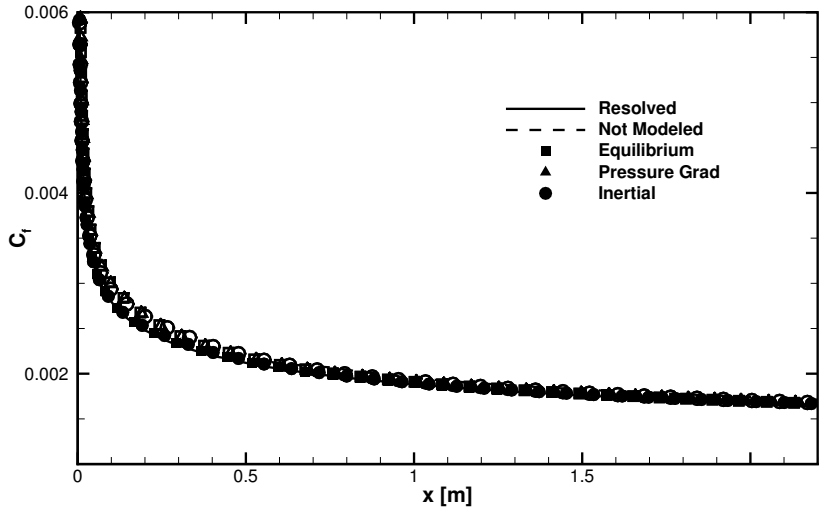

(a) Cone

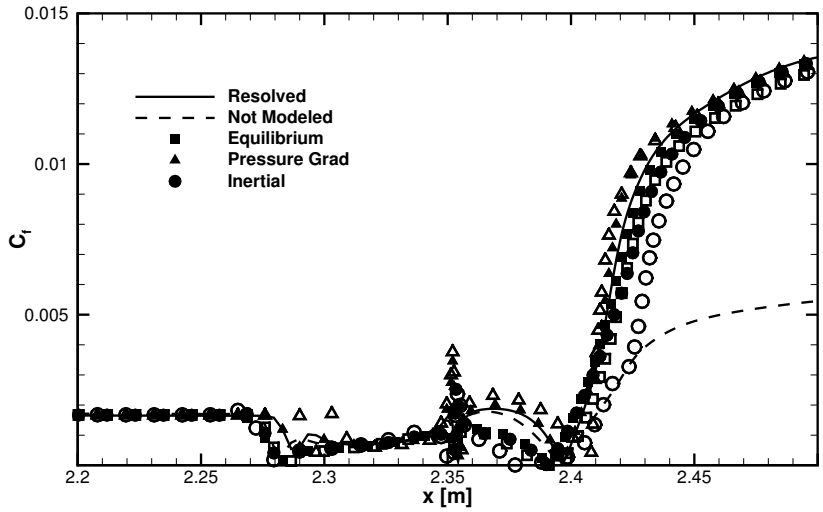

(b) Flare

Figure 6.9: Skin friction coefficient the 4-50 grid. Hollow symbols use mixing length for eddy viscosity, filled symbols use SA-Catris

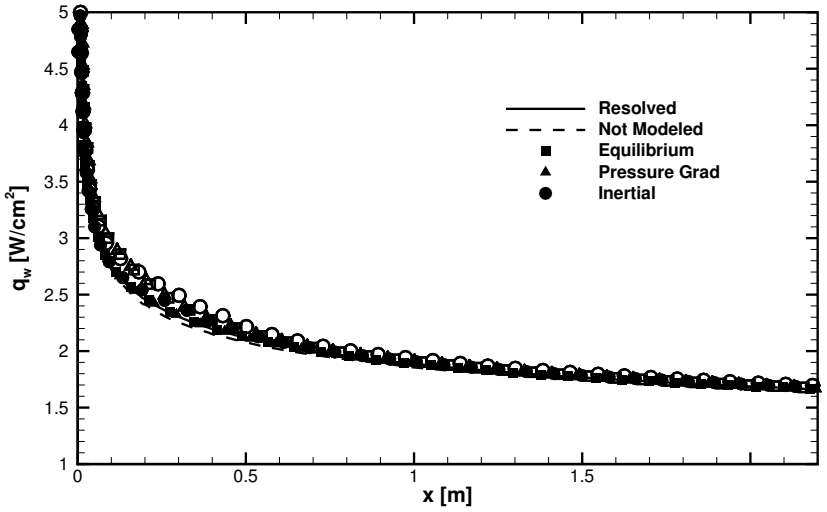

(a) Cone

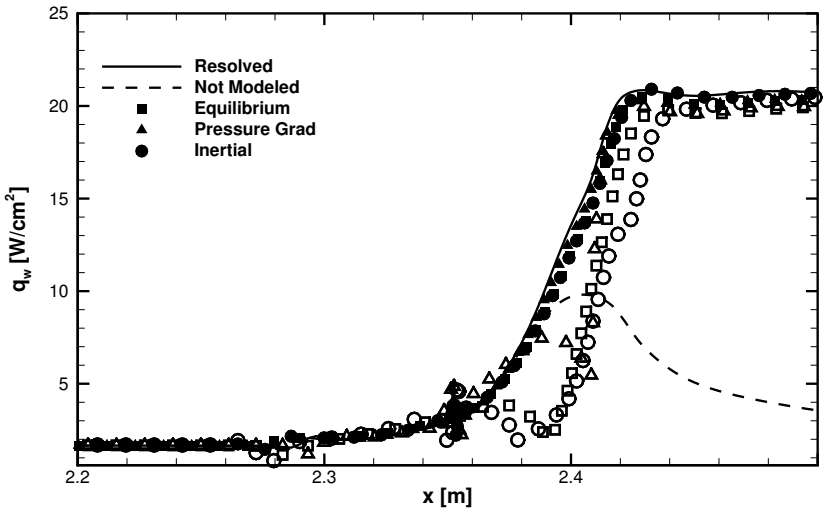

(b) Flare

Figure 6.10: Wall heat flux for the 4-50 grid. Hollow symbols use mixing length for eddy viscosity, filled symbols use SA-Catris

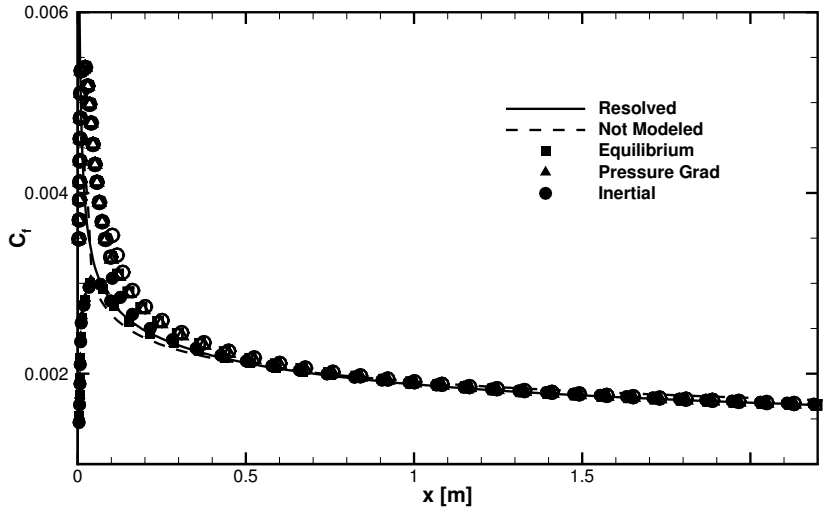

(a) Cone

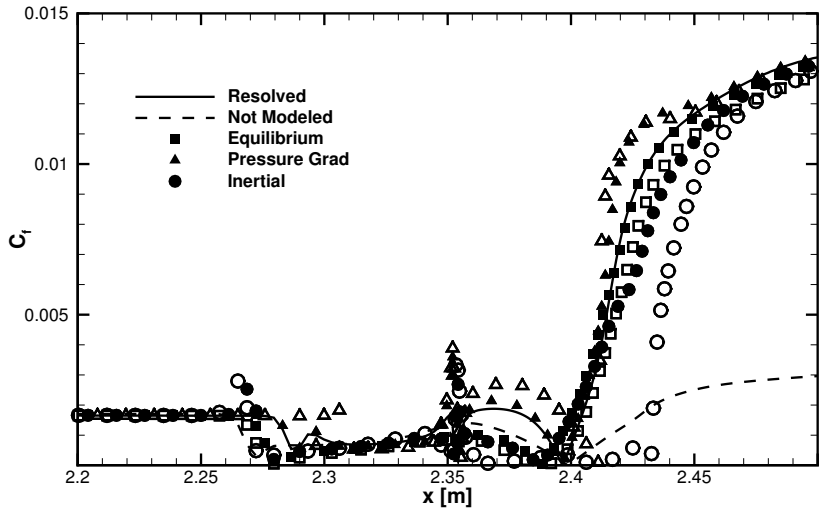

(b) Flare

Figure 6.11: Skin friction coefficient the 8.3-100 grid. Hollow symbols use mixing length for eddy viscosity, filled symbols use SA-Catris

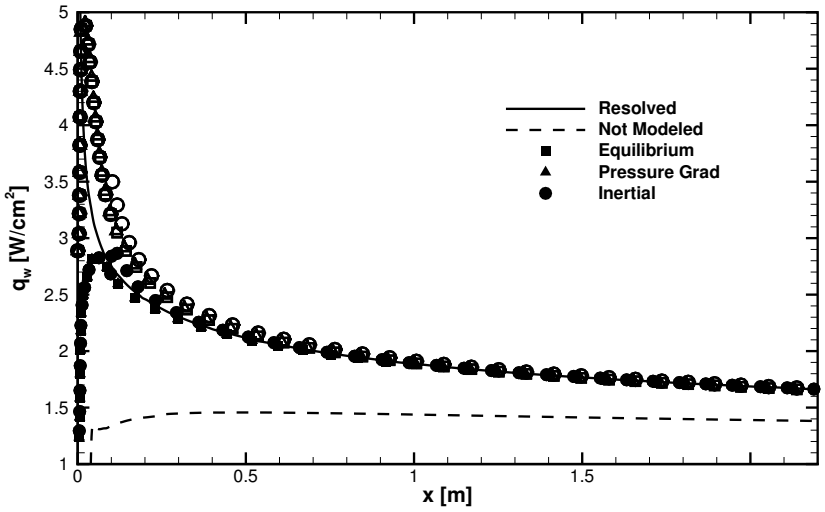

(a) Cone

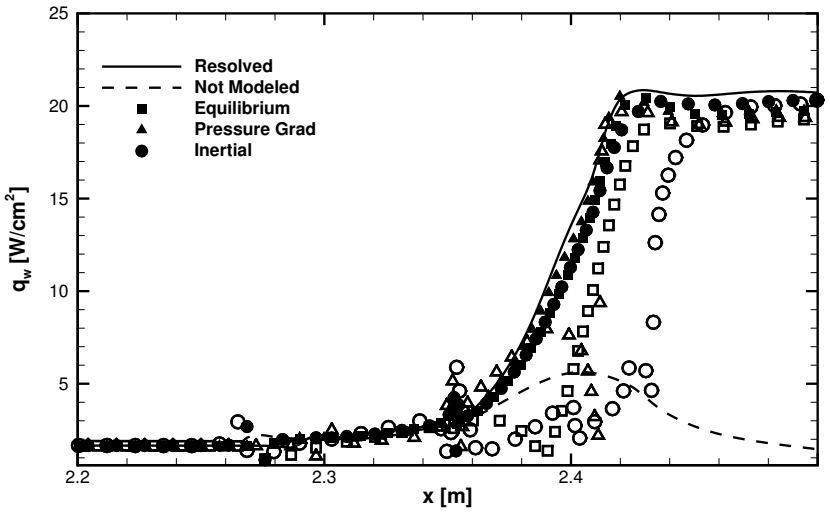

(b) Flare

Figure 6.12: Wall heat flux for the 8.3-100 grid. Hollow symbols use mixing length for eddy viscosity, filled symbols use SA-Catris

6.12(a). This effect is also observed in Sec. 5.4, and is due to the boundary layer not appropriately interacting with wall model probe location.

On the flare, the effect of eddy viscosity formulation is more pronounced. Examining subfigure (b) of Figs. 6.9 - 6.12 it is clear that the simulations using the mixing length eddy viscosity formulation deviate significantly from the resolved solution, and show much poorer agreement than the comparable simulations which use SA-Catris for eddy viscosity.

The reason for the poor performance of the mixing-length model is attributable to the very high turbulent viscosity present over the flare, shown in Fig. 6.13. The incoming turbulent boundary layer on the cone is compressed by the flare, greatly elevating turbulence intensities beyond that of a zero pressure gradient flat plate, on which the mixing length model is based. The mismatch in eddy viscosities between the resolved flow and the wall model introduces significant error in the determination of wall shear and heat flux.

Given the fundamental issues with the mixing length based model being used in this RANS calculation, very little information can be gained by examining the influence of other model terms. For this reason, the rest of this chapter will focus on the analysis of the wall model using the SA-Catris equation to determine eddy viscosity.

6.3.2 Equilibrium Terms

The equilibrium wall model accurately predicts skin friction coefficient and heat transfer on the cone portion of the geometry on all grids used in this study. The solutions on the flare are more dependent on grid resolution than the solutions on the cone.

Table 6.3 compares the flow separation and re-attachment points at the cone-flare juncture using the equilibrium based model. The trend is for the separation bubble to shrink as the grid is coarsened. Additionally, the separation point moves forward with the use of the equilibrium wall model.

Finally, there is a gradual reduction in shear predicted on the flare as the grid is coarsened, as well as a reduction in peak heating levels on the flare. It is noted that these effects are slight, and the results from the equilibrium applied to all grids are in close agreement with the resolved calculation, despite the grids being coarsened by one to two orders of magnitude.

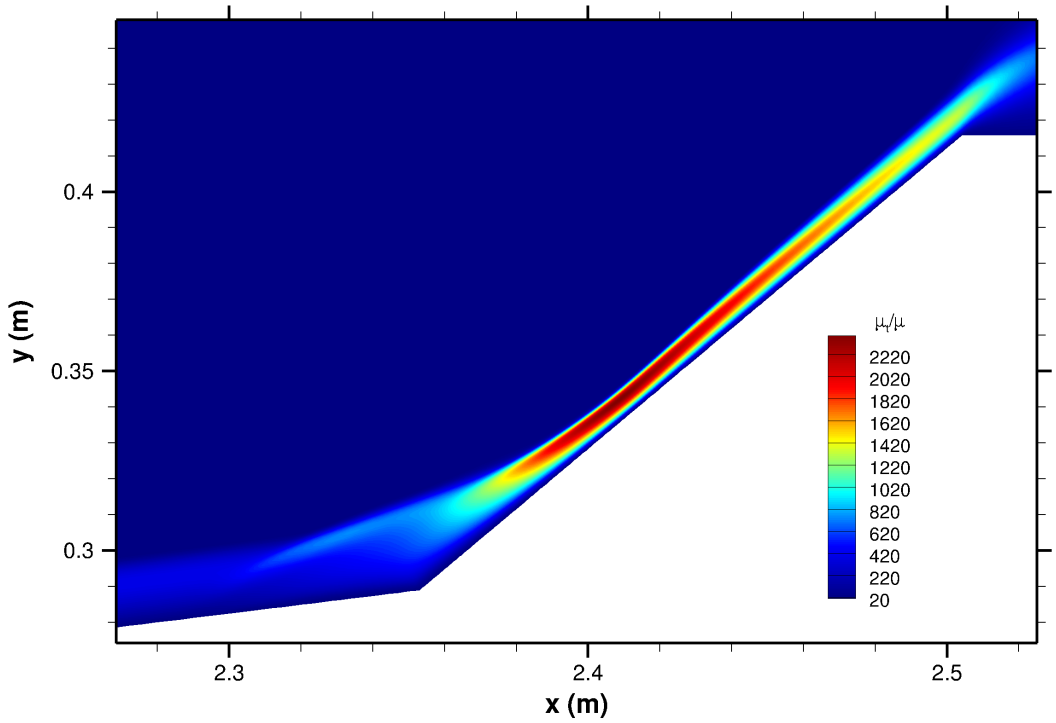

Figure 6.13: Ratio of effective turbulent viscosity to molecular viscosity over flare portion of LCF on resolved grid

6.3.3 Pressure Gradient

The wall model with pressure gradient included as a source term accurately predicts skin friction coefficient and heat transfer on the cone portion of the geometry on all grids used in this study. The solutions on the flare are more dependent on grid resolution than the solutions on the cone.

Table 6.4 compares the flow separation and re-attachment points at the cone-flare juncture using the wall model with pressure gradient source term. The wall model exactly reproduces the location of separation onset and length of separation from the resolved simulation on all grids used in this study.

The wall model with pressure gradient source term increasingly overpredicts skin friction on the flare following reattachment as the grid is coarsened. The predicted heat transfer after reattachment very closely follows the rise in heating observed in the resolved calculation, but on both the Coarse and Very Coarse grids it plateaus before

Grid	x_{sep} (cm)	x_{att} (cm)	L_{sep} (cm)
Resolved	228.7	239.7	11.0
Medium	227.9	238.8	10.9
Coarse	228.3	239.1	10.8
Very Coarse	228.3	238.8	10.5

Table 6.3: Details of separation at LCF cone-flare juncture for equilibrium wall model

Grid	x_{sep} (cm)	x_{att} (cm)	L_{sep} (cm)
Resolved	228.7	239.7	11.0
Medium	228.7	239.7	11.0
Coarse	228.7	239.7	11.0
Very Coarse	228.7	239.7	11.0

Table 6.4: Details of separation at LCF cone-flare juncture for wall model with pressure gradient

the peak heating level observed on the resolved grid. The peak heating on the Coarse grid is 2.5% less than that of the resolved grid, while the peak heating on the Very Coarse grid is 5.1% less than that of the resolved grid.

6.3.4 Inertial Terms

The wall model with approximate inertial source terms accurately predicts skin friction coefficient and heat transfer on the cone portion of the geometry on all grids used in this study. The solutions on the flare are more dependent on grid resolution than the solutions on the cone.

Table 6.5 compares the flow separation and re-attachment points at the cone-flare juncture using the wall model with inertial source terms. The wall-modeled solutions have a separation point that increasingly shifts forward as the grid is coarsened. Also as the grid is coarsened, the length of separation diminishes, but not to the same extent as is seen in the equilibrium wall model results.

In the region of the flare after reattachment, the wall model with inertial source term generally underpredicts skin friction coefficient and heat flux. Once the heat flux plateaus, however, the predicted values of heat flux are within 3% of the values on the resolved grid.

Grid	x_{sep} (cm)	x_{att} (cm)	L_{sep} (cm)
Resolved	228.7	239.7	11.0
Medium	228.4	239.3	10.9
Coarse	228.3	239.0	10.7
Very Coarse	228.0	238.7	10.7

Table 6.5: Details of separation at LCF cone-flare juncture for wall model with inertial terms

A closer examination of streamwise velocity boundary layer in the vicinity of the cone-flare junction is shown in Fig. 6.14. This figure compares the solution of the wall model with various model terms agains the resolved calculations at four stations. The left-most profile is taken on the cone just prior to separation. All model variants produce the same solution and the profile resembles a classical turbulent boundary layer. The second profile is just after separation. Note that the result including pressure gradient produces the correct profile while the results using either equilibrium terms or all inertial terms are nearly identical. The same is true for the next two profiles which present the flow just prior to and just after reattachment on the flare.

The fact that the solution with only equilibrium terms and the solution with all inertial terms produce nearly identical solutions in the vicinity of separation suggests that, at the probe location, the inertial terms nearly balance and that the source term is effectively zero for the inertial model. This does not match the solution observed in the resolved calculation or the modeled calculation with pressure gradient source term, where it appears that viscosity alone balances the pressure gradient in the inner layer. Regardless of the reason, it is clear that convective term modeled as described in Sec. 3.5 fails in the vicinity of compression-induced separation, and in general does not increase the accuracy of the calculation.

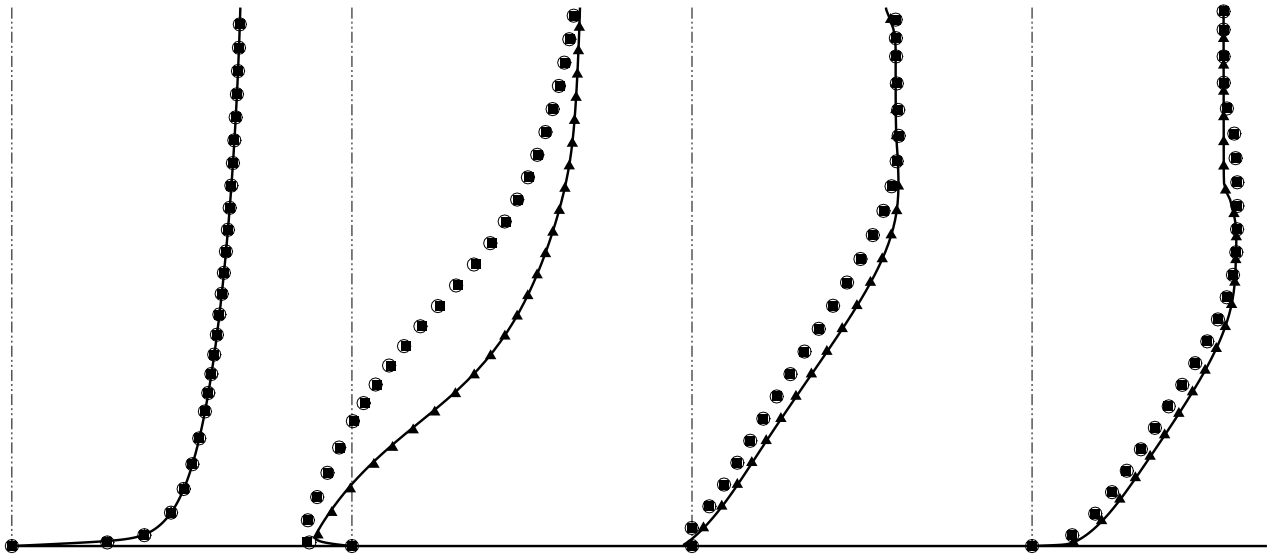

Figure 6.14: Streamwise velocity profiles at four stations on LCF. Prior to and after separation, and prior to and after reattachment. Solid line denotes resolved calculation, square symbol equilibrium model, triangle model with pressure gradient, open circle model with complete inertial term

6.4 Conclusions

Wall-modeled RANS calculations were conducted on the CUBRC LCF geometry at a high Reynolds number cold wall condition. All wall model variants produced accurate levels of skin friction coefficient and heat transfer on the cone portion of the geometry when compared to the wall-resolved RANS calculation using the SA-Catris turbulence model. Evaluation of the results at the cone-flare juncture and over the flare itself revealed significant insight in how the various wall model terms influenced the solution.

When compared to the wall model results using SA-Catris for eddy viscosity, the model that used mixing length produced spurious results. This stems from the fact that the turbulent viscosity intensities convecting from the cone onto the flare are significantly augmented by the compression process the boundary layer experiences. This results in turbulent viscosity levels inconsistent with the mixing length model, which is based on zero pressure gradient flow. The results from the wall model when using SA-Catris for eddy viscosity are consistent with the resolved results since the S-A variable in the freestream is used as a boundary condition in the solution of the wall-modeled SA-Catris equation.

Wether or not an LES of this flow would show the same error with the mixing length model is unclear, and should be the subject of future study. The Reynolds stresses that arise from taking the temporal mean of the Navier-Stokes equations are themselves not a solution of the un-averaged governing equations. While it may be accurate to say that a RANS-based wall model should use an eddy viscosity that is consistent with the RANS parent calculation, the same is not necessarily true for a RANS-based wall model used in a time-accurate flow.

Considering only the wall-modeled results from the SA-Catris eddy viscosity case, the wall-modeled results with and without source terms subjectively agree very well with the wall-resolved calculation. The equilibrium model very accurately predicts skin friction on the flare, but misrepresents the size and location of separation. Including the pressure gradient source term allows the wall-modeled calculation to exactly replicate the wall-resolved separation. In addition, the heat flux rise predicted in this case matches best with the resolved calculation, but peak heating and skin friction after reattachments are misestimated. Including an approximation of the convective source term results in

better estimation of peak heating, however the predicted separation is no more accurate than the equilibrium case. Additionally the rise in skin friction and heating on the flare after reattachment lag the resolved solution.

The results from this chapter suggests that while apparent, the effects of the non-equilibrium source terms on the solutions is slight. Recent DNS results from Coleman *et al.* [32] of Couette-Poiseuille flow support this assertion by showing the effect of pressure gradient to be slight on the mean velocity at a y^+ of 50. Bermejo-Moreno *et al.* [33] showed favorable agreement with experiment using an equilibrium-based wall model for incipiently separated flow at a STBLI. Their results suggest that the sum of the non-equilibrium terms in a turbulent boundary layer may be nearly zero, even if the terms themselves are not.

The present results supports the assertion by Larsson *et al.* [34] that equilibrium models may have utility in non-equilibrium flows given sufficient resolution in the outer region of the boundary layer. In a properly resolved wall-modeled calculation, 80% of the boundary layer is properly resolved and able to experience non-equilibrium effects, the authors state. The portion of the boundary layer that is modeled is dominated by viscous forces, and all inertial terms approximately balance.

Chapter 7

Validation with Large Eddy Simulation

7.1 Overview

Once the performance of the model with equilibrium terms has been established in a RANS calculation, it is of interest to assess the performance of said model in a Large Eddy Simulation. In the context of an LES, a preponderance of the computational burden stems from the restrictive timestep of the near-wall cells. Relaxing the grid spacing by an order of magnitude should allow for a wall-modeled calculation to achieve the same level of statistical convergence as a wall-resolved calculation an order of magnitude faster, in terms of computation time. While there will also be a savings in the number of computational elements in the wall-modeled calculation, a majority of the computational elements lie outside the viscous sub-layer of a boundary layer, with sizes limited by the integral length scale of the flow.

This chapter will examine the behavior of the wall model with the solver operating as an LES. Turbulent structures will be synthetically generated based on a RANS profile and allowed to spatially and temporally develop. The work presented in this chapter was an extensive collaboration with Anand Kartha, whose technical support made this simulation possible. The digital filtering technique discussed in Sec. 7.3 was developed and implemented by Mr. Kartha, but it is discussed here to provide the reader sufficient detail on the methodology of these simulations.

Re_θ	M_e	δ_{99} [mm]	θ [mm]	U_e [m/s]	Source
5,000	2.3	11.0	0.96	550.0	Souverein *et al.* [5]

Table 7.1: Flow conditions of LES validation

direction	extent
x	50 δ_{99}
y	10 δ_{99}
z	4 δ_{99}

Table 7.2: Domain sizes for LES grids

7.2 Test Geometry and Flow Conditions

A necessary but insufficient condition for a wall model to produce accurate LES results of STBLI flows is for the model to produce accurate turbulent boundary layers for equilibrium flows. All simulations in this chapter will be for fully-developed turbulent boundary layers over a zero pressure gradient flat plate. The conditions used for these simulations are given in Table 7.1.

Two-dimensional RANS simulations were conducted using the S-A Catris [31] turbulence model with the freestream conditions of the experiments in Table 7.1. Boundary layer profiles were extracted from the RANS data just upstream of the point where the boundary layer grew to the specified thickness. These profiles were used as the upstream inflow boundary condition for the LES calculations.

Grids for the LES calculations were constructed as a cartesian mesh with regular spacing and smooth stretching. The grids had constant spacing in the streamwise (x) and spanwise (z) directions. The grid in the wall normal (y) direction was created by establishing a specific height of the first cell, and then smoothly growing at a 5% growth rate to a constant farfield spacing. This spacing was maintained for five boundary layer heights above the wall, and then rapidly stretched (20% growth rate) for another five boundary layer heights. The domain extents for the LES grids is given in Table 7.2 and the grid spacing is given in Tables 7.3 and 7.4. A representative view of the near wall grid spacing for each grid is shown in Fig. 7.1.

The flow is modeled as periodic in the spanwise direction. Streamwise boundaries are supersonic turbulent inflow and supersonic outflow. The wall is treated with a

direction	spacing
Δx	$\delta_{99}/24$
Δy_e	$\delta_{99}/40$
Δz	$\delta_{99}/37.5$

Table 7.3: Grid spacing for LES grids

grid	y_1^+
Resolved	0.5
Medium	2.0
Coarse	10.0

Table 7.4: Wall clustering for LES grids

wall-modeled equilibrium isothermal boundary condition at the adiabatic recovery temperature of 281 Kelvin. The reference calculation, which is resolved to the wall, uses an adiabatic boundary condition. The farfield boundary condition was supersonic outflow. The high rate of stretching used near the farfield boundary introduces numerical dissipation to reduce any reflected characteristic from the outflow boundary.

Time advancement in the LES calculations is accomplished with a third-order Runge-Kutta (RK3) scheme. Inviscid fluxes are evaluated with the sixth-order kinetic energy consistent method of Subbareddy and Candler [35] with the limiter by Ducros [36] applied to introduce dissipation to maintain stability near shocks. Subgrid scale stresses are determined using the model by Vreman [37]. The generation of turbulent inflow is described in the next section.

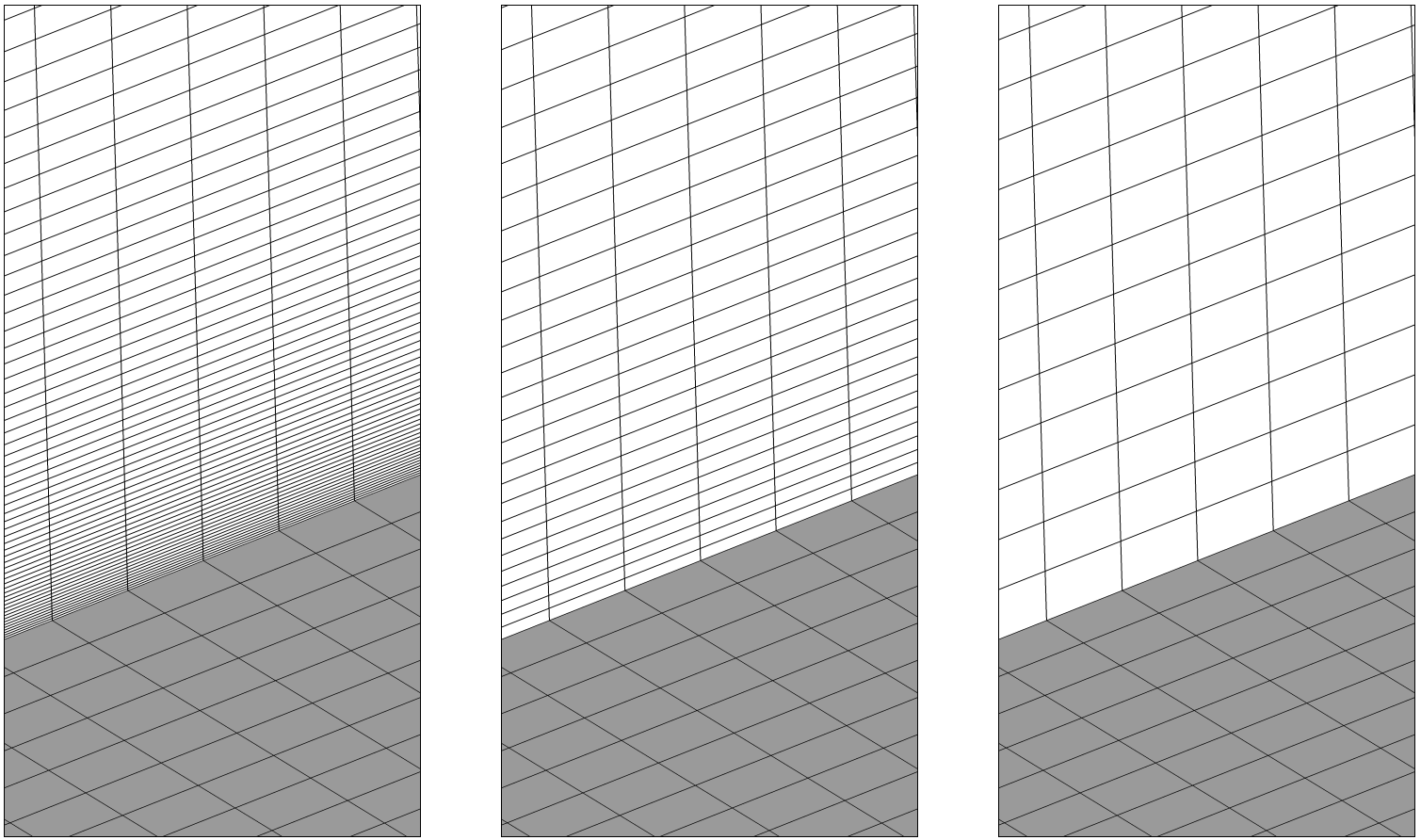

(a) resolved (b) medium (c) coarse

Figure 7.1: Schematic view of LES grids. Shaded region is the wall face, unshaded region is the periodic boundary

7.3 Generation of Inflow Turbulence

The digital filtering technique used by Kartha *et al.* [38] was adapted for use in this work. In this method, inflow perturbations are generated to reproduced prescribed Reynolds stresses. These perturbations are added to the mean RANS profile to generate a time varying inflow with appropriate Reynolds stresses. The review papers by Wu [39] and Dhamankar *et al.* [40] provide an excellent overview on the prescription of inflow turbulence.

To appropriately synthesize a wall-bounded turbulence, the inflow must be set to provide time varying disturbances at appropriate length scales and amplitudes. In the temporal mean, these fluctuations should reproduce the Reynolds-averaged turbulent eddy viscosity that was prescribed at the inflow. Spatially, the distribution of the disturbances should adhere to an appropriate integral length scale representative of turbulent boundary layers. Two general philosophies exist in the literature as to the most appropriate way to prescribe integral length scales at the inflow. The first uses a constant length scale throughout the boundary layer, while the second method varies the length scale based on distance to the wall. There are advantages and disadvantages to both approaches. In this work, the prescribed integral length scale diminishes near the wall. Figs. 7.2 and 7.3 show the prescribed velocity correlation at the inflow compared with the average of the computed correlations at several heights in the inflow boundary layer. Some deviation is observed between the prescribed and computed quantities, but in general they are in very good agreement. The integral length scale is related to the velocity correlations as follows:

$$L = \int_0^\infty R_{uu}(r)\mathrm{d}r \tag{7.1}$$

where the velocity correlation in the i direction is defined as:

$$R_{uu} = \frac{\langle u(x_i)u(x_i + r)\rangle}{\langle u(x_i)^2\rangle} \tag{7.2}$$

Degraff and Eaton [6] observed an approximate collapse on time-averaged Reynolds normal stresses for incompressible flows at a wide range of Reynolds numbers using an

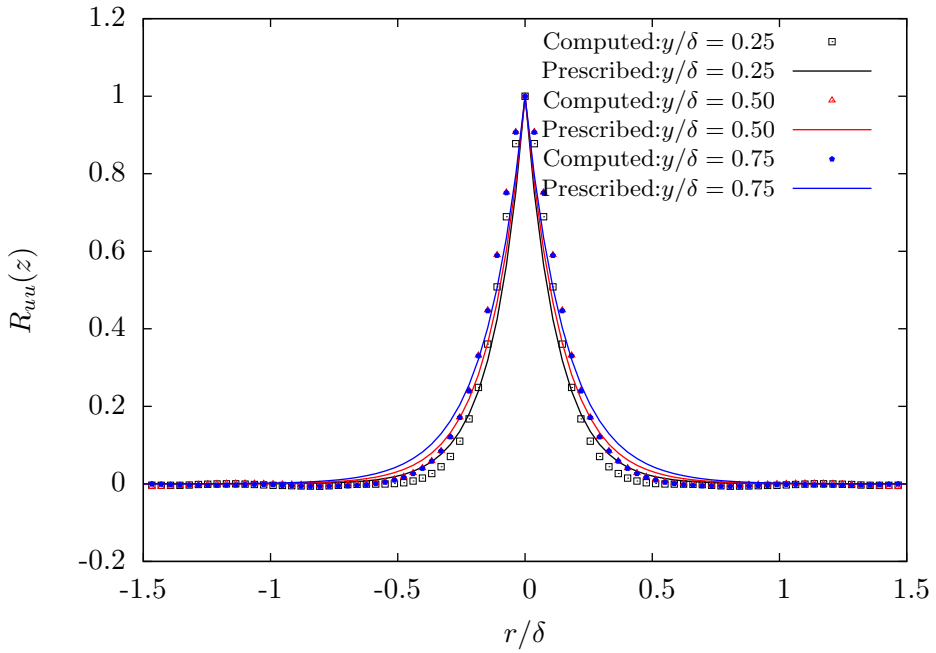

Figure 7.2: Distribution of inflow integral length scales in the spanwise direction

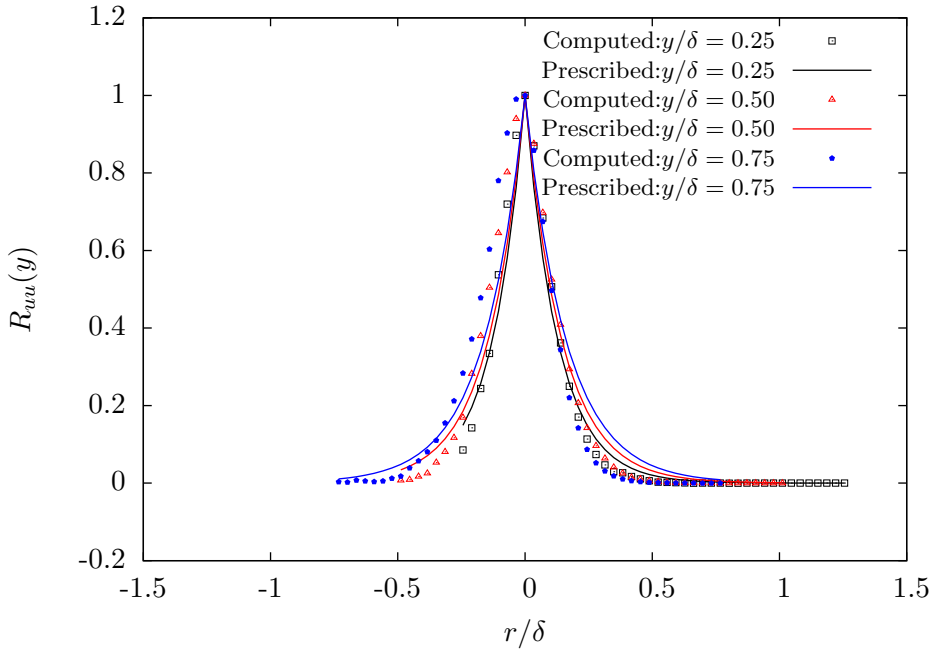

Figure 7.3: Distribution of inflow integral length scales in the wall-normal direction

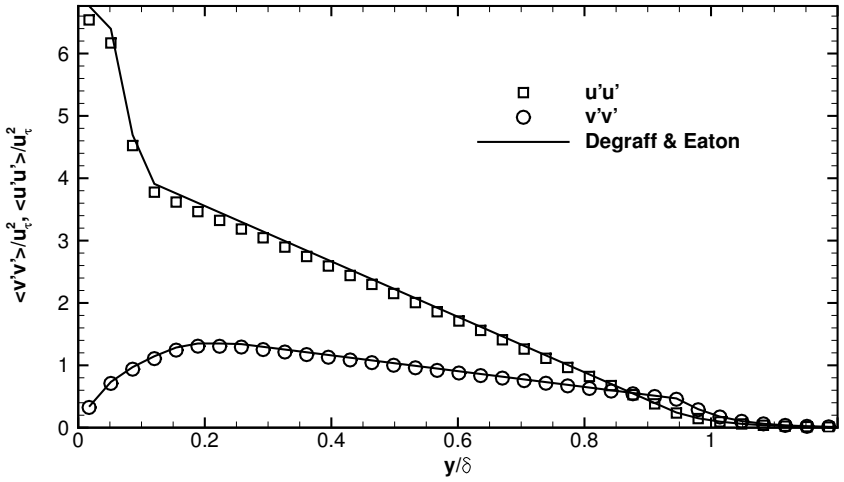

Figure 7.4: Inflow turbulence Reynolds stresses

'inner-outer' scaling. The mean velocity perturbation is normalized by the square of the friction velocity $u_\tau = \sqrt{\tau_w/\rho}$ while the distance from the wall is scaled by boundary layer height δ_{99}. To apply this profile to a compressible boundary layer, Morkovin scaling was applied to weight the incompressible Reynolds stress by $\sqrt{\rho_w/\rho}$ [41]. Fig. 7.4 compares the time averaged Reynolds normal stresses at the inflow with the prescribed values based on the characterization by Degraff and Eaton.

Finally, Fig. 7.5 shows the wall-normal velocity perturbations at three different instances for the Mach 2.3 turbulent inflow. At all three instances, the disturbance amplitudes are approximately equal, but the distributions of the disturbances are unique in each instance.

7.4 Analysis

The turbulent simulations are initialized using the RANS inflow profile. The flow is then simulated for approximately five convective flowtimes ($\tau_c = \delta_{99}/U_e$) to allow the synthetic turbulent inflow to flow through the domain and allow start-up transients to subside. From this point statistics are collected for approximately ten convective

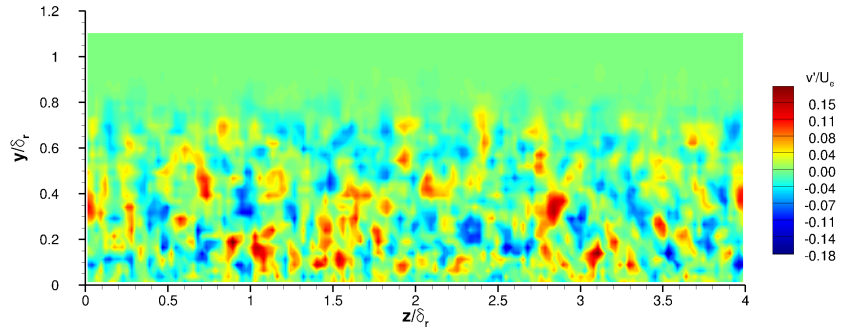

(a) initial

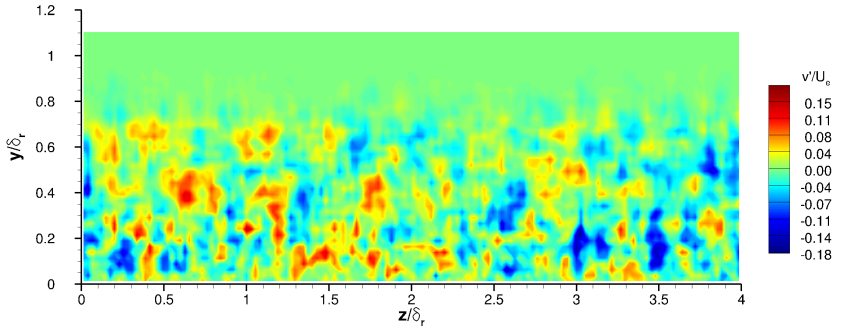

(b) 1 flowtime

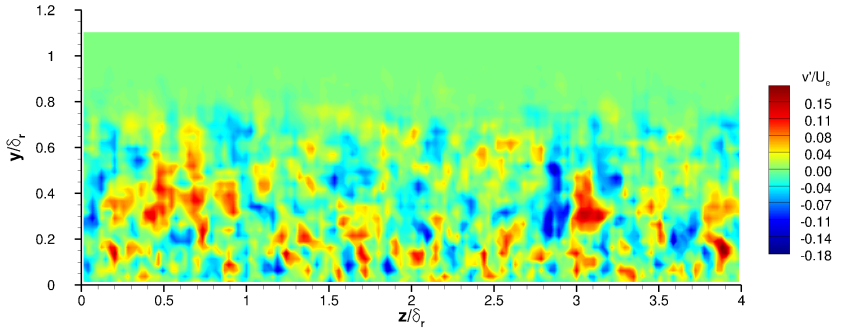

(c) 2 flowtimes

Figure 7.5: Instantaneous wall-normal velocity perturbation for digitally-filtered LES inflow

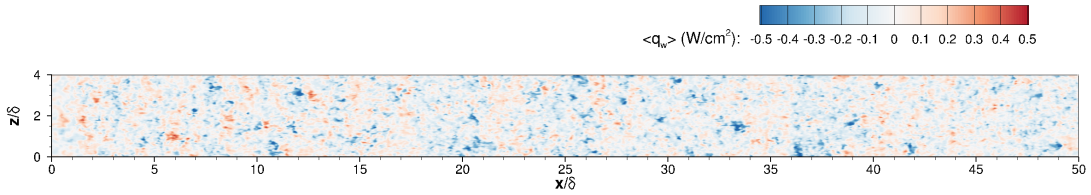

Figure 7.6: Average heat flux on wall boundary for coarse grid with wall model

flowtimes. [1] Volume statistics are collected for flow primitives and Reynolds stresses, and are averaged in the spanwise-direction. Surface statistics are collected as well for wall temperature, pressure, and shear.

Fig. 7.6 shows the average heat flux on the wall boundary for the coarse grid. In the mean, the heat transfer between the wall and the fluid is 0.03 W/cm^2 over the entire plate, however locally the average peaks at $\mathcal{O}(.1)$ W/cm^2. As fluctuating quantities at the surface take the longest time to converge of all turbulent quantities in the simulation, it is expected that with further simulation the statistics would converge to a value near zero.

An instantaneous visualization of wall shear is shown in Fig. 7.7. Flow in the figure is from left to right. Characteristic streaks in wall-shear are evident from larger turbulent structures impinging and lifting off in the wall. Temperature contours in the same figure show the spatial development of the compressible turbulent boundary layer.

An effective technique to visualize the presence and development of turbulent structures is the q-criterion suggested by Hunt *et al.*, [42] given in Eq. 7.3.

$$Q = \frac{1}{2}\left(|S|^2 - |\Omega|^2\right) \tag{7.3}$$

where S is the symmetric strain rate tensor $(\partial u_i/\partial x_j + \partial u_j/\partial x_i)$, and Ω is the vorticity $(\epsilon_{ijk}\partial u_k/\partial x_j)$. Where this criteria falls below a specified threshold, a vortex is said to exist. These structures are evident in Fig. 7.8, which shows vorticies identified by q-criterion colored by instantaneous streamwise velocity.

[1] The wall-resolved results on the fine grid are only converged to approximately $1.5\tau_c$, due to the extremely slow nature of the simulation.

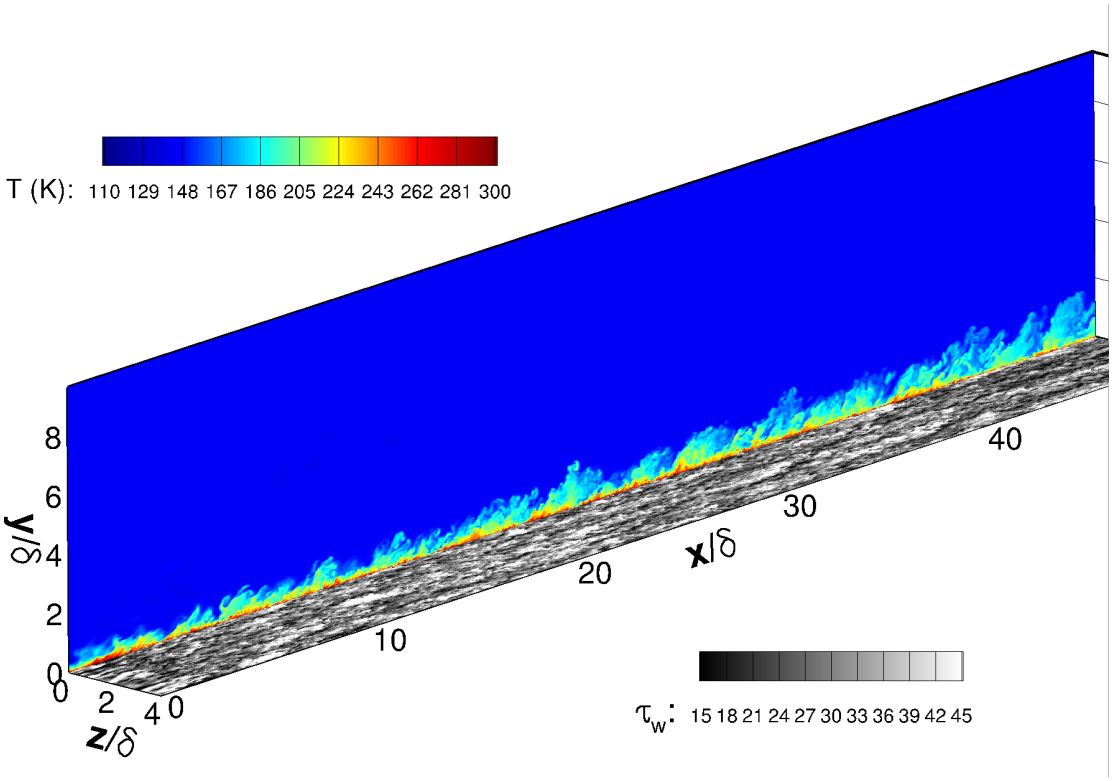

Figure 7.7: Instantaneous wall shear and temperature for $Re_\theta = 5000$ flow over a flat plate at Mach 2.3 on the wall-modeled grid

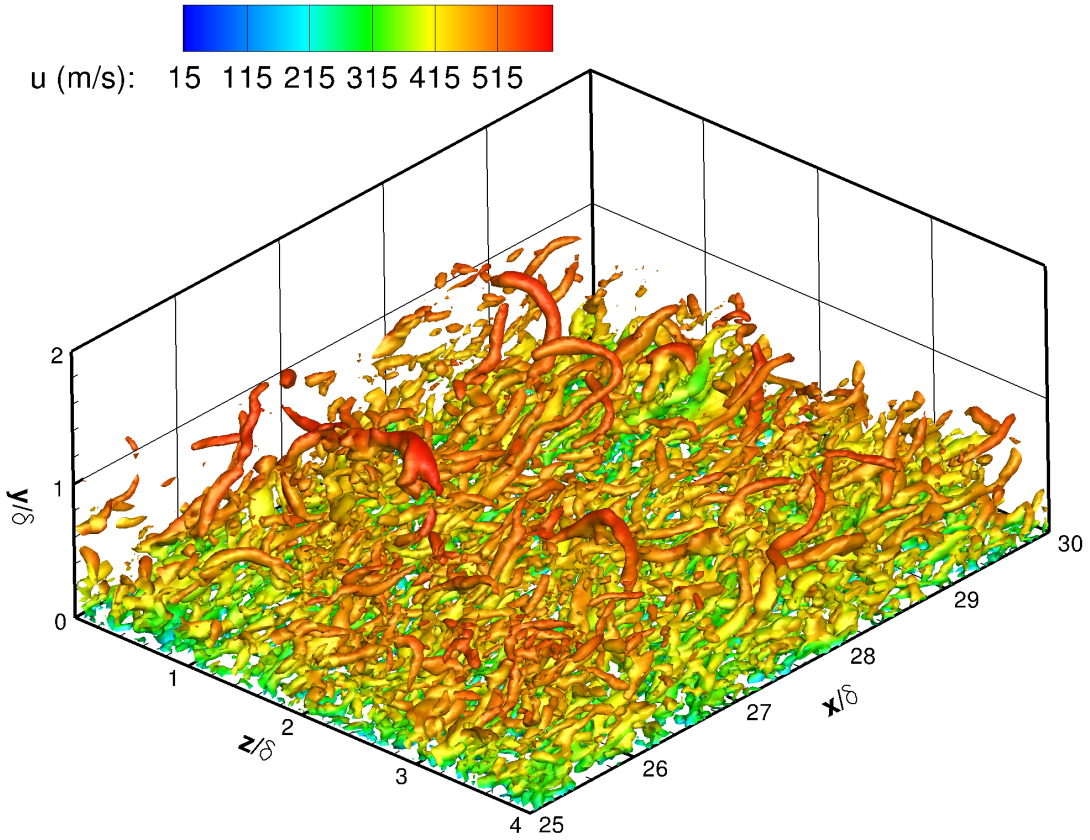

Figure 7.8: Instantaneous q-criterion isosurface for $Re_\theta = 5000$ flow over a flat plate at Mach 2.3

7.4.1 Mean Flow

Fig. 7.9 shows the span-averaged mean velocity distribution at several stream-wise stations. The velocity profile is van Driest transformed to allow for comparison to the classic incompressible law of the wall, given below.

$$u^+ = \frac{1}{\kappa} \log y^+ + C \tag{7.4}$$

where κ and C traditionally assume the values of 0.41 and 5.1 respectively. The two wall-modeled calculations fail to resolve the viscous sub-layer, as it is essentially sub-cell information and only present within the wall model. Both grids produce a log layer, however they are offset from one another due to differences in mean wall shear. The solution from the coarse grid has a log-law constant of slightly over 5.1, as did the experimental measurements of Souverien [5] as well as the wall-resolved simulation. The simulation on the medium mesh has a log-law constant slightly lower that 5.1.

Fig. 7.10 shows the mean computed skin friction coefficient, $C_f = \tau_w / \frac{1}{2}\rho U_e^2$ compared to the power-law fit by White [43] given in Eq. 7.5. The van Driest transformation is applied to compare the compressible boundary layer results with the incompressible fit by White [44]. Error bars of 5% are applied for reference. The predicted skin friction on both the medium and coarse grids are within 5% of White's fit, whereas the coarse grid without application of the wall model underestimates skin friction by almost 10% and is denoted in the figure by a dashed line. The wall-resolved solution produces a skin friction coefficient slightly less than that predicted by White, for which the wall model applied to the coarse grid provides excellent agreement.

$$C_f = 0.020 Re_\delta^{-1/6} \tag{7.5}$$

The simulations have an initial establishment region wherein the skin-friction coefficient is suppressed due to inhomogeneity in the turbulent boundary layer above. After the establishment region, the simulated skin friction coefficient decays at a rate consistent with the one-sixth power law. The simulation on the coarse mesh without application of the wall model underpredicts the average skin friction coefficient, as is expected due to inaccuracies in derivative approximations on the unmodeled boundary.

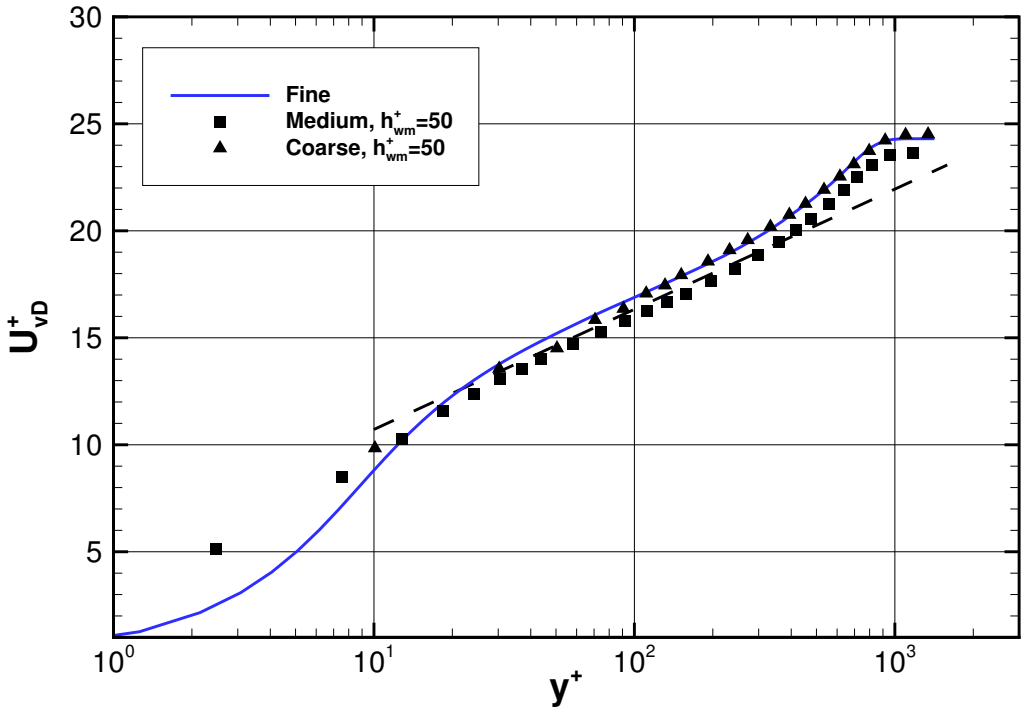

Figure 7.9: Flat plate van Driest-transformed velocity profiles

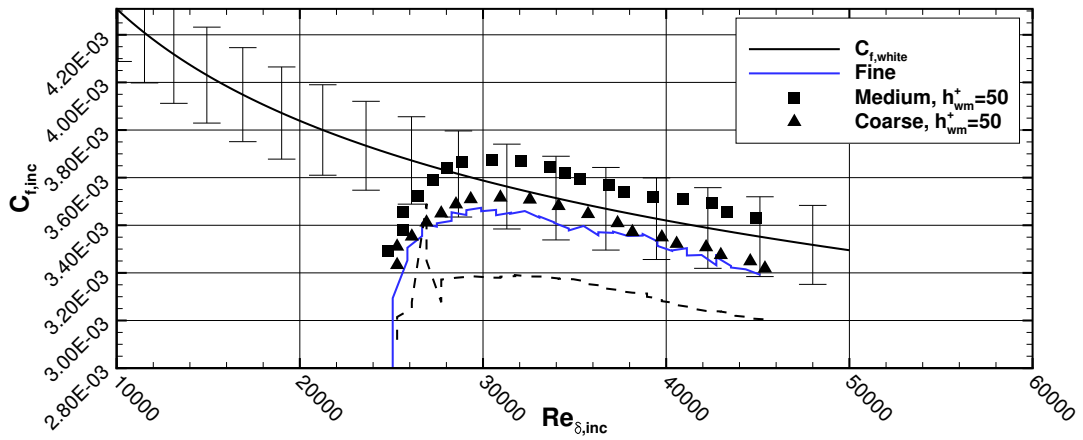

Figure 7.10: Flat plate skin friction coefficient. Symbols denote use of wall model, dashed line is coarse grid without wall model

The wall modeled results on both the coarse and medium meshes agrees very well with the fit by White. While the the wall model results on both meshes are accurate when compared to the fit by White, they do not produce identical results. The reason for this difference can be attributed to multiple possible causes. Possible reasons for the error include:

- Insufficient wall-model convergence. The wall models in the two simulations each executed 10 sub-iterations to solve the wall model equations. Given that the two simulations had drastically different timesteps, the number of sub-iterations per timestep was not constant. Additionally, the finer near-wall mesh in the medium simulation allowed for smaller flow structures to be present. These structures would be characterized by higher frequencies and shorter characteristic times.

- More energetic turbulent inflow. The inflow Reynolds stresses peak near the wall, as shown in Fig. 7.4. The finer near-wall mesh in the medium grid allows for the introduction of resolved fine-scale energetic structures near the wall.

- Performance of the Vreman subgrid stress model. It is unclear at this point what the effect is of near-wall resolution on the subgrid stress stress model used in this study.

7.4.2 Reynolds Stresses

In addition to correctly determining mean values of the flowfield primitives, it is critical that any augmentation to an LES accurately predict the resolved scale Reynolds stresses. These include the normal Reynolds stresses ($\overline{u'u'}$, $\overline{v'v'}$, and $\overline{w'w'}$) and the Reynolds shear stresses ($\overline{u'v'}$, $\overline{u'w'}$, $\overline{v'w'}$). In the case of a wall-bounded flow, analysis is typically restricted to the streamwise and normal Reynolds stress, and the $\overline{u'v'}$ shear.

The Reynolds normal stresses are shown in Fig. 7.11. The profiles collapse for stations greater than $x/\delta = 15$, indicating that the synthetically generated turbulence has equilibrated and that self-similarity has been achieved. Reasonable agreement is observed with the experimental measurements of $\overline{u'u'}$ by Souverein [5]. Agreement is poorer when comparing to the measurement of $\overline{v'v'}$. Similar disagreement was observed by Kawai and Larsson [8] when simulating the $Re_\theta = 50,000$ experiments by Souverein.

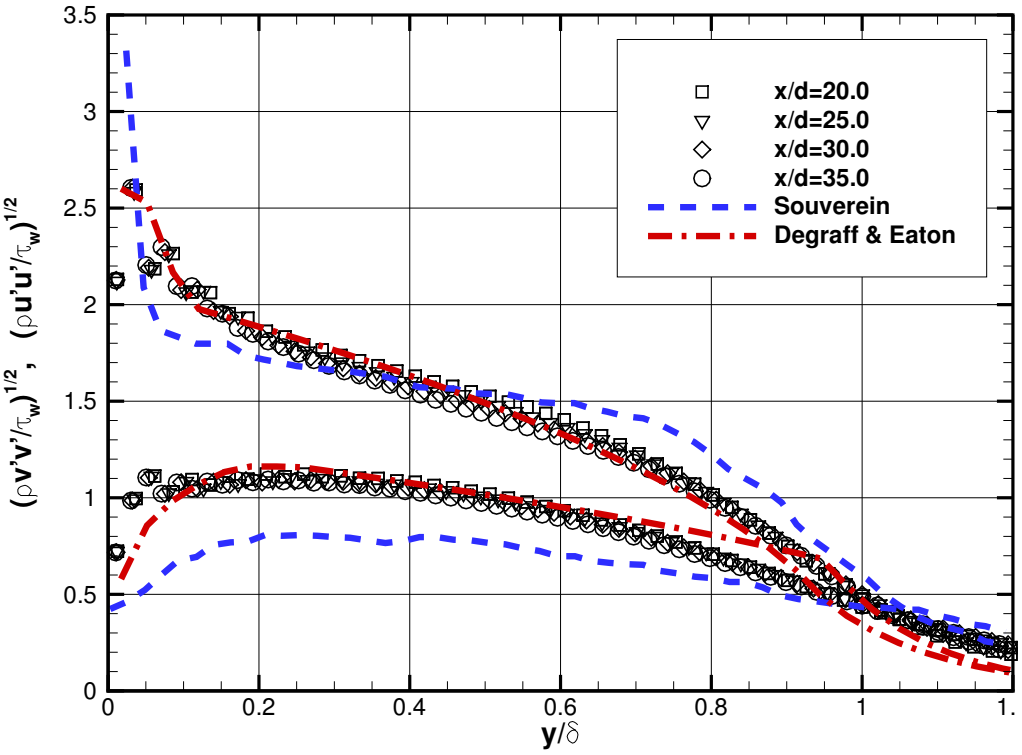

Figure 7.11: Flat plate Reynolds stresses (normal) on Coarse grid, compared to the experiment of Souverein [5] and the incompressible profile of Degraff and Eaton [6]

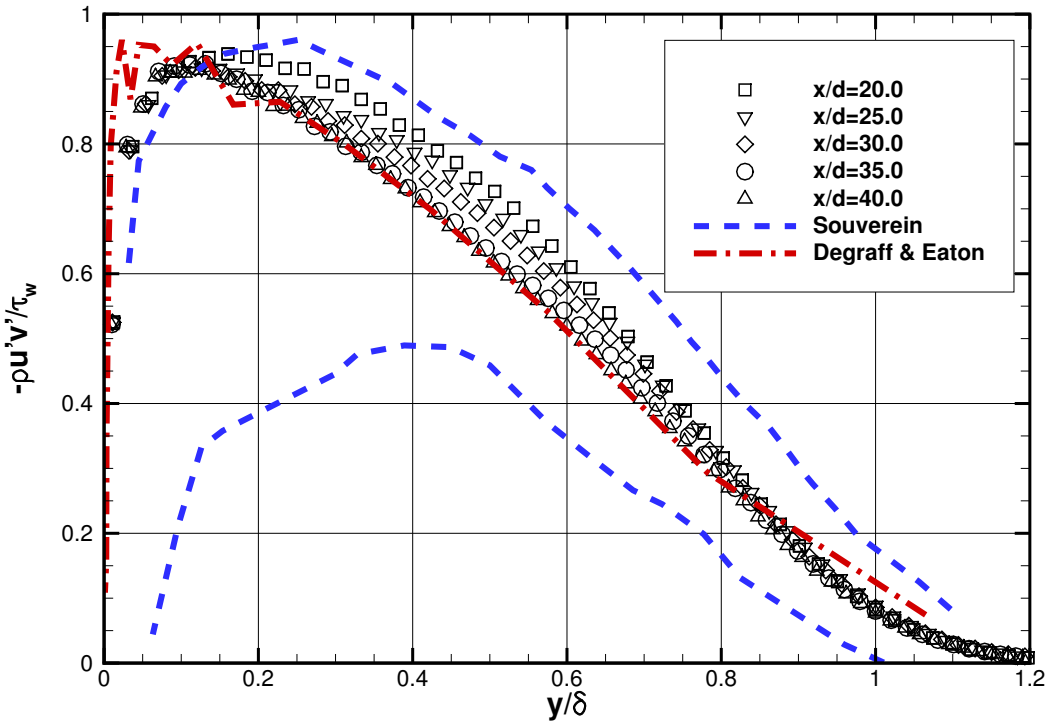

Figure 7.12: Flat plate Reynolds stresses (shear) on Coarse grid

Souverein [45] notes a systemic underrepresentation of v', so our current disagreement is likely attributable to experimental error. There is exceptional agreement between the averaged Reynolds normal stresses and the profile by Degraff and Eaton [6]. This indicates that the computed Reynolds stresses have not been adversely affected by the use of the wall model.

The Reynolds shear stresses are shown in Fig. 7.12. As is seen in the normal stress, the profiles collapse for stations greater than $x/\delta = 15$, however further downstream reductions in Reynolds shear stress is observed. There is a large spread in experimental measurements of Reynolds shear stress reported by Souverein [45] at this Reynolds number. The values predicted in this simulation fall within the experimentally observed envelope, shown in Fig. 7.12. The computed Reynolds shear stress nearly identically reproduces the incompressible profile from Degraff and Eaton [6] at this Re_θ after the

Grid	Timestep (ns)	Number of iterations	Wall time (hrs)
Resolved	14	1,250,000	1.20×10^6
Medium	60	187,500	1.65×10^5
Coarse	250	60,000	4.80×10^4

Table 7.5: Computational cost of flat plate calculations

flow has developed. The agreement with the incompressible profile indicates that the computed stress has not been adversely affected by the use of the wall model.

7.4.3 Computation Time

In any LES, the total number of computational elements is driven by the integral length scale spacing used throughout the domain, and is a very weak function of near-wall clustering. The three grids used in this study all have approximately the same number of computational elements ranging from 40-48 million. The maximum stable timestep varies greatly from grid to grid, and has a significant impact on the cost of the calculations, as shown in Table 7.5. This analysis assumes that time per iteration scales linearly with grid size an that all calculations are executed on 720 computational cores.

The obvious impact of the wall model is that it accelerated the speed of the calculation by allowing for a significantly higher timestep than the wall-resolved calculation without having to resort to point-implicit time-stepping. This means that the wall-resolved calculation requires more than 20 times the computational resources of the coarse wall-modeled calculation at this condition.

7.4.4 Impact of Wall Model Parameters

In this section we examine the sensitivity of the solution to permutations in wall model parameters. Permutations were examined on the Coarse grid to expedite the exploration of a large parameter space. Figs. 7.13 - 7.16 show the previously discussed results at the $x/\delta = 30$ station as well as two additional results. The first additional result involves moving the probe location approximately twice as far from the wall as previously examined. The second additional result executes ten-times as many wall-model sub-iterations as was used in the previous calculations.

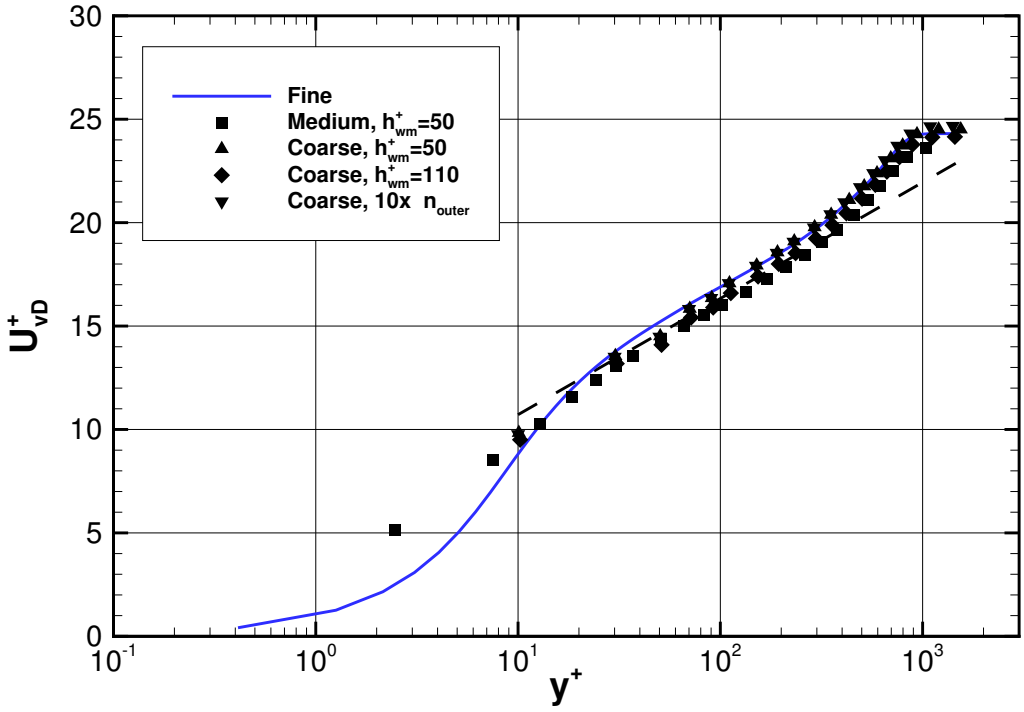

Figure 7.13: Flat plate van Driest-transformed velocity profiles for a variety of wall model settings

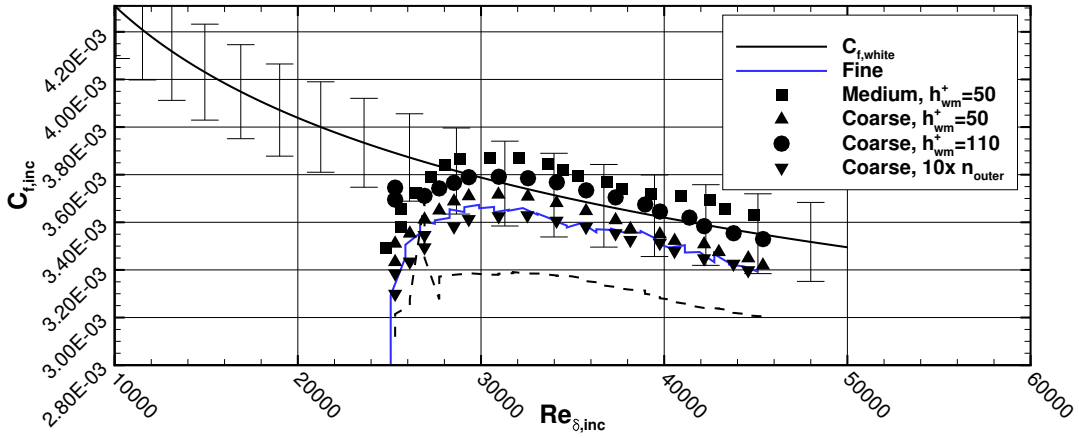

Figure 7.14: Flat plate skin friction coefficient for a variety of wall model settings. Symbols denote use of wall model, dashed line is coarse grid without wall model

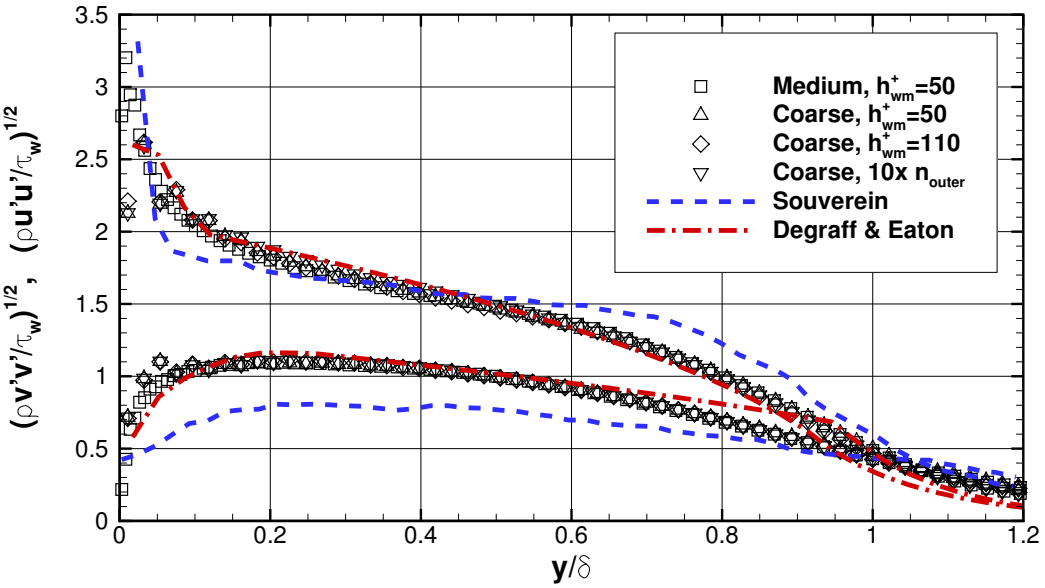

Figure 7.15: Flat plate Reynolds stresses (normal) for a variety of wall model settings compared to the experiment of Souverein [5] and the incompressible profile of Degraff and Eaton [6]

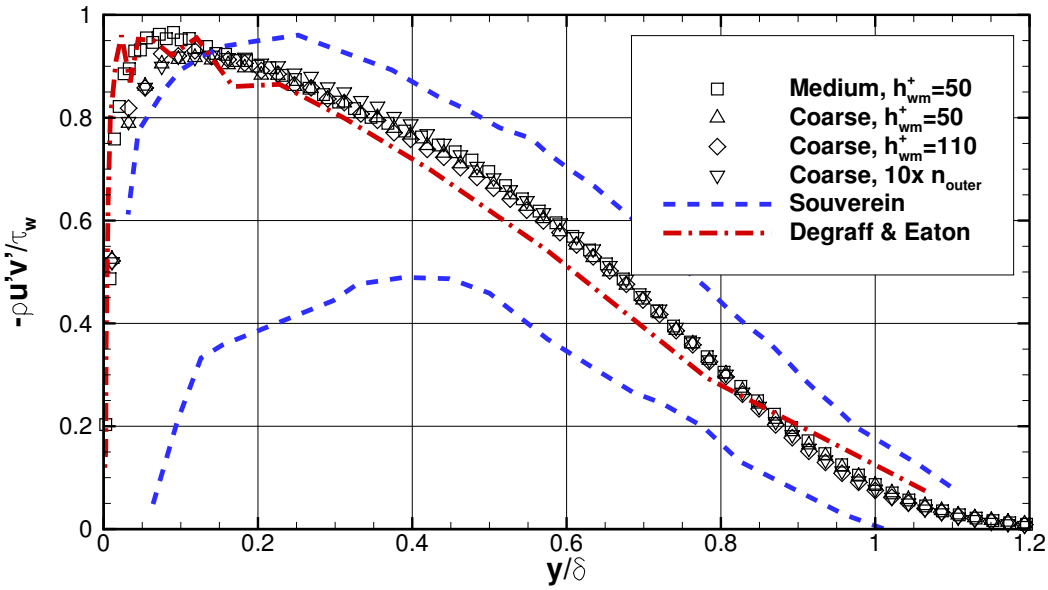

Figure 7.16: Flat plate Reynolds stresses (shear) for a variety of wall model settings

Location of wall model probe

Moving the probe location further from the wall resulted in a slight increase in computed skin friction, and a corresponding shift in the log region of the van Driest-transformed velocity profiles. The Reynolds-normal stresses shown in Fig. 7.15 are insensitive to adjusting the probe location. The Reynolds-shear stress shown in Fig. 7.16 are nearly identical to the results with the probe placed closer to the wall, demonstrating similar insensitivity to probe placement.

Degree of wall model convergence

The results previously discussed in this chapter have involved running 10 sub-iterations of the wall model for each LES RK3 step. We extend the degree of wall model convergence by running 100 wall model sub-iterations and examine the effect on the calculation. The probe location for this calculation was at $h^+_{\text{wm}} = 50$.

The mean skin friction is underpredicted to a greater extent than the other model permutations, as shown in Fig. 7.14. The van Direst-transformed velocity profile is identical to the result using fewer wall model sub-iterations. The mean Reynolds stresses exhibit very slight elevation when compared to the other results, suggesting a slight dependence of the turbulent statistics on the number of wall model sub-iterations, or at least the streamwise extent over which they equilibrate.

7.5 Conclusions

A validation was conducted against the experimental measurements of Souverein [5]. This validation served as an important milestone to demonstrate the accuracy of several key additions to US3D working in concert. Namely:

- Wall model boundary condition operating in an equilibrium boundary layer.
- Digitally filtered turbulent inflow of Karta [38] applied to a wall-bounded flow.
- Vreman [37] subgrid-scale stress model.
- All associated statistics routines.

Wall-modeled calculations agree with the boundary layer properties measured experimentally, predicted by analytic theory, and those produced by wall-resolved simulations. The sensitivity of the solutions to permutations of wall model parameters were examined, and determined to be slight. This suite of models are now prepared host of research problems in high Reynolds number LES.

Chapter 8

Summary and Conclusions

8.1 Summary

A wall-modeled boundary condition was developed and integrated into the US3D finite volume solver. The boundary condition was derived so that it would be appropriate for compressible flows with heat transfer. A set of one-dimensional equations are solved at each wall face for wall tangent velocity and specific energy. Pressure is assumed to be constant in the wall-normal direction and density is prescribed from the equation of state. Solution of these wall model equations allows for the accurate determination of skin friction and wall heat flux on grids that are severely under-resolved at the wall boundary. Since the explicit timestep used in a finite volume calculation is determined by the shortest cell dimension in the entire computational domain, coarsening the near-wall region allows for significantly larger timesteps and dramatically lowers the computational cost to converge statistics of time-accurate simulations.

Non-equilibrium effects such as pressure gradient and convective imbalances are accounted for in the model through a source term. In principle, modeling these effects as a source term allows for many possible closures and degrees of fidelity without changing the solution methodology. For the results presented in the work, the pressure gradient is assumed to be a function of the wall-tangent directions only, and not a function of the wall-normal direction. This allowed for evaluation of the pressure gradient from resolved data in the global solution at the wall model probe location to be enforced all the way to the wall. The convective source term was similarly evaluated from finite

volume data at the probe location, but this term is damped using a van Driest-type damping very close to the wall. This represents a gross approximation that is accurate only on the boundaries, and does not take into account variations in this profile due to compressibility or local discontinuities.

Two different methods of determining an RANS turbulent eddy viscosity were implemented in the model. The first was a mixing-length based model, with cold-wall correction. This type of model is typically used in large eddy simulations to account for mixing at the smallest unresolved scales. The second model implemented was the compressible Spalart-Allmaras turbulence model by Catris and Aupoix. This model adds a fourth equation to the set of one-dimensional line solutions at each wall face, and is a means of incorporating information about the state of the turbulence at the edge of the wall model into its solution.

The model was evaluated against a series of RANS and LES test cases to assess the suitability of the various modeling choices, and the relative contribution of the model terms in both equilibrium and non-equilibrium flows. High Reynolds number cold-wall test cases from the CUBRC LENS facilities were used to assess the performance of the model in RANS calculations of axisymmetric cold-wall bodies. Wall-modeled LES calculations were conducted on a Mach 2.3 flat plate at an Re_θ of 5,000.

8.2 Conclusions

The wall model presented in this work produces accurate boundary layer profiles and surface flux calculations on coarsened grids in a variety of applications. RANS calculations on equilibrium boundary layers were accurate for all combinations of model terms and choice of eddy viscosity formulations so long as the wall model probe location was within the log region of the turbulent boundary layer. For scenarios where the probe fell outside of the log region, wall-modeled results based on the mixing-length eddy viscosity formulation showed significantly greater error than simulations conducted with the SA-Catris model.

For non-equilibrium RANS flows, simulations using mixing length eddy viscosity were inaccurate due to the inaccuracies in the wall-modeled eddy viscosity profile. Simulations using SA-Catris for eddy viscosity produced results qualitatively similar to

wall-resolved calculations of non-equilibrium flows. This general agreement for all permutation of model terms suggests two things. First, the profile used for the convective source terms is inaccurate enough where its inclusion does not significantly improve the solution. Secondly, the inclusion or omission of non-equilibrium effects within the wall-model is not a first-order effect on the quality of the wall-modeled solution for some non-equilibrium flows.

Finally, through our examination of the model's performance in an LES of a compressible boundary layer we demonstrated that the model is suitable for use in wall-modeled LES. Together with the inclusions of a new subgrid-scale stress model into US3D along with a synthetically generated turbulent inflow, a new capability has been added to the research tool to facilitate wall-bounded turbulence research.

8.3 Suggestions for Future Research

Now that the wall model has been integrated into US3D and partially validated, many new avenues of research are available. Two categories of suggestions are presented: research into wall models themselves and research that is facilitated by the use of a wall model.

Research should continue in assessing and improving wall models used in the LES of compressible flows with heat transfer. In particular, attention should be focused on flows of engineering interest, which will necessarily include STBLIs and other non-equilibrium phenomena. To examine the effect of wall-modeled LES on compression flows, WM-LES should be conducted on the compression ramp of Zheltovodov [46], CUBRC Hollow Cylinder-Flare of Holden *et al.* [3] and CUBRC Large Cone-Flare, also of Holden *et al.* To examine the effect of shock impingement, the LES discussed in this work should be extended to include the shock generated in the work by Souverein *et al.* [5] Three-dimensional STBLIs could be examined by flowing a turbulent boundary layer over a vertically mounted fin, as in the experiments by Zheltovodov [47] and Kim [48]. The results of these investigations would further inform the community on the necessity of non-equilibrium wall-modeled terms, and the applicability of this type of wall models to the LES of STBLIs. Assuming these investigations are successful, a dataset should

be identified to allow for the wall model to be evaluated on the internal flowpath of a scramjet inlet.

A second class of research suggestions focuses on research enabled by the use of a wall model. Typically, the wall model could be used to relax restrictive timesteps used in the study of very high Reynolds number configurations. There are current efforts underway to use the model to develop a wall-bound turbulent boundary layer over a splitter plate to be used in the simulation of a high Reynolds number mixing layer.

References

[1] Haecheon Choi and Parviz Moin. Grid-point requirements for large eddy simulation: Chapman's estimates revisited. *Physics of Fluids (1994-present)*, 24(1), 2012.

[2] Steven R Allmaras, Forrester T Johnson, and Philippe R Spalart. Modifications and clarifications for the implementation of the spalart-allmaras turbulence model. In *Seventh International Conference on Computational Fluid Dynamics (ICCFD7)*, pages 1–11, 2012.

[3] Michael S Holden, Timothy P Wadhams, and Matthew MacLean. Shock wave/turbulent boundary layer (SWTBL) study presented at AIAA Aviation 2014. `http://www.cubrc.org/index.php?option=com_content&view=article&id=121&Itemid=64`.

[4] Sergio Pirozzoli and Matteo Bernardini. Supersonic turbulent boundary layers - DNS database up to $Re_\tau = 1110$. `http://reynolds.dma.uniroma1.it/dnsm2/`.

[5] Louis J Souverein, Pierre Dupont, Jean-François Debiève, Bas W Van Oudheusden, and Fulvio Scarano. Effect of interaction strength on unsteadiness in shock-wave-induced separations. *AIAA journal*, 48(7):1480–1493, 2010.

[6] David B. De Graff and John K. Eaton. Reynolds-number scaling of the flat-plate turbulent boundary layer. *Journal of Fluid Mechanics*, 422:319–346, 11 2000.

[7] Dean R Chapman. Computational aerodynamics development and outlook. *AIAA journal*, 17(12):1293–1313, 1979.

[8] Soshi Kawai and Johan Larsson. Wall-modeling in large eddy simulation: Length scales, grid resolution, and accuracy. *Physics of Fluids (1994-present)*, 24(1):015105, 2012.

[9] David M Dawson, Julien Bodart, and Sanjiva K Lele. Assessment of wall-modeled large eddy simulation for supersonic compression ramp flows. AIAA/ASME/SAE/ASEE Joint Propulsion Conference, 2013.

[10] Robert H Nichols and CC Nelson. Wall function boundary conditions including heat transfer and compressibility. *AIAA journal*, 42(6):1107–1114, 2004.

[11] Zachary P. Vane and Sanjiva K. Lele. Simulations of a normal shock train in a constant area duct using wall-modeled les. In *43rd Fluid Dynamics Conference*. American Institute of Aeronautics and Astronautics, 2013.

[12] DB Spalding. A single formula for the "law of the wall". *Journal of Applied Mechanics*, 28(3):455–458, 1961.

[13] Stephen B Pope. *Turbulent flows*. Cambridge University Press, 2000.

[14] David C Wilcox. *Turbulence modeling for CFD*, volume 2. DCW industries La Canada, CA, 1998.

[15] Donald Coles. The law of the wake in the turbulent boundary layer. *Journal of Fluid Mechanics*, 1:191–226, 7 1956.

[16] Ugo Piomelli and Elias Balaras. Wall-layer models for large-eddy simulations. *Annual review of fluid mechanics*, 34(1):349–374, 2002.

[17] PR Spalart, WH Jou, M Strelets, SR Allmaras, et al. Comments on the feasibility of LES for wings, and on a hybrid RANS/LES approach. *Advances in DNS/LES*, 1:4–8, 1997.

[18] Ryan B Bond and Frederick G Blottner. A compressible wall-layer approach compatible with various turbulence models. *AIAA Paper*, 1410, 2007.

[19] Ryan B Bond, Frederick G Blottner, and Thomas M Smith. Validation of a wall-layer model for a shock-wave/boundary-layer interaction. *AIAA Paper*, 115, 2010.

[20] RB Bond and Frederick G Blottner. Derivation, implementation, and initial testing of a compressible wall-layer model. *International Journal for Numerical Methods in Fluids*, 66(9):1183–1206, 2011.

[21] S Hickel, E Touber, J Bodart, and J Larsson. A parametrized non-equilibrium wall-model for large-eddy simulations. In *Proceedings of the Summer Program*, page 127. Center for Turbulence Research, Stanford University, 2012.

[22] George Ilhwan Park and Parviz Moin. Numerical aspects and implementation of a two-layer zonal wall model for LES of compressible turbulent flows on unstructured meshes. *Journal of Computational Physics*, 305:589 – 603, 2016.

[23] George Ilhwan Park and Parviz Moin. An improved dynamic non-equilibrium wall-model for large eddy simulation. *Physics of Fluids*, 26(1), 2014.

[24] Ioannis Nompelis, Travis Drayna, and Graham Candler. A parallel unstructured implicit solver for hypersonic reacting flow simulation. In *17th AIAA Computational Fluid Dynamics Conference*, 2005.

[25] S. R. Spalart and S. A. Allmaras. A one-equation turbulence model for aerodynamic flows. In *AIAA Paper No. 92-0429*, 1992.

[26] Langley research center langley research center turbulence modeling resource, http://turbmodels.larc.nasa.gov/, May 2015.

[27] M. J. Wright, G. V. Candler, and D. Bose. Data-parallel line-relaxation method for the navier-stokes equations. *AIAA Journal*, 36(9):1603–1609, September 1998.

[28] Graham V. Candler, Pramod K. Subbareddy, and Ioannis Nompelis. CFD methods for hypersonic flows and aerothermodynamics. In *Hypersonic Nonequilibrium Flows: Fundamentals and Recent Advances*, pages 203–237. American Institute of Aeronautics and Astronautics, Inc., 2015.

[29] Soshi Kawai and Johan Larsson. A non-equilibrium wall-model for LES of shock/boundary layer interaction at high reynolds number. In *42nd AIAA Fluid Dynamics Conference and Exhibit*. American Institute of Aeronautics and Astronautics, 2012.

[30] Zachary P. Vane, Ivan Bermejo-Moreno, and Sanjiva K. Lele. Wall-modeled large-eddy simulations of a supersonic turbulent flow in a square duct. In *44th AIAA Fluid Dynamics Conference*. American Institute of Aeronautics and Astronautics, 2014.

[31] Stéphane Catris and Bertrand Aupoix. Density corrections for turbulence models. *Aerospace Science and Technology*, 4(1):1 – 11, 2000.

[32] G. N. Coleman, A. Garbaruk, and P. R. Spalart. Direct numerical simulation, theories and modelling of wall turbulence with a range of pressure gradients. *Flow, Turbulence and Combustion*, 95(2):261–276, 2015.

[33] Iván Bermejo-Moreno, Laura Campo, Johan Larsson, Julien Bodart, David Helmer, and John K. Eaton. Confinement effects in shock wave/turbulent boundary layer interactions through wall-modelled large-eddy simulations. *Journal of Fluid Mechanics*, 758:5–62, 11 2014.

[34] Johan Larsson, Soshi Kawai, Julien Bodart, and Ivan Bermejo-Moreno. Large eddy simulation with modeled wall-stress: recent progress and future directions. *Mechanical Engineering Reviews*, (0), 2015.

[35] Pramod K. Subbareddy and Graham V. Candler. A fully discrete, kinetic energy consistent finite-volume scheme for compressible flows. *Journal of Computational Physics*, 228(5):1347 – 1364, 2009.

[36] F Ducros, V Ferrand, F Nicoud, C Weber, D Darracq, C Gacherieu, and T Poinsot. Large-eddy simulation of the shock/turbulence interaction. *Journal of Computational Physics*, 152(2):517 – 549, 1999.

[37] A. W. Vreman. An eddy-viscosity subgrid-scale model for turbulent shear flow: Algebraic theory and applications. *Physics of Fluids*, 16(10):3670–3681, 2004.

[38] Anand Kartha, Pramod K. Subbareddy, Graham V. Candler, and Paul Dimotakis. Les of reacting mixing layers: Species concentration boundedness and inflow conditions. In *22nd AIAA Computational Fluid Dynamics Conference*. American Institute of Aeronautics and Astronautics, 2015.

[39] Xiaohua Wu. Inflow turbulence generation methods. *Annual Review of Fluid Mechanics*, (0), 2017.

[40] Nitin S Dhamankar, Gregory A Blaisdell, and Anastasios S Lyrintzis. An overview of turbulent inflow boundary conditions for large eddy simulations. In *22nd AIAA Computational Fluid Dynamics Conference*, page 3213, 2015.

[41] Alexander J Smits and Jean-Paul Dussauge. *Turbulent shear layers in supersonic flow, second edition*. New York : Springer, New York, 2006.

[42] Julian CR Hunt, Alan A Wray, and Parviz Moin. Eddies, streams, and convergence zones in turbulent flows. 1988.

[43] Frank M White and Isla Corfield. *Viscous fluid flow*, volume 3. McGraw-Hill New York, 2006.

[44] S. Pirozzoli, F. Grasso, and T. B. Gatski. Direct numerical simulation and analysis of a spatially evolving supersonic turbulent boundary layer at m=2.25. *Physics of Fluids*, 16(3):530–545, 2004.

[45] Louis J Souverein. *On the scaling and unsteadiness of shock induced separation*. PhD thesis, Delft University of Technology, 2010.

[46] AA Zheltovodov, VM Trofimov, E Schülein, and VN Yakovlev. An experimental documentation of supersonic turbulent flows in the vicinity of forward-and backward-facing ramps. *Report N*, 2030, 1990.

[47] AA Zheltovodov. Regimes and properties of three-dimensional separation flows initiated by skewed compression shocks. *Journal of Applied Mechanics and Technical Physics*, 23(3):413–418, 1982.

[48] K-S Kim, Y Lee, FS Alvi, GS Settles, and C Horstman. Skin-friction measurements and computational comparison of swept shock/boundary-layer interactions. *AIAA journal*, 29(10):1643–1650, 1991.

Appendix A

Derivations

A.1 Wall Model Equation

As stated in Chapter 3, the Navier-Stokes equations in divergence form are:

$$\frac{\partial U}{\partial t} + \frac{\partial F_1}{\partial x_1} + \frac{\partial F_2}{\partial x_2} + \frac{\partial F_3}{\partial x_3} = 0 \tag{A.1}$$

where U and F_j are the vectors of conserved variables and fluxes respectively.

$$U = \begin{pmatrix} \rho \\ \rho u_1 \\ \rho u_2 \\ \rho u_3 \\ E \end{pmatrix}, \quad F_j = \begin{pmatrix} \rho u_j \\ \rho u_1 u_j + p\delta_{1j} - \sigma_{1j} \\ \rho u_2 u_j + p\delta_{2j} - \sigma_{2j} \\ \rho u_3 u_j + p\delta_{3j} - \sigma_{3j} \\ (E+p)u_j - \sigma_{kj}u_k - q_j \end{pmatrix} \tag{A.2}$$

The viscous stress tensor, σ_{ij}, and heat conduction vector, q_j, are defined as

$$\sigma_{ij} = \hat{\mu}\left(\frac{\partial u_i}{\partial x_j} + \frac{\partial u_j}{\partial x_i}\right) - \frac{2}{3}\hat{\mu}\frac{\partial u_k}{\partial x_k}\delta_{ij} \tag{A.3}$$

$$q_j = \hat{\kappa}\frac{\partial T}{\partial x_j} \tag{A.4}$$

Here, the Bouusinesq approximation has been used to treat the mean effects of turbulent motion as an approximate eddy viscosity

$$\hat{\mu} = \mu + \mu_t, \qquad \hat{\kappa} = \kappa + \kappa_t \tag{A.5}$$

We start by assuming that pressure is constant in the wall normal direction, and as a result density is uniquely determined by temperature. Using the equation of state for a perfect gas:

$$\rho = \frac{P\big|_{h_{wm}^+}}{RT} \tag{A.6}$$

With this relationship, conservation of mass has been decoupled from the equation set, and is no longer required. Density is a consequence of the temperature field and the pressure at the probe location.

Assuming gradients in the wall-normal direction are much larger than gradients in the wall-tangent directions, we rearrange the conservation equations to retain only the time and x_3 derivatives on the left hand side.

$$\begin{aligned}
\frac{\partial \rho u}{\partial t} + \frac{\partial}{\partial x_3}\left[\rho u w - \hat{\mu}\frac{\partial u}{\partial x_3}\right] &= -\sum_{i=1}^{2}\frac{\partial F_i}{\partial x_i} \\
\frac{\partial \rho v}{\partial t} + \frac{\partial}{\partial x_3}\left[\rho v w - \hat{\mu}\frac{\partial v}{\partial x_3}\right] &= -\sum_{i=1}^{2}\frac{\partial F_i}{\partial x_i} \\
\frac{\partial \rho w}{\partial t} + \frac{\partial}{\partial x_3}\left[\rho w^2 - \frac{4}{3}\hat{\mu}\frac{\partial w}{\partial x_3}\right] &= -\sum_{i=1}^{2}\frac{\partial F_i}{\partial x_i} \\
\frac{\partial \rho e}{\partial t} + \frac{\partial}{\partial x_3}\left[(\rho e + P)w - \hat{\mu}\left(u\frac{\partial u}{\partial x_3} + v\frac{\partial v}{\partial x_3} + w\frac{\partial w}{\partial x_3}\right) - \hat{\kappa}\frac{\partial T}{\partial x_3}\right] &= -\sum_{i=1}^{2}\frac{\partial F_i}{\partial x_i}
\end{aligned} \tag{A.7}$$

The right-hand side source terms in Eqs. A.7 are typically neglected in their entirety for wall wall models. They will be carried forward in this derivation with the short hand notation of Σ.

The subsequent derivation will examine the u-momentum equation only, however the extension to v-momentum is trivial. Expanding Eqs. A.7 by chain rule and neglecting the time derivative of density:

$$\rho\frac{\partial u}{\partial t}+\rho\left(u\frac{\partial w}{\partial x_3}+w\frac{\partial u}{\partial x_3}\right)+uw\frac{\partial \rho}{\partial x_3}-\frac{\partial}{\partial x_3}\left(\hat{\mu}\frac{\partial u}{\partial x_3}\right)=-\Sigma \tag{A.8}$$

Dividing by density:

$$\frac{\partial u}{\partial t}+u\frac{\partial w}{\partial x_3}+w\frac{\partial u}{\partial x_3}+\frac{uw}{\rho}\frac{\partial \rho}{\partial x_3}-\frac{1}{\rho}\frac{\partial}{\partial x_3}\left(\hat{\mu}\frac{\partial u}{\partial x_3}\right)=-\frac{1}{\rho}\Sigma \tag{A.9}$$

If we assume the distance the gradient is evaluated over, δ, to be small, u to be large and represent it as Ψ, and w to be small represented as ψ. The resulting magnitude analysis yields:

$$\frac{\Psi}{\Delta t}+\underbrace{\Psi\frac{\psi}{\delta}+\psi\frac{\Psi}{\delta}+\frac{\Psi\psi}{\rho}\frac{\rho}{\delta}}_{small}-\underbrace{\frac{\hat{\mu}}{\rho}\frac{\Psi}{\delta^2}}_{large}=-\frac{1}{\rho}\Sigma \tag{A.10}$$

We now assume that the terms that scale as $\Psi\psi/\delta$ are small compared to the other terms. Therefore, Eq. A.9 reduces to:

$$\frac{\partial u}{\partial t}-\frac{1}{\rho}\frac{\partial}{\partial x_3}\left(\hat{\mu}\frac{\partial u}{\partial x_3}\right)=-\frac{1}{\rho}\Sigma \tag{A.11}$$

The source term is fixed in time with regards to the wall model, and is evaluated from LES data from time level n. The current wall model sub-iteration is denoted as iteration k, and the previous sub-iteration $k-1$. Using these labels, Eq. A.11 becomes

$$\frac{\partial u^k}{\partial t}-\frac{1}{\rho^{k-1}}\frac{\partial}{\partial x_3}\left(\hat{\mu}^{k-1}\frac{\partial u^k}{\partial x_3}\right)=-\left.\frac{1}{\rho}\Sigma\right|^n \tag{A.12}$$

Defining u^k as the sum of u^{k-1} and δu^k and reordering terms we arrive at:

$$\begin{aligned}\frac{\delta u^k}{\delta t}-\frac{1}{\rho^{k-1}}\frac{\partial}{\partial x_3}\left[\hat{\mu}^{k-1}\frac{\partial}{\partial x_3}\left(u^{k-1}+\delta u^k\right)\right]&=-\left.\frac{1}{\rho}\Sigma\right|^n\\ \frac{1}{\Delta t}\delta u^k-\frac{1}{\rho^{k-1}}\frac{\partial}{\partial x_3}\left[\hat{\mu}^{k-1}\frac{\partial}{\partial x_3}\delta u^k\right]&=\frac{1}{\rho^{k-1}}\frac{\partial}{\partial x_3}\left[\hat{\mu}^{k-1}\frac{\partial}{\partial x_3}u^{k-1}\right]-\left.\frac{1}{\rho}\Sigma\right|^n\end{aligned} \tag{A.13}$$

As stated previously, the extension of Eq. A.13 to v velocity is trivial. The source term on the right hand side of Eq. A.13 can neglected or modeled depending on however one chooses. The update δu^k consists of a tri-diagonal implicit operator and an explicit evaluation. The implicit operator is built using central differences. Considering point i within the wall model, we define:

$$\begin{aligned}
\hat{\mu}^+ &= \hat{\mu}\left(T\Big|_{i+1/2} \right) \\
\hat{\mu}^- &= \hat{\mu}\left(T\Big|_{i-1/2} \right) \\
\Delta x^+ &= x_{i+1} - x_i \\
\Delta x^- &= x_i - x_{i-1} \\
\Delta x_f &= \frac{1}{2}(x_{i+1} + x_i) - \frac{1}{2}(x_i + x_{i-1})
\end{aligned} \tag{A.14}$$

We now build the implicit operator by using central differences

$$\begin{aligned}
&\frac{1}{\Delta t}\delta u_i^k - \frac{1}{\rho^{k-1}}\frac{\partial}{\partial x_3}\left[\hat{\mu}^{k-1}\frac{\partial}{\partial x_3}\delta u^k\right] = \frac{1}{\Delta t}\delta u_i^k - \frac{1}{\rho^{k-1}}\frac{\Delta}{\Delta x_f}\left[\hat{\mu}^{k-1}\frac{\partial}{\partial x_3}\delta u^k\right] \\
&= \frac{1}{\Delta t}\delta u_i^k - \frac{1}{\rho^{k-1}}\frac{1}{\Delta x_f}\left[\hat{\mu}^{+}\frac{1}{\Delta x^+}\left(\delta u_{i+1}^k - \delta u_i^k\right) - \hat{\mu}^{-}\frac{1}{\Delta x^-}\left(\delta u_i^k - \delta u_{i-1}^k\right)\right] \\
&= \frac{1}{\Delta t}\delta u_i^k - \frac{1}{\rho^{k-1}}\frac{1}{\Delta x_f}\left[\frac{\hat{\mu}^{+}}{\Delta x^+}\delta u_{i+1}^k - \left(\frac{\hat{\mu}^{+}}{\Delta x^+} + \frac{\hat{\mu}^{-}}{\Delta x^-}\right)\delta u_i^k + \frac{\hat{\mu}^{-}}{\Delta x^-}\delta u_{i-1}^k\right]
\end{aligned} \tag{A.15}$$

Returning our attention to the energy equation component of A.7, we again expand by chain rule and neglect products of w.

$$\frac{\partial e}{\partial t} + \frac{1}{\rho}\frac{\partial}{\partial x_3}\left[\hat{\mu}\left(-u\frac{\partial u}{\partial x_3} - v\frac{\partial v}{\partial x_3}\right) - \hat{\kappa}\frac{\partial T}{\partial x_3}\right] = -\frac{1}{\rho}\Sigma \tag{A.16}$$

For this equation, we choose to evaluate the velocities at the previous wall model sub-iteration and linearize specific energy and temperature.

$$\frac{\delta e^k}{\Delta t} + \frac{1}{\rho^{k-1}}\frac{\partial}{\partial x_3}\left[\hat{\mu}^{k-1}\left(-u^{k-1}\frac{\partial u^{k-1}}{\partial x_3} - v^{k-1}\frac{\partial v^{k-1}}{\partial x_3}\right) - \hat{\kappa}^{k-1}\left(\frac{\partial T^{k-1}}{\partial x_3} + \frac{\partial \delta T^k}{\partial x_3}\right)\right] = -\frac{1}{\rho}\Sigma\Big|^n \quad \text{(A.17)}$$

Neglecting enthalpy of formation, the specific energy of the gas is defined as $e = c_v T + \frac{1}{2}u_i u_i$. Holding kinetic energy constant, the change in temperature is related to the change in internal energy by $\delta T = \delta e / c_v$. Rearranging Eq. A.17 and expressing updates in terms of δe:

$$\frac{1}{\Delta t}\delta e^k - \frac{1}{\rho^{k-1}}\frac{\partial}{\partial x_3}\left(\frac{\hat{\kappa}^{k-1}}{c_v}\frac{\partial}{\partial x_3}\delta e^k\right) = -\frac{1}{\rho^{k-1}}\left[\frac{\partial}{\partial x_3}\left(-u\hat{\mu}\frac{\partial u}{\partial x_3} - v\hat{\mu}\frac{\partial v}{\partial x_3} - \hat{\kappa}\frac{\partial T}{\partial x_3}\right)\Big|^{k-1} + \Sigma^n\right] \quad \text{(A.18)}$$

The implicit operator for specific energy is formulated identically as was done in Eq. A.15.

$$\frac{1}{\Delta t}\delta e_i^k - \frac{1}{\rho^{k-1}}\frac{\partial}{\partial x_3}\left[\frac{\hat{\kappa}^{k-1}}{c_v}\frac{\partial}{\partial x_3}\delta e^k\right] = \frac{1}{\Delta t}\delta e_i^k - \frac{1}{\rho^{k-1}}\frac{1}{\Delta x_f}\frac{1}{c_v}\left[\frac{\hat{\kappa}^+}{\Delta x^+}\delta e_{i+1}^k - \left(\frac{\hat{\kappa}^+}{\Delta x^+} + \frac{\hat{\kappa}^-}{\Delta x^-}\right)\delta e_i^k + \frac{\hat{\kappa}^-}{\Delta x^-}\delta e_{i-1}^k\right] \quad \text{(A.19)}$$

A.2 Wall-Modeled Spalart-Allmaras (Catris-Aupoix) Equation

The SA-Catris turbulence model is expressed as:

$$\frac{\partial \rho\tilde{\nu}}{\partial t} + u_j\frac{\partial \rho\tilde{\nu}}{\partial x_j} = c_{b1}\tilde{S}\rho\tilde{\nu} - c_{w1}f_w\rho\left(\frac{\tilde{\nu}}{d}\right)^2 + \frac{1}{\sigma}\frac{\partial}{\partial x_j}\left(\mu\frac{\partial\tilde{\nu}}{\partial x_j}\right) + \frac{1}{\sigma}\frac{\partial}{\partial x_j}\left(\sqrt{\rho}\tilde{\nu}\frac{\partial\sqrt{\rho}\tilde{\nu}}{\partial x_j}\right) + \frac{c_{b2}}{\sigma}\frac{\partial\sqrt{\rho}\tilde{\nu}}{\partial x_i}\frac{\partial\sqrt{\rho}\tilde{\nu}}{\partial x_i} \quad \text{(A.20)}$$

with all model constant taken from the standard expression of the model. We assume that gradients in the 1 and 2 directions are very small compared to gradients in the wall-normal direction. We further assume that wall-normal velocity is negligible, and that there is no time derivative of density. Under theses assumptions, the above equation reduces to:

$$\rho\frac{\partial\tilde{\nu}}{\partial t} = \underbrace{c_{b1}\tilde{S}\rho\tilde{\nu} - c_{w1}f_w\rho\left(\frac{\tilde{\nu}}{d}\right)^2}_{\text{I}} + \underbrace{\frac{1}{\sigma}\frac{\partial}{\partial x_3}\left(\mu\frac{\partial\tilde{\nu}}{\partial x_3}\right)}_{\text{II}} + \underbrace{\frac{1}{\sigma}\frac{\partial}{\partial x_3}\left(\sqrt{\rho}\tilde{\nu}\frac{\partial\sqrt{\rho}\tilde{\nu}}{\partial x_3}\right)}_{\text{III}} + \underbrace{\frac{c_{b2}}{\sigma}\frac{\partial\sqrt{\rho}\tilde{\nu}}{\partial x_3}\frac{\partial\sqrt{\rho}\tilde{\nu}}{\partial x_3}}_{\text{IV}} \quad \text{(A.21)}$$

Terms I and II require no further simplification under these assumptions. For term III:

$$\begin{aligned}\frac{1}{\sigma}\frac{\partial}{\partial x_3}\left(\sqrt{\rho}\tilde{\nu}\frac{\partial\sqrt{\rho}\tilde{\nu}}{\partial x_3}\right) &= \frac{1}{\sigma}\frac{\partial}{\partial x_3}\left[\sqrt{\rho}\tilde{\nu}\left(\tilde{\nu}\frac{\partial\sqrt{\rho}}{\partial x_3} + \sqrt{\rho}\frac{\partial\tilde{\nu}}{\partial x_3}\right)\right] \\ &= \frac{1}{\sigma}\frac{\partial}{\partial x_3}\left(\sqrt{\rho}\tilde{\nu}^2\frac{\partial\sqrt{\rho}}{\partial x_3} + \rho\tilde{\nu}\frac{\partial\tilde{\nu}}{\partial x_3}\right) \quad \text{(A.22)}\end{aligned}$$

Term IV expands to:

$$\begin{aligned}\frac{c_{b2}}{\sigma}\frac{\partial\sqrt{\rho}\tilde{\nu}}{\partial x_3}\frac{\partial\sqrt{\rho}\tilde{\nu}}{\partial x_3} &= \frac{c_{b2}}{\sigma}\left(\sqrt{\rho}\frac{\partial\tilde{\nu}}{\partial x_3} + \tilde{\nu}\frac{\partial\sqrt{\rho}}{\partial x_3}\right)\left(\sqrt{\rho}\frac{\partial\tilde{\nu}}{\partial x_3} + \tilde{\nu}\frac{\partial\sqrt{\rho}}{\partial x_3}\right) \\ &= \frac{c_{b2}}{\sigma}\left(\rho\frac{\partial\tilde{\nu}}{\partial x_3}\frac{\partial\tilde{\nu}}{\partial x_3} + \tilde{\nu}^2\frac{\partial\sqrt{\rho}}{\partial x_3}\frac{\partial\sqrt{\rho}}{\partial x_3} + 2\sqrt{\rho}\tilde{\nu}\frac{\partial\sqrt{\rho}}{\partial x_3}\frac{\partial\tilde{\nu}}{\partial x_3}\right) \quad \text{(A.23)}\end{aligned}$$

The solution variable $\tilde{\nu}$ is approximated as the value from the previous iteration, $\tilde{\nu}^{k-1}$ plus an update, $\delta\tilde{\nu}^k$ ($\tilde{\nu} = \tilde{\nu}^{k-1} + \delta\tilde{\nu}^k$). This substitution is now made into the equation, and superscripts are dropped. In the following linearization, the products of two small quantities ($\delta\tilde{\nu}^2$) are neglected. Dividing through by density, the terms of Eq. A.21 become:

Left-Hand Side:

$$\frac{\delta\tilde{\nu}}{\Delta t} \tag{A.24}$$

Term I:

$$\begin{aligned} c_{b1}\tilde{S}(\tilde{\nu}+\delta\tilde{\nu}) - c_{w1}f_w\left(\frac{\tilde{\nu}+\delta\tilde{\nu}}{d}\right)^2 &= c_{b1}\tilde{S}\tilde{\nu} + c_{b1}\tilde{S}\delta\tilde{\nu} - \frac{c_{w1}f_w}{d^2}\big(\tilde{\nu}^2 + 2\tilde{\nu}\delta\tilde{\nu} + 0\big) \\ &= \left[c_{b1}\tilde{S}\tilde{\nu} - c_{w1}f_w\left(\frac{\tilde{\nu}}{d}\right)^2\right] + \left(c_{b1}\tilde{S} - \frac{c_{w1}f_w}{d^2}\tilde{\nu}\right)\delta\tilde{\nu} \end{aligned} \tag{A.25}$$

Term II:

$$\frac{1}{\sigma\rho}\frac{\partial}{\partial x_3}\left[\mu\frac{\partial}{\partial x_3}(\tilde{\nu}+\delta\tilde{\nu})\right] = \frac{1}{\sigma\rho}\left[\frac{\partial}{\partial x_3}\left(\mu\frac{\partial\tilde{\nu}}{\partial x_3}\right) + \frac{\partial}{\partial x_3}\left(\mu\frac{\partial\delta\tilde{\nu}}{\partial x_3}\right)\right] \tag{A.26}$$

Term III:

$$\begin{aligned} &\frac{1}{\rho\sigma}\frac{\partial}{\partial x_3}\left(\sqrt{\rho}(\tilde{\nu}+\delta\tilde{\nu})^2\frac{\partial\sqrt{\rho}}{\partial x_3} + \rho(\tilde{\nu}+\delta\tilde{\nu})\frac{\partial}{\partial x_3}(\tilde{\nu}+\delta\tilde{\nu})\right) \\ &= \frac{1}{\rho\sigma}\frac{\partial}{\partial x_3}\left[\sqrt{\rho}\big(\tilde{\nu}^2 + 2\tilde{\nu}\delta\tilde{\nu} + 0\big)\frac{\partial\sqrt{\rho}}{\partial x_3} + \rho(\tilde{\nu}+\delta\tilde{\nu})\left(\frac{\partial\tilde{\nu}}{\partial x_3} + \frac{\partial\delta\tilde{\nu}}{\partial x_3}\right)\right] \\ &= \frac{1}{\rho\sigma}\frac{\partial}{\partial x_3}\left[\sqrt{\rho}\tilde{\nu}^2\frac{\partial\sqrt{\rho}}{\partial x_3} + 2\sqrt{\rho}\tilde{\nu}\delta\tilde{\nu}\frac{\partial\sqrt{\rho}}{\partial x_3} + \rho\tilde{\nu}\frac{\partial\tilde{\nu}}{\partial x_3} + \rho\tilde{\nu}\frac{\partial\delta\tilde{\nu}}{\partial x_3} + \rho\delta\tilde{\nu}\frac{\partial\tilde{\nu}}{\partial x_3}\right] \\ &= \frac{1}{\rho\sigma}\frac{\partial}{\partial x_3}\left[\left(\sqrt{\rho}\tilde{\nu}^2\frac{\partial\sqrt{\rho}}{\partial x_3} + \rho\tilde{\nu}\frac{\partial\tilde{\nu}}{\partial x_3}\right) + \left(2\sqrt{\rho}\tilde{\nu}\frac{\partial\sqrt{\rho}}{\partial x_3} + \rho\frac{\partial\tilde{\nu}}{\partial x_3}\right)\delta\tilde{\nu} + \rho\tilde{\nu}\frac{\partial\delta\tilde{\nu}}{\partial x_3}\right] \end{aligned} \tag{A.27}$$

Term IV:

$$\begin{aligned}
&\frac{c_{b2}}{\rho\sigma}\left[\rho\frac{\partial}{\partial x_3}(\tilde{\nu}+\delta\tilde{\nu})\frac{\partial}{\partial x_3}(\tilde{\nu}+\delta\tilde{\nu})+(\tilde{\nu}+\delta\tilde{\nu})^2\frac{\partial\sqrt{\rho}}{\partial x_3}\frac{\partial\sqrt{\rho}}{\partial x_3}+2\sqrt{\rho}(\tilde{\nu}+\delta\tilde{\nu})\frac{\partial\sqrt{\rho}}{\partial x_3}\frac{\partial}{\partial x_3}(\tilde{\nu}+\delta\tilde{\nu})\right]\\
&=\frac{c_{b2}}{\rho\sigma}\left[\rho\left(\frac{\partial\tilde{\nu}}{\partial x_3}\frac{\partial\tilde{\nu}}{\partial x_3}+2\tilde{\nu}\frac{\partial\tilde{\nu}}{\partial x_3}\right)+(\tilde{\nu}^2+2\tilde{\nu}\delta\tilde{\nu})\frac{\partial\sqrt{\rho}}{\partial x_3}\frac{\partial\sqrt{\rho}}{\partial x_3}\right.\\
&\qquad\left.+2\sqrt{\rho}\frac{\partial\sqrt{\rho}}{\partial x_3}\left(\tilde{\nu}\frac{\partial\tilde{\nu}}{\partial x_3}+\tilde{\nu}\frac{\partial\delta\tilde{\nu}}{\partial x_3}+\delta\tilde{\nu}\frac{\partial\tilde{\nu}}{\partial x_3}\right)\right]\\
&=\frac{c_{b2}}{\rho\sigma}\left[\left(\rho\frac{\partial\tilde{\nu}}{\partial x_3}\frac{\partial\tilde{\nu}}{\partial x_3}+\tilde{\nu}^2\frac{\partial\sqrt{\rho}}{\partial x_3}\frac{\partial\sqrt{\rho}}{\partial x_3}+2\sqrt{\rho}\tilde{\nu}\frac{\partial\sqrt{\rho}}{\partial x_3}\frac{\partial\tilde{\nu}}{\partial x_3}\right)\right.\\
&\qquad+\left(2\tilde{\nu}\frac{\partial\sqrt{\rho}}{\partial x_3}\frac{\partial\sqrt{\rho}}{\partial x_3}+2\sqrt{\rho}\frac{\partial\sqrt{\rho}}{\partial x_3}\frac{\partial\tilde{\nu}}{\partial x_3}\right)\delta\tilde{\nu}\\
&\qquad\left.+\left(2\rho\frac{\partial\tilde{\nu}}{\partial x_3}+2\sqrt{\rho}\tilde{\nu}\frac{\partial\sqrt{\rho}}{\partial x_3}\right)\frac{\partial\delta\tilde{\nu}}{\partial x_3}\right] \qquad \text{(A.28)}
\end{aligned}$$

Now each of the terms have been factored such that we can easily separate terms with $\delta\tilde{\nu}$ and terms with $\frac{\partial\delta\tilde{\nu}}{\partial x_3}$ from all other terms. Moving all terms containing $\delta\tilde{\nu}$ and its derivative to the left-hand side, and keeping all other terms on the right yields the following expression:

$$\mathcal{A}\delta\tilde{\nu}-\frac{c_{b2}}{\sigma\rho}\mathcal{B}\frac{\partial}{\partial x_3}\delta\tilde{\nu}-\frac{1}{\sigma\rho}\frac{\partial}{\partial x_3}(\mathcal{C}\delta\tilde{\nu})-\frac{1}{\sigma\rho}\frac{\partial}{\partial x_3}\left(\mathcal{D}\frac{\partial\delta\tilde{\nu}}{\partial x_3}\right)=\mathcal{E} \qquad \text{(A.29)}$$

where,

$$\mathcal{A}=\left[\frac{1}{\Delta t}-\left(c_{b1}\tilde{S}-\frac{c_{w1}f_w}{d^2}\tilde{\nu}\right)-\frac{2c_{b2}}{\sigma\rho}\left(\tilde{\nu}\frac{\partial\sqrt{\rho}}{\partial x_3}\frac{\partial\sqrt{\rho}}{\partial x_3}+\sqrt{\rho}\frac{\partial\sqrt{\rho}}{\partial x_3}\frac{\partial\tilde{\nu}}{\partial x_3}\right)\right] \qquad \text{(A.30)}$$

$$\mathcal{B}=2\left(\rho\frac{\partial\tilde{\nu}}{\partial x_3}+\sqrt{\rho}\tilde{\nu}\frac{\partial\sqrt{\rho}}{\partial x_3}\right) \qquad \text{(A.31)}$$

$$\mathcal{C}=\left(2\sqrt{\rho}\tilde{\nu}\frac{\partial\sqrt{\rho}}{\partial x_3}+\rho\frac{\partial\tilde{\nu}}{\partial x_3}\right) \qquad \text{(A.32)}$$

$$\mathcal{D}=(\mu+\rho\tilde{\nu}) \qquad \text{(A.33)}$$

$$\begin{aligned}
\mathcal{E}=\frac{1}{\rho}\left\{S_P-S_D+\frac{1}{\sigma}\left[\frac{\partial}{\partial x_3}\left(\mu\frac{\partial\tilde{\nu}}{\partial x_3}\right)+\frac{\partial}{\partial x_3}\left(\sqrt{\rho}\tilde{\nu}^2\frac{\partial\sqrt{\rho}}{\partial x_3}+\rho\tilde{\nu}\frac{\partial\tilde{\nu}}{\partial x_3}\right)\right.\right.\\
\left.\left.+c_{b2}\left(\sqrt{\rho}\frac{\partial\tilde{\nu}}{\partial x_3}+\tilde{\nu}\frac{\partial\sqrt{\rho}}{\partial x_3}\right)^2\right]\right\} \qquad \text{(A.34)}
\end{aligned}$$

and,

$$S_P = c_{b1}\tilde{S}\rho\tilde{\nu} \tag{A.35}$$

$$S_D = c_{w1}f_w\rho\left(\frac{\tilde{\nu}}{d}\right)^2 \tag{A.36}$$

The derivatives in Eq. A.29 are approximated using central differences. Using the same shorthand as defined in Eq. A.14, the implicit operator is formed as follows:

$$\begin{aligned}\mathcal{L} =&\mathcal{A}_i\delta\tilde{\nu}_i - \frac{c_{b2}}{\rho\sigma}\mathcal{B}_i\frac{1}{\Delta x^+ + \Delta x^-}(\delta\tilde{\nu}_{i+1} - \delta\tilde{\nu}_{i-1}) \\ &- \frac{1}{\rho\sigma}\frac{1}{\Delta x^+ + \Delta x^-}[\mathcal{C}_{i+1}\delta\tilde{\nu}_{i+1} - \mathcal{C}_{i-1}\delta\tilde{\nu}_{i-1}] \\ &- \frac{1}{\rho\sigma}\frac{1}{\Delta x_f}\left[\frac{\mathcal{D}_{i+1/2}}{\Delta x^+}(\delta\tilde{\nu}_{i+1} - \delta\tilde{\nu}_i) - \frac{\mathcal{D}_{i-1/2}}{\Delta x^-}(\delta\tilde{\nu}_i - \delta\tilde{\nu}_{i-1})\right]\end{aligned} \tag{A.37}$$

Combining terms, the implicit operator is finally expressed in tri-diagonal form:

$$\begin{aligned}\mathcal{L} =&\left(\mathcal{A}_i + \frac{\mathcal{D}_{i+1/2}}{\rho\sigma\Delta x_f\Delta x^+} + \frac{\mathcal{D}_{i-1/2}}{\rho\sigma\Delta x_f\Delta x^-}\right)\delta\tilde{\nu}_i \\ &- \left(\frac{c_{b2}}{\rho\sigma}\mathcal{B}_i\frac{1}{\Delta x^+ + \Delta x^-} + \frac{1}{\rho\sigma}\frac{1}{\Delta x^+ + \Delta x^-}\mathcal{C}_{i+1} + \frac{\mathcal{D}_{i+1/2}}{\rho\sigma\Delta x_f\Delta x^+}\right)\delta\tilde{\nu}_{i+1} \\ &+ \left(\frac{c_{b2}}{\rho\sigma}\mathcal{B}_i\frac{1}{\Delta x^+ + \Delta x^-} + \frac{1}{\rho\sigma}\frac{1}{\Delta x^+ + \Delta x^-}\mathcal{C}_{i-1} + \frac{\mathcal{D}_{i-1/2}}{\rho\sigma\Delta x_f\Delta x^-}\right)\delta\tilde{\nu}_{i-1}\end{aligned} \tag{A.38}$$

Appendix B

Code Description

This appendix provides a brief summary of the source code used in this research. My intention is that any researcher who receives the source code be able to use these descriptions to help them understand what the software is doing, and how to modify it for their purposes. The wall model uses an input deck to set many of the model a parameters. A description of the settings in the input deck is provided in Table B.1

B.1 us3d_user.f

This is the standard source file that US3D uses to implement user routines. This file contains `include()` statements for the other source files defined in this section (`testbl.f`,`wall_module.f`). These are the only routines that interface with or overwrite data in the parent finite-volume solver. The following routines are used in this file:

Item	Type	Description	Value used
`iwmodel`	int	Which wall model is used	2
`iwinit`	int	Wall model initialization method	3
`iwinv`	int	Wall model source term selection	0-2
`iwturb`	int	Wall model eddy viscosity formulation	2-3
`nyw`	int	Number of nodes in 1-D mesh	31
`iprobe`	int	Distance from wall in cells for probe location	4
`n_outer`	int	Number of outer loop iterations	10
`k_inner`	int	Number of inner loop iterations	1
`n_iup`	int	Number of timesteps before applying source term	4000
`wCFL`	double	CFL used within wall model	500-1000
`w_omega`	double	Relaxation factor for wall model update	0.2-0.3
`w_alpha`	double	Damping parameter for convective source term	10.0

Table B.1: Wall model input deck variables

Subroutine Name: `user_startup()`

Purpose: Creates wall model data structures

Description: This routine is executed on all processors in the calculation. Each processor loops over all zone types to detect wall zones. If wall zones are encountered, `itype` is checked to determine if it is wall modeled. If so, the following activities occur: 1) a MPI communicator is created of processors with wall model faces, 2) the wall model input deck section is read, 3) data structures are allocated, 4) face-basis is determined, 5) wall model grid is established.

Called by: `startup()`

Calls: `wall_model_input()`

Subroutine Name: `user_init()`

Purpose:	Initialize wall model data structures
Description:	This routine is executed on all processors in the calculation. If the processor contains wall-modeled faces, it initialized the solution in the wall model data structures per the setting in the input deck. The routine then initializes the 1-D solver. If the simulation is a restart, wall model restart files are checked for, and loaded if available.
Called by:	`init()`
Calls:	`wall_model_init(), wall_restart()`

Subroutine Name: `user_conv()`

Purpose:	Provide wall-model convergence information
Description:	Passes the L_2-norm of $\delta\tau_w$ and δq_w to US3D for inclusion in the convergence file.
Called by:	`null`
Calls:	`null`

Subroutine Name: `user_viswallbc()`

Purpose:	Invoke wall model to determine flux on modeled faces
Description:	This routine is executed on all processors with wall model faces. The routine updates the wall model boundary values with updated info from US3D. The routine then invokes the subroutine controlling the wall model
Called by:	`visflux()`
Calls:	`wallmodel_jrk()`

Element	Type	Dimension	Description
ns	int	scalar	number of species in wall model
iprobe	int	scalar	index of element where probe resides
jwall	int	scalar	index of face corresponding to wall model
iff	int	(4)	index of adjacent wall model structures
yn	double	(0:3,:)	location of model grid in global frame
rhos	double	(ns,:)	species density
u,v,w, t,tv,p, mut	double	(:)	primitives
sx	double	(3,3)	orthonormal face basis

Table B.2: Description of wall model data structure

Subroutine Name: `user_fix_tau()`

Purpose:	Correct the viscous flux for wall-modeled faces
Description:	This routine is executed on all processors with wall faces. If the face is a wall-modeled face, the viscous flux already determined by US3D is corrected with data from the wall model solution.
Called by:	`visflux()`
Calls:	`null`

B.2 wall_module.f

This source file includes most of the management routines for the wall model. Two modules are included, `wall_comm` which contains the variables needed by the wall model routines and `wall_module` which contains the subroutines. Of the variables included in `wall_comm`, the most important is the data structure `wms`, which is declared as an array of structures with one element corresponding to each wall modeled face on the processor. Table B.2 lists the information contained in each element of the data structure, `wms`. The subroutines contained in `wall_comm` are described below:

Subroutine Name: `wall_exch()`

Purpose:	Exchange wall model information between processors
Description:	This routine is executed on all processors with wall faces. MPI calls are executed to exchange `wms` structures amongst processors. **Note:** not used in the current implementation.
Called by:	`null`
Calls:	`null`

Subroutine Name: `wallmodel_jrk()`

Purpose:	Solve an arbitrarily complex wall model over a range of faces
Description:	The source term is zeroed, and then recomputed if required. Looping over faces, the wall model solution is packed into 1-D arrays and passed to the line solver. The new solution is then unpacked from the 1-D arrays and placed in `wms`. Once this has been completed, updated wall shear and heat flux is determined from the wall model solution.
Called by:	`user_viswallbc()`
Calls:	`wall_calc_duex(), outer_loop(), wall_solve()`

Subroutine Name: `wall_solve()`

Purpose:	Determine wall shear and heat flux over a range of faces
Description:	For each face, wall shear and heat flux are determined by an first-order finite difference of wall model data at the wall. The shear tensor is rotated from wall-frame to the solver-frame. L_2 residual of wall flux is determined and stored.
Called by:	`wallmodel_jrk()`
Calls:	`null`

Subroutine Name: `wall_calc_duex()`

Purpose:	Determine wall model source term from solver data
Description:	The source term used in the wall model line solve is determined in this routine.
Called by:	`wallmodel_jrk()`
Calls:	`null`

Subroutine Name: `wall_restart()`

Purpose:	Read and write wall model restart files
Description:	Each processor with wall model data either writes or reads restart info to/from `wall_data/` as directed by the invoking routine. **Note:** restarts do not support changing partitioning or number of points within the model. In such cases the default initialization is used.
Called by:	`user_init()`, `user_dataio()`
Calls:	`write_wallfile()`, `read_wallfile()`, `check_wallfile()`

Subroutine Name: `wall_model_input()`

Purpose:	Read the wall model section of the input deck
Description:	This subroutine is called by all processes with wall faces. Process `0` reads the input deck and broadcasts setting to all other processes.
Called by:	`user_startup()`
Calls:	`null`

B.3 testbl.f

This source file contains all of the routines that actually populate and solve the 1-D system of equations. It contains four modules, `wall_constants`, `wall_data`, `wturb_module`, and `wall_subs`. Module `wall_constants` defines a number of parameters used in the line solve. Module `wall_data` stores all of the common switches and solution variables for the line solve. Module `wturb_module` holds the S-A model constants and routines

needed to accomplish a line solve of the S-A equation. Module `wall_subs` contains all routines that accomplish the line solve.

Subroutine Name: `wall_turb_guess()`

Purpose: Determine S-A variable from eddy viscosity

Description: If needed, this routine solves for S-A variable on the boundary by Newton iteration given a value for eddy viscosity

Called by: `outer_loop()`

Calls: `null`

Subroutine Name: `wall_turb_duex()`

Purpose: Calculate the explicit update to the S-A equation

Description: Given the current line solution from the outer loop, determine explicit update to S-A equation

Called by: `calc_duex()`

Calls: `null`

Subroutine Name: `wall_turb_operator()`

Purpose: Form implicit operator for S-A equation

Description: Inside the inner loop, calculate the terms of the S-A implicit operator

Called by: `solve_line()`

Calls: `null`

Subroutine Name: `wall_model_init()`

Purpose: Initialize 1-D line solver

Description: Sets solver switches

Called by: `user_init()`

Calls: `null`

Subroutine Name: `solve_line()`

Purpose: Solve 1-D tri-diagonal system

Description: Solves the selected equation using a Thomas algorithm

Called by: `solve_bl()`

Calls: `null`

Subroutine Name: `calc_duex()`

Purpose: Determine explicit update to 1-D equation

Description: Evaluates the explicit updated associated with the viscous terms of the 1-D equation

Called by: `solve_bl()`

Calls: `wall_turb_duex()`

Subroutine Name: `calc_gradients()`

Purpose: Determines gradients at the faces between the 1-D nodes

Description: Calculates all necessary gradients evaluated at face locations between the nodes in the 1-D finite-difference mesh

Called by: `solve_bl()`

Calls: `null`

Subroutine Name: `calc_thermo()`

Purpose: Determine viscosity and thermal conductivity (molecular and turbulent)

Description: Viscosity is determined by Sutherland's formula, and thermal conductivity from constant Prandtl number. Turbulent eddy viscosity is prescribed either from a mixing length model or from the S-A equation.

Called by: `solve_bl()`

Calls: `null`

Subroutine Name: `update()`

Purpose: Update the solution on the inner loop

Description:

Called by: `solve_bl()`

Calls: `null`

Subroutine Name: `update_rho()`

Purpose: Update density in the outer loop

Description: Based on the updated temperature field, determine density field from the equation of state

Called by: `outer_loop()`

Calls: `null`

Subroutine Name: `solve_bl()`

Purpose: Execute inner loop iterations for 1-D solve

Description: Solves 1-D system of equations in an inner loop

Called by: `outer_loop()`

Calls: `calc_thermo()`, `calc_gradients()`, `calc_duex()`, `solve_line()`

Subroutine Name: `outer_loop()`

Purpose: Drives solution of 1-D system

Description: Receives 1-D arrays to use in solving the wall model on one face. Passes information to and from the invoking routine

Called by: `wallmodel_jrk()`

Calls: `solve_bl()`, `update_rho()`

Appendix C

Acronyms

Table C.1: Acronyms and Nomenclature

Acronym	Meaning
AIAA	American Institute of Aeronautics and Astronautics
CFL	Courant-Friedrichs-Lewy Condition
CUBRC	Calspan-University of Buffalo Research Center
DPLR	Data Parallel Line Relaxation
CFD	Computational Fluid Dynamics
DNS	Direct Numerical Simulation
HCF	Hollow Cylinder Flare
LCF	Large Cone Flare
LES	Large Eddy Simulation
NASA	National Aeronautics and Space Administration
ODE	Ordinary Differential Equation
RANS	Reynolds-Averaged Navier-Stokes
RK3	Third-Order Runge-Kutta
TLM	Two-Layer Model
SA, S-A	Spalart-Allmaras turbulence model
STBLI	Shock Turbulent Boundary Layer Interaction

Continued on next page

Table C.1 – continued from previous page

Acronym	Meaning
WM-LES	Wall-Modeled Large Eddy Simulation
WR-LES	Wall-Resolved Large Eddy Simulation